DESIGN, DEVELOPMENT, AND MODELING OF PERFUSABLE HYDROGELS TO REGULATE CELL FATE AND BEHAVIOR IN 3D CONSTRUCTS

By

Brian O'Grady

Vanderbilt University

Dissertation

Submitted to the Faculty of the

Graduate School of Vanderbilt University

in partial fulfillment of the requirements

for the degree of

DOCTOR OF PHILOSOPHY

in

Interdisciplinary Materials Science

May 10, 2019

Nashville, Tennessee

Approved:
Leon M. Bellan, Ph.D.
Ethan S. Lippmann, Ph.D.
Craig L. Duvall, Ph.D.
Elaine L. Shelton, Ph.D.
Vivian Gama, Ph.D.

To my wife, Kristin O'Grady, I am the best I can be because of you
To Lilly, I love you very much and you're lucky you're so damn cute
and
To my family and friends for their infinite support and encouragement

ACKNOWLEDGMENTS

I would like to thank my Ph.D. advisors, Professors Leon Bellan and Ethan Lippmann, for their guidance and expertise throughout my dissertation project and my development as a scientist. I would also like to thank my committee members, Professors Craig Duvall, Elaine Shelton and Vivian Gama for providing valuable insight and dedicating time to advising me on this work.

Next, I would like to thank my collaborators and peers for their support and contributions to this work. Many thanks go to Dr. Mason McClatchey for his help with developing image processing code. Dr. Jeff Reese guidance and tutelage with understanding the physiology of the human ductus arteriosus. Dr. Mukesh Gupta for his expertise in NMR is greatly appreciated. Several graduate students assisted with the data experiments and processing, including Kylie Balotin, Emma Neal, Allison Bosworth, John Rector. I would like to thank my collaborators and peers in SyBBURE, Dr. Rizia Bardhan and May Ou for their guidance in computational modeling and invaluable insight into my experimental design and data acquisition.

This work would not have been possible without the financial support provided by Vanderbilt University Start-Up funding for Professors Leon Bellan and Ethan Lippman, NSF BMAT 1506717, NIH R00EB013630, NARSAD Young Investigator Award from the Brain and Behavior Research Foundation, NSF Graduate Research Fellowship DGE-1445197, CMMI-1634856, by NIH T32GM007347, and Dr. Anita Mahadevan-Jansen and Jennifer Bateman. I would like to also acknowledge the laboratories and core facilities in which portions of this work were performed, including Vanderbilt Institute for Nanoscale Science and Engineering.

TABLE OF CONTENTS

LIST OF TABLES

Table

LIST OF FIGURES

Figure Page

CHAPTER 1

INTRODUCTION

1.1 Motivation

Over the past several decades, animal models have been used to demonstrate efficacy and safety of promising therapeutics for a wide spectrum of diseases and disorders. During that time, 85% of early clinical trials for novel drugs failed despite promising results from preclinical animal studies[1–3]. Of those 15% that were deemed effective in phase III trials, only half became approved for larger population studies. In general, it can take more than 10 years to get a new drug from the laboratory to earning FDA approval for clinical use. There are many reasons why promising drugs fail phase III trials. One of the main reasons is the inability to demonstrate efficacy when translated from animal models to human trials. In one particular finding, 54% of 640 phase III trials with novel therapeutics failed in clinical development, with more than half of those failing to demonstrate efficacy despite *in vivo* success in preclinical studies[4]. Because of these failures, the FDA and European Medicines Agency introduced guidelines for testing very small doses of novel drug candidates in humans[4,5]. This method was approved as a way to bypass animal models to evaluate therapies in humans without the concern of toxicity caused by normal drug doses. These early trials, called “phase 0”, gave insight into how drugs were absorbed and distributed in the body. However, roughly one fourth of the new drugs failed to meet the criteria for advancing into the next phase. The high failure rates of clinical trials and phase 0 trials reveal an urgent need for new *in vitro* technologies that will better represent the three-dimensional (3D) *in vivo* physiology and microenvironment of human cells and tissues; such platforms hold great

promise for high throughput screening, drug discovery, and a better understanding of the pathophysiology associated with human diseases.

An ideal 3D *in vitro* model of a human tissue or organ would be able to incorporate multiple cell types, large enough to accommodate cell growth, scalable, and would provide a means for spatiotemporal control over the delivery and removal of compounds during long term culture. Additionally, the 3D nature of the platform would better simulate the target physiological microenvironment where cells can attach, metabolize, proliferate and, if necessary, differentiate. Currently available models may meet some of these needs, but each have their respective strengths and limitations, and none meet all of the above criteria. One of the biggest challenges in developing 3D cultures for extended studies or high throughput screening is the ability to properly support tissue-specific cell-to-cell interactions and cell-to-extracellular matrix (ECM) interactions. One common system for high throughput screening uses a hanging drop culture approach[6,7]. Such experiments are often performed in 96- or 384-well plates and can provide a robust attrition of novel therapeutics and dosing. However, due to the complex protocols involved with such approaches, they often require significant expertise and are still susceptible to user-induced variations in ECM composition. Another common issue is the biomaterial used to embed cells in 3D culture. Common hydrogels used for *in vitro* modeling are Matrigel[8], hyaluronic acid[9], silk[10], polyethylene glycol (PEG)[11], alginate[12] and collagen[13,14]. These hydrogels have provided previously unobtainable advancements in 3D culture and have deepened the understanding of the microenvironment that presents key regulatory signals to support proliferation, migration and fate decision[8]. However, they can be expensive (Matrigel, hyaluronic acid, collagen), can lack tissue-specific presentation of ECM cues for cell survival/proliferation (PEG, alginate, silk), may be difficult or impossible to pattern (Matrigel,

hyaluronic acid), and can exhibit variation in composition due to batch-to-batch manufacturing (Matrigel)[15]. Providing the research community with enabling technologies for large, scalable, perfusable cell and tissue culture scaffolds would catalyze new discoveries through improved understanding of disease biology and serve as platforms for rapid screening of potential novel therapeutics.

1.2 A Custom, DIY Peristaltic Pump to Facilitate Hydrogel Construct Perfusion

To enable long-term 3D cell culture (on order of months), thick cell-laden hydrogels must be perfused with fresh culture media. Thus, in Chapter 3, I will discuss the development of a novel pumping system and demonstrate its use in conjunction with a perfusable hydrogel construct to enable *in vitro* models of human tissues. This platform consists of a compact, 3D-printed housing unit, stepper motors, EasyDriver chips, a power supply, and an Arduino board. Each Arduino board enables control over up to six motors. While the Arduino and motor driver electronics are located outside of the incubator, the motors and associated pump hardware are placed in the incubator, resulting in a smaller footprint within the controlled incubator environment as compared to placing a commercially available perfusion systems in the incubator. Furthermore, this unique system allows for complete control over motor scheduling and pump rates.

Commercially available perfusion systems typically consist of a single motor and thus lack the flexibility to pump multiple independent fluid conduits at different speeds and time intervals simultaneously in an automated, programmable manner[16–18]. Additionally, these systems are large, expensive and lack critical features, such as multiple motors for various fluid flow rates and scheduling. These limitations make it difficult to develop more complex experiments involving

engineered tissues, as such systems fail to meet the unique demands of tissue construct perfusion experiments.

The perfusion system described in Chapter 3 provides an inexpensive pumping platform that can be programmed to schedule and run multiple motors at various speeds. This control facilitates the ability to increase the complexity of perfusion experiments and enables reliable, long term (months) culture experiments.

1.3 Perfusable Hydrogels Enable Spatiotemporal Control of Morphogen Gradients

Morphogen presentation plays a critical role in biological development[19–21]. These cues can be spatially and temporally interpreted to determine cell fate and direct the eventual formation of large, complex tissues and organs. Few platforms have been able to produce morphogen gradients over extended periods of time and across a large scale (on the order of centimeters) to guide differentiation and eventual proliferation and self-organization. The current techniques to recapitulate these cues have shown limited efficacy in developing sustained gradients to induce a spectrum of differentiation in a large tissue construct.

In the context of mesenchymal stem cells, one approach to producing spatially-varying differentiation employed microspheres loaded with various concentrations of bone morphogen protein 2 (BMP2) and insulin-like growth factor 1 (IGF-1)[22]. The researchers were able to create gradients of multiple species within a single scaffold. However, because the microparticles were crosslinked into the hydrogel and not perfused, the system could not sustain a uniform morphogen gradient for extended studies without compromising the integrity of the hydrogel.

In Chapter 4, I describe a platform employing embedded perfusion channels that provides spatial and long-term (months) temporal control of morphogen delivery in a hydrogel that is large

enough to accommodate stem cell growth into larger tissue structures. The ability to predict and spatiotemporally modulate the presentation of morphogens in a large tissue construct will lay the groundwork for more complex patterning of stem cell fate.

1.4 A Novel Biomaterial that Facilitates Neuronal Network Development in 3D

The lack of efficacy of many therapies tested in clinical trials, to a great extent, is due to a lack of accurate *in vitro* models. Currently, there are several examples of 3D human neural tissue models in the literature, each of which aim to create interconnected neural circuits[23–28]. However, these culture platforms are generally unable to recapitulate appropriate cell morphology, electrophysiological activity, and robust neuronal communication over extended timeframes. Additionally, the typical materials used for the ECM are either too compliant (Matrigel, hyaluronic acid), lack physical cues that promote neuronal maturation (PEG, silk), or collapse under their own weight (Matrigel and hyaluronic acid)[25,29,30]. These scaffolds are generally too soft for molding, making them incompatible for incorporating vasculature using top-down fabrication approaches and thereby cannot overcome mass transfer limitations that result in hypoxia-mediated apoptotic regions in larger structures.

Therefore, to overcome some of these issues, in Chapter 5 I will discuss a ECM biomaterial which consisted of gelatin methacrylate (GelMA) conjugated with a peptide from an extracellular epitope of N-cadherin. This material provides physiological stiffness, supports neuron survival through the presentation of the peptide and RGD motif, and may be patterned with perfusable channels to enable long term cell culture. The ability to sustain neurons in a perfusable hydrogel will yield a more physiologically accurate representation of neuronal network formation and serve as a platform for screening potential therapeutics.

1.5 An Engineered Perfusable Ductus Arteriosus Construct

In the last several decades, there has been a significant lack of successful clinical trials for novel therapeutics for patent ductus arteriosus (PDA) [31,32]. Though animal models have been used to screen potential therapies for closing a PDA[33,34], this has led to few pharmacological therapies that are effective in closing of PDA in pre-term human infants. Some of the most effective current therapies for closing PDA consist of inhibiting cyclooxygenase (COX) enzymes[35]. Ibuprofen is a common COX inhibitor used to induce vasoconstriction of the PDA. However, COX enzymes are present in organs throughout the body, so off-target effects are a significant concern. For example, due to the presence of COX enzymes in the renal system, systemic use of ibuprofen can result in a reduction of renal prostaglandins, which disrupts vasodilation, reduces renal plasma flow and leads to acute deterioration of renal function. Although such treatments have become rather common, they are not ideal given the increased risk of pulmonary hypertension, systemic vasoconstriction, and long-term adverse side-effects. There is thus a critical need to develop new, more specific therapeutics that can treat a PDA without negatively affecting other tissues.

To address this issue, in Chapter 6 I will discuss the development of a perfusable artificial artery containing human ductus arteriosus smooth muscle cells (SMC) to enable rapid screening of potential therapeutics.

1.6 Innovation

Biomedical research using 3D tissue culture to model human tissues currently lacks a solution for perfusable, large-scale constructs (cm) that support growth and/or differentiation of

human cells for time scales on the order of weeks to months. This work described herein is based upon newly-developed methods to create perfused, customizable hydrogel scaffolds designed for stem cell biology, neurobiology, and vascular biology applications. A low-cost pump perfusion system was designed to provide dynamic control over the flow rate and composition of media delivered to embedded cells. This system was used to control the spatially and temporally varying presentation of morphogens in a 3D scaffold for human stem cell differentiation into a spectrum of cell fates, and a computational model was developed to provide a new tool for predicting spatial and temporal morphogen gradients. Furthermore, a perfused 3D scaffold modeling the human ductus arteriosus was developed and resulted in cell behavior that mimics the native vessel. This novel construct may be useful for screening potential therapeutics for patent ductus arteriosus. Finally, a bioinstructive material was developed to enable *in vitro* formation of neuronal networks from a suspension of human iPSC-derived neural cells. This biomaterial is the first to support the survival of *single* neural cells in a 3D matrix and the formation of individually distinguishable axon projections and synaptic connectivity. This platform provides a new research tool for studying cell-to-cell disease propagation for neurological diseases such as Alzheimer's Disease. Overall, these new technologies, materials and techniques may provide more robust studies of stem cell differentiation and more effective, long-term 3D cell culture platforms for screening therapies and gaining new insights into disease pathophysiology.

1.7 Specific Aims

The first objective of this dissertation is to develop a customizable pump perfusion system to provide sustained spatial and long-term (months) temporal control of morphogen delivery in a hydrogel to induce gradients of stem cell differentiation. Using this system, we will develop and

validate a computational model of the spatiotemporally varying presentation of morphogens in a 3D hydrogel. The second objective is to demonstrate the broader utility of the perfused hydrogel system by developing *in vitro* models for 1) a neuronal network using induced pluripotent stem cell (iPSC)-derived neuronal cells and 2) the ductus arteriosus, a fetal blood vessel that must close after birth for proper blood circulation to occur.

Aim 1: Design, fabricate, and model a platform enabling spatiotemporal control of soluble factor delivery to cells in a large hydrogel scaffold.

Aim 1.A. Develop and characterize a customizable pump perfusion system and bioreactor to support controlled morphogen delivery to stem cells in a 3D hydrogel scaffold. An Arduino and stepper motor-based pump system was designed, fabricated and calibrated for precisely controlled delivery of soluble factors.

Aim 1.B. Create and validate a computational model for temporally varying delivery of soluble factors to cells in a 3D hydrogel scaffold via embedded perfusion channels. The diffusion coefficient of a small and large molecule, retinoic acid and dextran, will be measured in a hydrogel using Raman spectroscopy and FRAP, respectively. The resulting data will be used to inform and validate a model created in COMSOL.

Aim 2: Differentiate mesenchymal stem cells into various lineages using opposing gradients of signaling factors

Aim 2.A. Create opposing gradients of morphogens to induce a spectrum of differentiation in a 3D hydrogel scaffold. The pump perfusion system developed in Aim 1 was used to deliver

two different morphogens from two isolated parallel channels to demonstrate the ability to create two opposing gradients of mesenchymal stem cell (MSC) differentiation in the hydrogel.

Aim 2.B. Demonstrate spatial control of differentiation by varying the morphogen concentration. To demonstrate spatial control over the differentiation gradient, the concentration of TGFβ1 (the primary morphogen driving chondrogenic differentiation) delivered to a hydrogel was modulated. This showed that modulating morphogen concentration presented to the cells through diffusion altered the differentiation spectrum in the hydrogel.

Aim 3: Apply the pump and perfused hydrogel platform to develop new *in vitro* models for the study of disease and potential therapies.

Aim 3.A. Develop a biomaterial hydrogel that supports the formation of a 3D neuronal network and can serve as a platform for studying neurological diseases. The pump perfusion system was used to supply media to iPSCs-derived neurons embedded in a hydrogel modified with N-cadherin, a short peptide that promotes synaptic formation and plasticity. The N-cadherin was conjugated to gelatin-methacrylate (GelMA) to enhance neuron cell viability and enable the formation of an interconnected neuronal network. The creation of a neuronal network out of single cell suspension will provide previously unattainable information regarding how neuronal pathophysiology propagates between individual cells and enable future drug discovery efforts for a wide range of neurological diseases.

Aim 3.B. Develop a perfused tissue construct to model the human ductus arteriosus. An engineered artery was developed using human ductus arteriosus (hDA) SMCs embedded in a perfused, cylindrical hydrogel. Functionality that mimics the native vessel was characterized (perpendicular cellular alignment, matrix remodeling, and inducible vessel constriction). This new

technique will enable rapid screening of potential therapeutics for treating PDA (failure to close vessel upon birth) in a human model.

1.8 Outline

In this dissertation, a new platform for supporting cell survival and directing cell fate/phenotype in *in vitro* models of stem cell differentiation, neuronal network, neurological disease, and patent ductus arteriosus are given. Chapter 1 provides the motivation and introductory information for this research and outlines the specific aims that are addressed. Chapter 2 provides an overview of relevant background information, and describes the biology of organ development, current approaches for spatiotemporal control of soluble factors in tissue constructs, current methods for forming neuronal networks, and current methods for fabricating perfusable tissue constructs. Chapter 3 describes the development of a reliable and flexible pump perfusion system for long term cell culture. In Chapter 4, I discuss how opposing gradients of morphogens can facilitate the patterning of stem cell fate in a large 3D hydrogel. Chapter 5 describes a new biomaterial for sustained 3D neural cell culture for the study of neurological disease pathology. In Chapter 6, a novel 3D hDA-laden, perfusable construct is established for the screening of novel therapeutics. Finally, a summary of the major results and a discussion of the broader impacts, challenges and future directions for this work will conclude this dissertation.

CHAPTER 2

BACKGROUND

2.1 Organ Development through Spatiotemporal Control

The development of complex multicellular organs is regulated through gradients of morphogens. This presentation of proteins or small molecules is tightly controlled to enable coordination of cellular growth, differentiation, and patterning. One example of the complexity of morphogen-guided differentiation is the development of the neural tube[36]. Neural tube development begins with the formation of the neural plate. This plate begins to fold to make neural grooves. When the grooves come in contact with each other due to folding, they begin to fuse. After fusing is complete, the neural tube begins developing into a more complex structure. There are four primary signals that are responsible for patterning the neural tube: Sonic hedgehog (SHH), bone morphogen protein (BMP), retinoic acid (RA) and fibroblast growth factor (FGF) (Fig. 2.1).

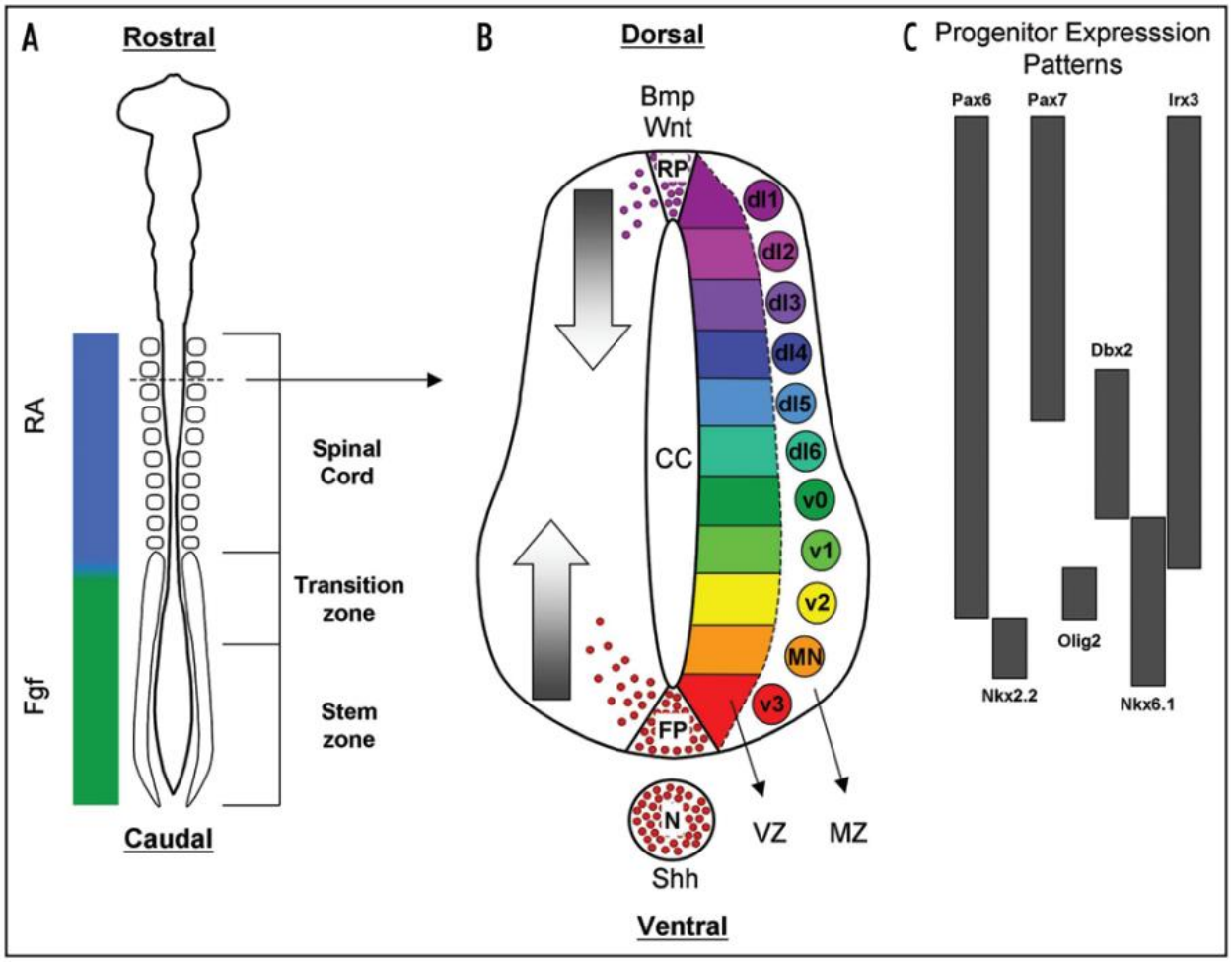

Figure 2.1: Illustration of BMP/Wnt and SHH opposing gradients in neural tube development[37].

During neural tube development, the anteroposterior axis (AP) is formed by opposing gradients of RA and FGF. RA is produced by the paraxial mesoderm and is responsible for down-regulating the FGF signals that are generated by the caudal mesoderm[38–42]. In general, RA and FGF act antagonistically in the developing neural tube. In the furthest posterior position, FGF signaling is at its highest concentration, maintaining a zone of undifferentiated stem cells at the posterior end of the axis. RA is at its highest concentration at the most extreme anterior position and promotes differentiation of neural ectoderm and mesoderm. A gradient of FGF signaling is established, which is antagonized by an opposing gradient of RA signaling. The dorsoventral axis

(DV) is formed by opposing gradients of SHH and BMP. The SHH gradient is produced by the notochord and floor plate. It is responsible for differentiating ventrally located neural cells in a concentration dependent manner. BMP is produced by the roof plate on the dorsal side. This protein is responsible for differentiating dorsally located neural cells into a spectrum of differentiation states[43].

At this point the neural tube has spatially organized domains due to the highly coordinated morphogen gradients. These domains can be defined into three separate regions and the spinal cord. The first is the prosencephalon region; this is the most anterior aspect of the neural tube and is ultimately responsible for the basal ganglia, limbic forebrain, olfactory system, and cerebral cortex. The next region is the mesencephalon, which is ultimately responsible for the visual and auditory reflex pathways. The most posterior region is the rhombencephalon. This section contains the rest of the brain and eventually develops into the pons, trapezoid body and the cerebellum[44].

All of these structures are developed through highly coordinated spatially and temporally varying presentation of specific growth factors and molecules. This controlled presentation can be seen in nearly every organ system in the body such as the central nervous system (described here to demonstrate the intricate and complex signaling processes), the heart[45], and the lining of the gut[46]. It would be quite useful to mimic the spatial and temporal coordination of morphogen gradients that is prevalent *in vivo* with an engineered platform for *in vitro* tissue culture. Such a platform would not only benefit studies in organ development, but could be of use in applications related to human disease modelling and regenerative medicine.

2.2 Current Methods for Spatiotemporally Controlled Delivery of Soluble Factors

Advances in tissue engineering and drug discovery research are rapidly advancing our understanding of the biological world. Over the past decade, these disciplines have enabled new tools that overcome the limitations of current animal models of disease. Traditionally, 2D *in vitro* culture models have been used as platforms for drug screening, toxicity and pathophysiology to diseases[47]. This approach, while it has served the research community for generations, is limited in its ability to support truly biomimetic behavior due to the lack of a 3D environment. Often, animal models are used to address some of these issues[48–50], as they exhibit increased complexity and provide a physiological, 3D environment in which to perform studies. Technological advances have recently enabled the alteration of the molecular genome of mouse germ lines to create humanized animal models for drug screening and efficacy of new therapeutics. However, due to remaining differences in physiology, limited utility in high-throughput screening efforts, and high cost, the overall rate of successful translation of animal models to clinical trials is a staggeringly low 8%[3]. Therefore, new tools are necessary to further advance regenerative medicine and facilitate translation from the lab bench to human trials.

One technology developed to address this problem is the 3D cell culture system, which is often based on hydrogel constructs containing organoids (3D multicellular mass) or individually suspended cells (single cell type or co-culture) [25,27,51]. 3D cell culture tools have been developed to control three key elements: the cells, the ECM (e.g. stiffness, adhesion motifs) and the signals provided to the cells in the ECM (e.g. morphogens, growth factors).

One approach to control many of these factors is the organ-on-a-chip platform[52–55] (Fig. 2.2). These are microfluidic devices that are developed to recapitulate the 3D microenvironment, while enabling control over the presentation of soluble factors such as morphogens. This

technology has been able to mimic the *in vivo* environment and facilitate desired cell function for prolonged experiments and has served as a useful platform for tissue and disease modeling for drug discovery[56–59]. For example, Jang et al. developed a model system for predicating drug efficacy, interactions and drug induced injury. This was achieved by seeding human renal cells in a perfusable micropatterned device and was used to drug screen known compounds and to study novel compounds to test drug toxicity[60]. Another system used multimaterial 3D printing to integrate cardiac cells on soft strain gauges to monitor contractile responses to various microenvironments and topographies[61]. These and other versatile platforms have made significant contributions to our understanding of cell behavior. However, these systems are designed on the sub-millimeter scale and cannot be scaled up in size without the addition of perfusion channels to address the limits of diffusion. In many cases, larger models are needed for more accurate modeling of the complex, heterogeneous organization of natural tissues.

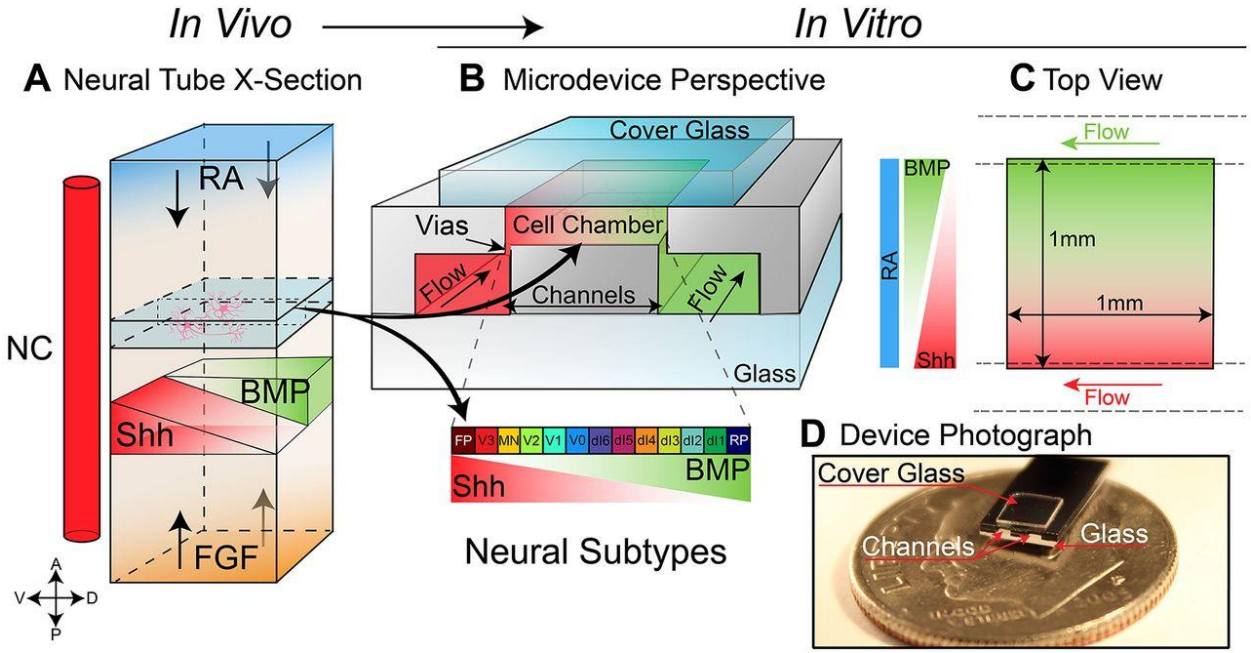

Figure 2.2: Schematic of microfluidic device intended to recapitulate the *in vivo* neural tube developmental patterning.

Another approach to enable delivery of soluble biochemicals is through the use of microparticle-based controlled release formulations. Microparticles have been long used in research and clinical applications to improve the performance of drug delivery [22,62,63]. Typically, these microparticles are made of a biocompatible polymer (e.g. PLGA, Chitosan) that are able to carry various concentrations of chemical compounds. Under various conditions (e.g. hypoxia, change in pH, ROS, hydrolytic degradation) these carriers release the loaded compounds into the microenvironment to induce cellular responses such as multicellular differentiation, gene/protein expression and ECM remodeling. One example of these microparticle platforms, developed by Poole et al., employed polypropylene sulfide loaded with curcumin that is released in the presence of reactive oxygen species (ROS)[64]. Curcumin is a natural molecule that acts to inhibit intracellular pro-inflammatory pathways by scavenging ROS. These microparticles have hydrophobic and hydrophilic regions that can change morphology in the presence of ROS and release curcumin in the local extracellular matrix. This platform was successfully used both *in vitro* and *in vivo* and has promising therapeutic potential for diabetes-induced ROS production. However, while these particles are promising for this application, the release rate of curcumin from the microparticles is governed by the ROS production of the local environment and cannot be modulated once injected into the tissue. Thus, this approach does not allow for dynamic user control over the presentation of therapeutics. A perfusable 3D culture system that can both sustain cells and allow for the dynamic delivery and removal of factors in a spatially controlled fashion would be beneficial to drug screening or stem cell differentiation research efforts.

2.3 Current Methods for Visualizing and Creating Hydrogel Neuronal Networks

Recent progress in 3D neural models and visualization of neuronal networks has provided new insight into understanding 3D network formation and function[30,65–67]. For example, Green et al. embedded Schwann cells and neural-like PC12 cells in a polyvinyl alcohol hydrogel with various mechanical properties to test which modulus enhanced the development of neuronal network[68]. However, this method used neuronal-like cells and not iPSC-derived neurons. Additionally, the human brain has billions of neurons interconnected to trillions of synapses. This makes it difficult to recapitulate this complex 3D neural cell connectivity in a construct that permits visualization of cell growth and disease pathology at the single cell level.

One attempt to create a platform for neurological studies is to culture cells on or in soft hydrogels. In previous work, Kaplan and colleagues were able to utilize a porous silk scaffold that has elastic properties similar to that found in brain tissue[29]. iPSCs and Alzheimer's-presenting primary neurons were embedded in the small scale (2mm thick) 3D silk scaffolds and cultured for long periods of time (months) (Fig. 2.3). The researchers were able to measure local electric field potentials in the scaffold indicating the presence of healthy, functioning neurons. Additionally, they visualized real-time growth and organization of the cells, including the formation of thick axonal processes. The ability to visualize individual axons is a distinct advantage of this approach as compared to experiments employing rat/mouse cortical neurons and 3D neural organoids. However, while this platform has its benefits, there are several disadvantages. One disadvantage was their inability to pattern channels for perfusion in the silk hydrogel. Thus, it was not possible to create larger 3D constructs with these materials, and thus these platforms were limited in their potential to mimic the complexity of organization found in the human brain. Additionally, the scaffolds must be seeded at a high initial cell density (each cluster had a minimum of $5x10^6$

cells/mL) to ensure survival and proliferation. However, peripheral cells obstruct visualization of cells embedded deep within the scaffold and grow thick axons that prevent researchers from visualizing axon formation and pruning at the single cell level. To overcome these limitations, there is a need for a biomimetic material that can present appropriate physical cues (N-cadherin, RGD motif) to promote cell integration and survival in single cell neuron suspension, while remaining rigid enough to support perfusable channels.

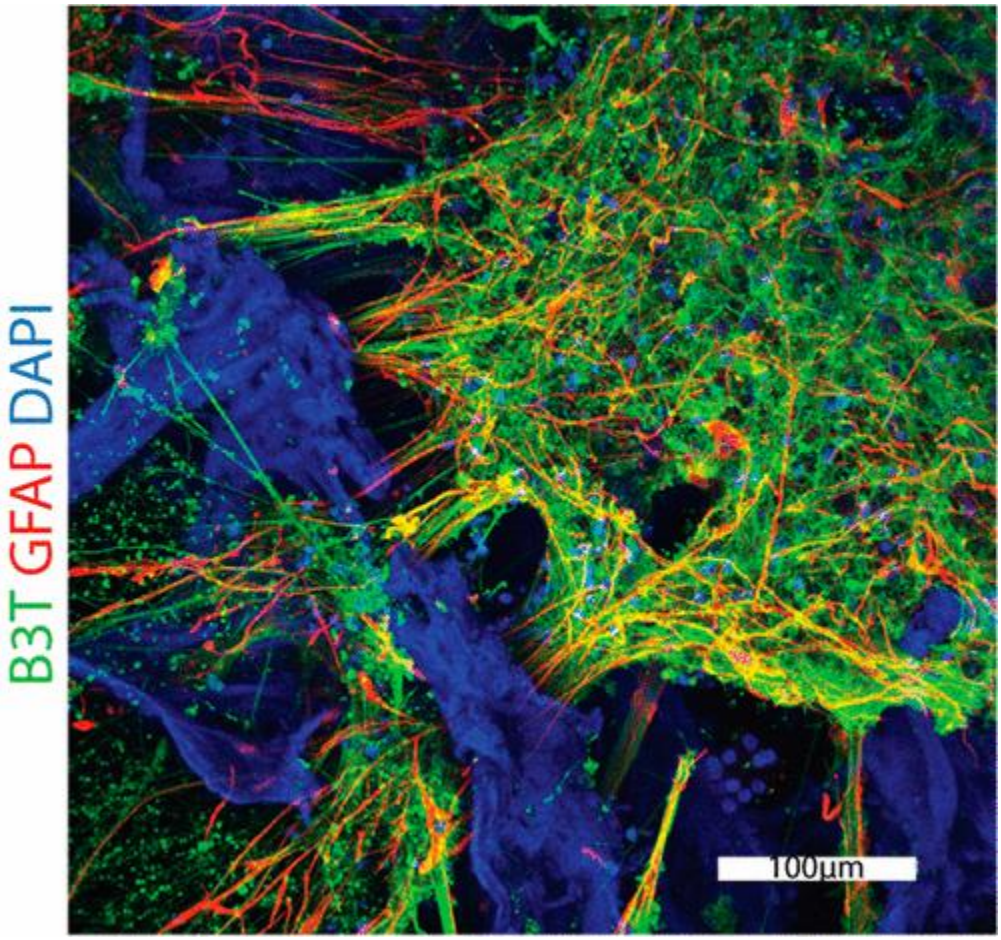

Figure 2.3: iPSCs derived neurons embedded in a silk scaffold for 10 months[29].

Another attempt to visualize and gain insight into the complex neuronal networks is through the use of mouse models[69,70]. Until recently, researchers had to harvest fresh mouse

brain tissue, slice it, and then employ patch clamping to study the electrophysiological responses to stimuli in various parts of the brain. The fresh brain slice approach allowed researchers to patch on to and stimulate a desired brain region and then place a second patch clamp at a location that is believed to be connected to the cells that were first patched. The response at the second location can be recorded to study neural communication. This method, however, is quite inefficient, leaving researchers to guess whether their patches are actually synaptically connected. To overcome this issue, adeno-associated viral (AAV) vectors have been developed to stereotactically deliver small depots of virus that can infect a local region of the brain[71]. The virus then intracellularly incorporates into the genome of the cell and begins to express a fluorescent protein attached to a targeted protein. Once the virus is incorporated into the neuron and expresses the target protein, the virus then spreads to dendritically or synaptically connected neurons (anterograde or retrograde). This viral propagation continues to label the cells with a fluorescent protein and can travel through long distant circuits in the brain (Fig. 2.4). This technology is currently one of the most commonly used systems for mapping neuronal networks in mice. This is a significant advance in the ability to map synaptically-connected cells on a large scale and monitor the response to external stimuli (e.g. electrophysiological, drugs compounds). While this groundbreaking technique has the potential to lead to new neural discoveries, it still has some limitations. One problem with the AAV neuronal tracing technique is the amount of time required for the virus to spread. Many researchers target regions of the brain that are physically distant from each other, and it can take several weeks for the AAV to fully spread from one region to another. Moreover, the AAV has been known to spread to off-target regions of the brain. Another significant issue with this approach is that brain slices are required, so that only harvested and sliced brain tissue may be used. Thus, while this approach can be useful for large scale neuronal tracing in harvested

tissue, long term, non-destructive monitoring of neuron growth, synapse pruning, plasticity and disease progression in living tissue is still impossible.

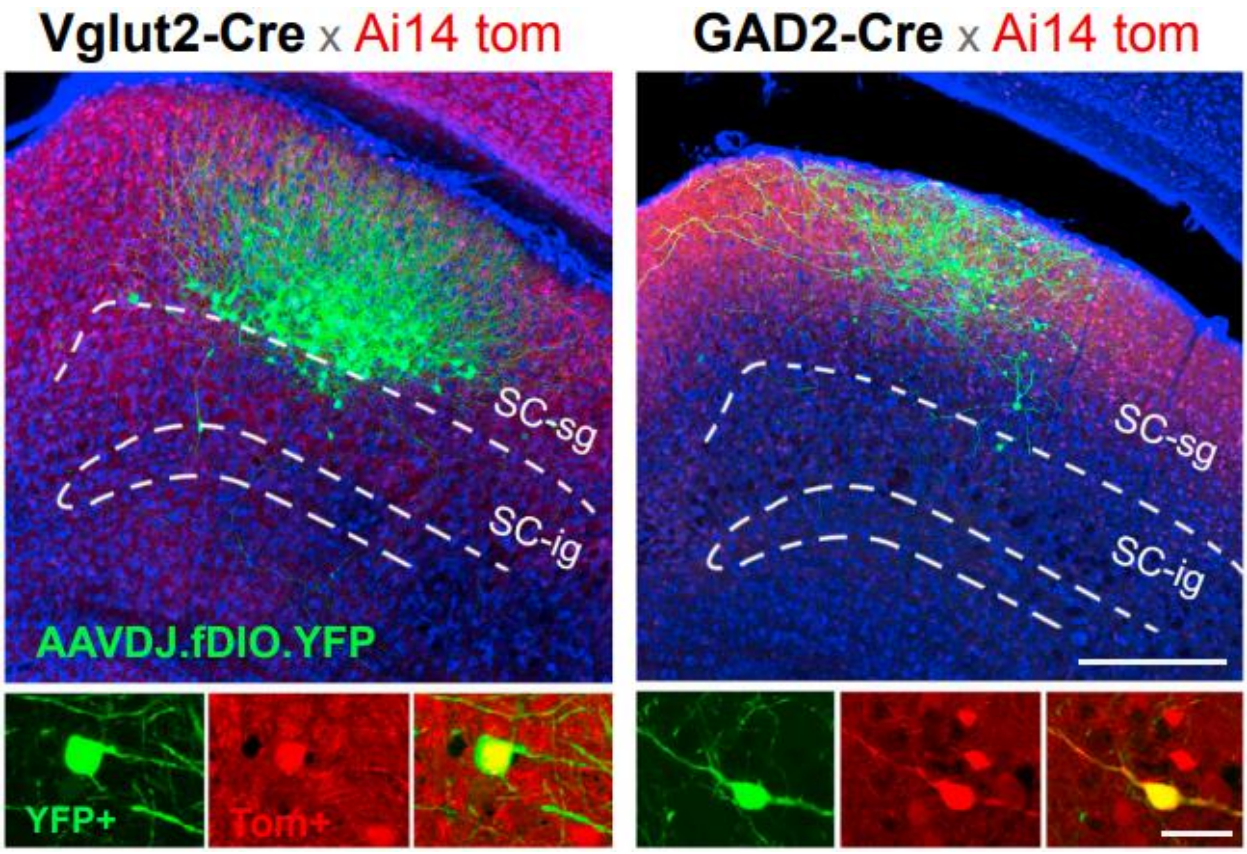

Figure 2.4: Example of anterograde transsynaptic spread of neuronal tracing viral construct[71].

2.4 Current Methods for Fabricating Tissue Engineered Small Vessels

The ductus arteriosus is an arterial blood vessel that connects the pulmonary artery to the descending aorta. Upon birth, this vessel permanently closes and shunts blood flow to the lungs. Failure to close after birth has lifelong consequences and is one of the most common human congenital heart defects[31,34,35]. In order to study the disease pathology of this highly prevalent problem, animal models have been genetically engineered to more accurately recapitulate specific

characteristics of diseases seen in humans[72–74]. For example, a rodent model was genetically engineered to cause patent ductus arteriosus in the animals[75]. This humanized mouse model was created by deleting the Jag1 gene, which encodes a Notch ligand that is expressed in smooth muscle cells and endothelial cells [76]. Thus, the mice exhibit defects in contractile smooth muscle cell differentiation in the vascular wall of the ductus arteriosus, and subsequent remodeling of the artery is prevented. While this model has provided new insight into previously unknown intracellular molecular pathways, translation of therapies developed using such animal models to clinical trials has been relative unsuccessful, and there is thus clearly a need for better models to enable high-throughput screening of potential therapeutic candidates.

One approach to enable such screening efforts is the use of 3D artificial tissue constructs that enable researchers to tune various characteristics of the environment to which embedded cells are exposed. This is a growing field that has enabled new, rapid pharmacological studies and therapeutic research. For example, a microfluidic cell stretching device was developed to study the cyclical stretching of artery smooth muscle cells to simulate pulmonary hypertension[77]. Another example is the development of multilayered 3D bioprinting with smooth muscle cells to create perfusable *in vitro* blood vessels. These cell laden channels are composed of key structural and physiological features found in native arteries[78]. There are a range of strategies for assembling perfusable constructs, each presenting its own unique advantages and challenges in their respective biomedical applications.

A recent study employed a PDMS housing with a collagen gel as a scaffold for embedded vascular smooth muscle cells (SMC)[79]. A central lumen was created using a 300μm diameter needle and lined with human umbilical vein endothelial cells (HUVECs). This simple yet versatile coculture model could be perfused, and the embedded cells demonstrated functional characteristics

similar to arteries found in the body. However, blood vessels have a distinct structural organization consisting of an inner layer of endothelium, followed by loose connective tissue, smooth muscle cells and finally collagen fibers. These structures provide stability/flexibility in the presence of pulsatile blood flow and are able to constrict and dilate when necessary[80]. In this recent work, the embedded smooth muscle cells had random orientations and remained round after several days of culture (Fig. 2.5). Thus, they did not recapitulate the contractile phenotype seen in healthy mature arteries. An *in vitro* platform that is able to sustain hDA SMCs in a perfusable 3D cell system for extended periods of time and instruct the SMCs to align would enable better therapeutic screening and could lead to more effective clinical translation.

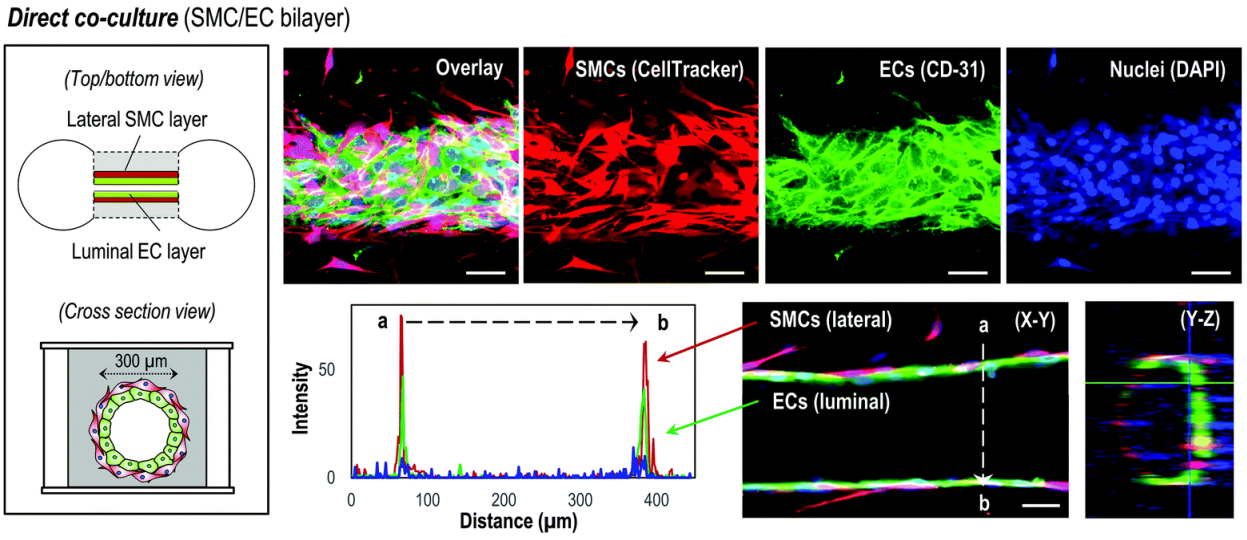

Figure 2.5: 3D coculture tubular structure perfused for 4 days[79].

CHAPTER 3

A CUSTOMIZABLE, LOW-COST PERFUSION SYSTEM FOR SUSTAINING TISSUE CONSTRUCTS

Aim 1.A: **Develop and characterize a customizable pump perfusion system and bioreactor to support controlled morphogen delivery to stem cells in a 3D hydrogel scaffold. An Arduino and stepper motor based pump system will be designed, fabricated and calibrated for precisely controlled delivery of soluble factors.**

Text for Chapter 3 taken from: O'Grady et al. A Customizable, Low-Cost Perfusion System for Sustaining Tissue Constructs. SLAS Technology. 2018

3.1 Abstract

The fabrication of engineered vascularized tissues and organs requiring sustained, controlled perfusion has been facilitated by the development of several pumps systems. Currently, researchers in the field of tissue engineering require the use of pump systems that are in general large, expensive and generically designed. Overall, these pumps often fail to meet the unique demands of perfusing clinically useful tissue constructs. Here, we describe a pumping platform that overcomes these limitations and enables scalable perfusion of large, three-dimensional hydrogels. We demonstrate the ability to perfuse multiple separate channels inside hydrogel slabs using a preprogrammed schedule that dictates pumping speed and time. The use of this pump

system to perfuse channels in large-scale engineered tissue scaffolds sustained cell viability over several weeks.

3.2 Introduction

To effectively engineer artificial tissue for research or clinical usage, culture platforms must mimic the properties of native tissue in order to achieve cellular behavior analogous to the *in vivo* phenotype. Three-dimensional (3D) tissue engineered microenvironments have allowed researchers to more accurately model native tissue and study cellular interactions that are not typically observed in two-dimensional (2D) culture systems[81,82]. For example, in 3D tissue *in vivo,* almost all cells are surrounded by other cells and reside in a complex extracellular environment; because 2D cell cultures are much simpler, they sometimes provide misleading and nonpredictive data for *in vivo* or 3D responses[83]. Platforms that enable perfusion using a scaffold that supports user controlled flow are also appealing for 3D studies, as they afford the ability to control presentation of soluble factors in either a spatial or temporal dimension, mimicking diffusion profiles documented in large tissues and organs[84]. However, the function of these perfusion systems is dependent on a reliable pumping mechanism, without which experiments involving live cell assays on a chip, shear flow studies and bioreactors with thick tissue cannot be maintained for extended culture periods[53,85,86].

For long-term cell culture within 3D scaffolds, the pumping system must be able to perfuse the scaffold in a watertight chamber without interruption, run in an incubator without undergoing corrosion, and reliably deliver fluids according to user-defined programs. However, most pump perfusion systems fail at least one of these criteria[87–89]. Perfusion systems typically require expensive pumps, and few can be utilized in a humidified incubator[16,82]. The commercially

available peristaltic pumps used in most studies are generally large in size (20-30 cm) and can weigh up to 5 kg[82]. These systems are typically kept outside of the incubator to prevent corrosion due to high humidity and heat in the incubator space. At some pumping speeds, a pump sitting outside the incubator may result in the fluid being delivered at a temperature cooler than 37°C, as well as improper gas balance in gas-permeable tubing. The ability to keep a pump inside the incubator would enable appropriate temperature and O2-to-CO2 balance in the fluid delivered to a tissue engineered scaffold. Moreover, commercial units using a single motor lack the flexibility to pump multiple independent fluid conduits at different speeds and time intervals simultaneously in an automated, user-programmed manner[90–92]. This flexibility in programming a perfusion system accommodates the changing physiological demands of different cell types within a tissue structure as it matures or ages.

In this work, we have addressed a current gap in tissue engineering platforms through the development of a customizable, inexpensive, and light-weight perfusion pump system. Using this platform, we show the ability to sustain cell viability by continuously perfusing large hydrogel scaffolds embedded with red fluorescent protein-expressing fibroblasts (RFP-expressing fibroblasts), run multiple motors at various speeds, and schedule the motors to run at various speeds. With the system we have developed, we are able to increase the complexity of perfusion experiments that may be designed with a single pump unit.

3.3 Methods and Materials

Cell culture

Red fluorescent protein (RFP)-expressing fibroblasts were purchased from Angio–Proteomie (Boston, MA), and maintained in a humidified 5% CO2-containing atmosphere (37°C).

Culture medium consisted of DMEM supplemented with 10% v/v fetal bovine serum (FBS), 50 U/mL penicillin and 50 µg/mL streptomycin, all procured from Life Technologies (Carlsbad, CA).

AutoCAD design and 3D printing

AutoCAD software (Autodesk Inc., San Rafael, CA) was used to make all 3D designs, including a housing component for the Arduino board and six EasyDriver chips, and a fluid-pump attachment (pumphead, Fig. 3.1A) for each stepper motor (StepperOnline, Nanjing City, China). Detailed instructions for assembling this system and code can be found at instructables.com (https://www.instructables.com/id/Custom-Peristaltic-Pumps-x6/), and STL files and print settings can be found at thingiverse.com (https://www.thingiverse.com/thing:2832314). The components were printed using a Dimension SST 768 3D printer (Statasys, Eden Prairie, MN) with Acrylonitrile Butadiene Styrene (ABS, Stratasys, Eden Prairie, MN). To form the rollers on the pumphead, Teflon tubing was cut to length and placed between a vertical pair of pumphead holes and secured with a Philips machine screw and hex nut.

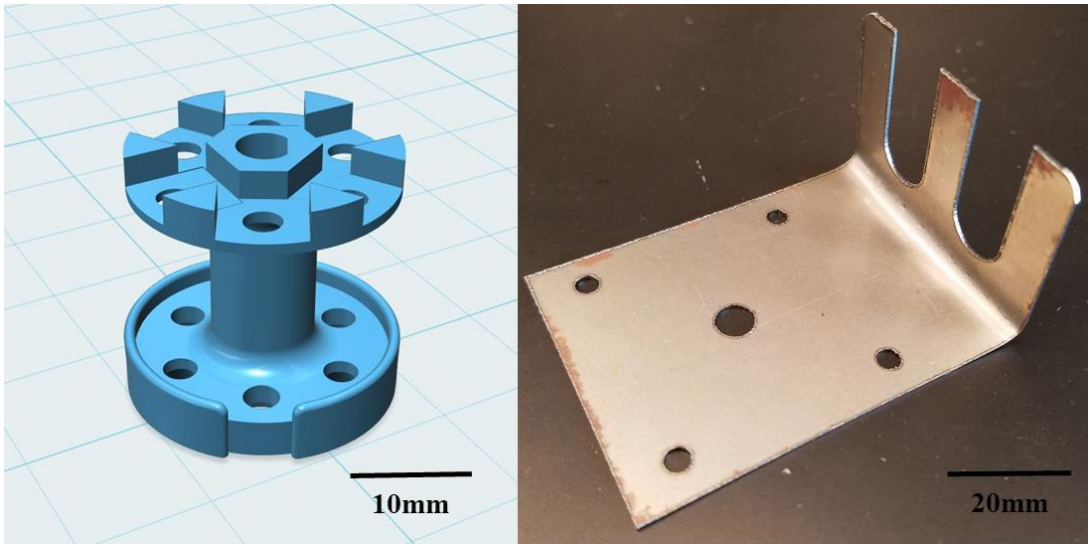

Figure 3.1: (A) AutoCAD sketch of the fluid pumphead attachment for stepper motors. There are six posts to allow for the least amount of pressure drop-off between the posts when turning. (B) Example of laser cut motor bracket after bending.

Arduino programming and speed calibration

Code for individually controlling the speed, direction, and on/off status of each of the six stepper motors was written in the Arduino program version 1.6.5. To determine a relationship between the arbitrary speeds in the Arduino code and actual flow rates, we performed a flow calibration as follows. Tygon lab tubing (1/16"ID X 1/8"OD) (Cole Palmer, Vernon Hills, IL) was cut to various lengths (98-105mm) and placed around a pumphead on a stepper motor. By varying the length of tubing placed between the bracket and pumphead, we were able to vary the tension on the tubing and thus the occlusion. This allowed us to control the volume dispensed in each pulse, and thus the flow rate for a given motor rotation rate. One side (the inlet) was placed in a 1 L beaker of water. The flow rate through the tubing at various motor speeds was measured with a Sensirion SLI-1000 flow meter (Staefa ZH, Switzerland). Each motor and tubing pair were run at 1, 10, 100, 175, 250, and 500 arbitrary units (AU, controlled by Arduino code) and the volume delivered was recorded. The relation between motor speed (AU) and flow rate was determined by a line of best fit. Ultimately, a tubing length of 102 mm was used due to the 1:1 relationship between AU and µL/min. After determining the relationship between motor speed and fluid flow rate, an additional experiment was performed to verify the ability to deliver a specified fluid volume. In this experiment, 6 motors were run at speeds of 1, 10, 100, 175, 250, and 500 AU for 10 minutes each, and the total water dispensed for each motor at a given speed was weighed on a microbalance and compared to the expected volume.

Polydimethylsiloxane (PDMS) molds for perfusion chambers

PDMS (Sylgard 184, Dow Corning, Midland, MI) was mixed in a 1:10 ratio, poured into a small paraffin mold with two 18-gauge needles placed through the sides to serve as large channels, and placed in an oven at 60°C for 2 hours. PDMS blocks were then removed from the paraffin, and needles were withdrawn and replaced with 1/16" silicon tubing (Cole Palmer, Vernon Hills, IL). A square was then cut out of the center of the PDMS block and discarded, leaving a 4-walled PDMS mold to be filled with a hydrogel. The mold was placed on a thin slab of uncrosslinked PDMS and placed in the oven for crosslinking.

Hydrogel device fabrication

Gelatin powder (Sigma Aldrich, St. Louis, MO) was dissolved in complete cell media to achieve either 5% or 10% w/v concentration and sonicated at 37° for one hour to thoroughly mix. Microbial transglutaminase (mTG; MooGloo, Eliot, ME) was dissolved in PBS to achieve 10% w/v concentration. All fluids were sterile filtered through a 0.2μm filter (Thermo Fisher, Waltham, MA). Trypsinized RFP-fibroblasts were then added to 8 mL of gelatin and 2 mL of mTG and thoroughly mixed. The mixture of gelatin and mTG was then poured into the PDMS mold over the silicon tubing (1/16") and incubated at 37°C. After the hydrogel solidified, the silicon tubing pieces were withdrawn until the end of the tubing was located just within the edge of the hydrogel. The tubing pieces (ports) were then connected to the pump tubing, and the PDMS mold containing the hydrogel was placed into a custom-built perfusion chamber. All steps were performed using sterile technique.

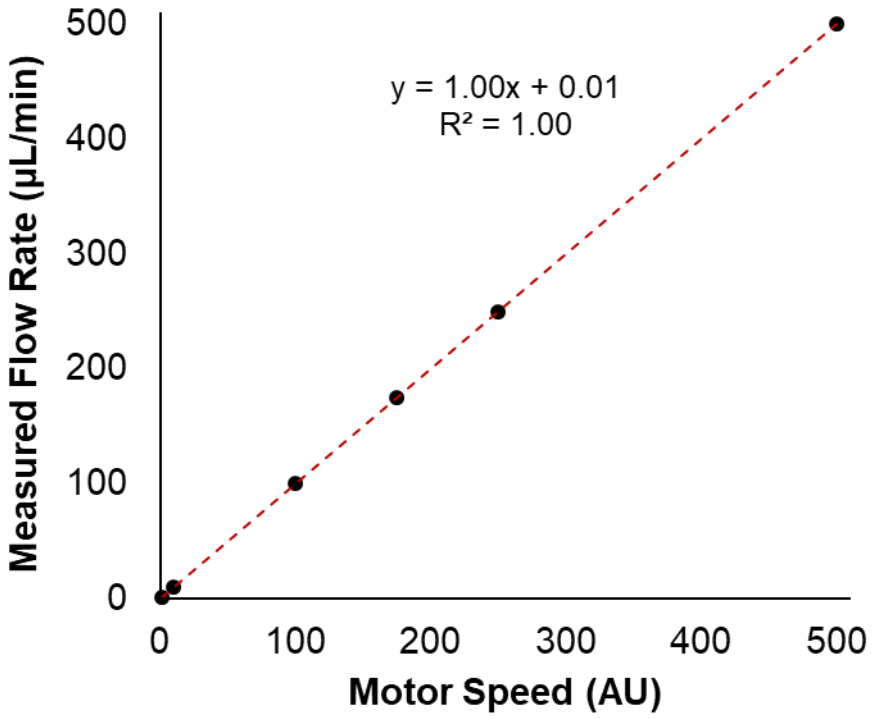

Figure 3.2: The actual fluid flow rate measured by a Senserion flow meter (µL/min) is linearly dependent on motor speed (AU) for calibrated motor-tubing pairs. Data represents mean ± standard error for 6 individual motors.

Cell viability in hydrogels

To assess long term cell viability in 3D gelatin hydrogels supported by the perfusion platform, cell-laden hydrogels were continuously perfused for 21 days, while control cell-laden gels (with identical channels) were not perfused. On the 21st day of culture, the hydrogels were perfused with 5% v/v Calcein-AM and Sytox Blue for one hour (Thermo Fisher, Waltham, MA). RFP signal from fibroblasts and intracellular Calcein from all cells were imaged on a Zeiss 710 confocal microscope (Zeiss Microscopy, Munich, Germany). Cell viability was assessed using ImageJ (National Institute of Health, Bethesda, MD). No-flow controls were performed, imaged 48 hours after seeding and stained with Calcein-AM for cell viability.

3.4 Results

Customizable 3D-printed parts and motor brackets

The six-sided pumphead was able to minimize the pulsatile effect of turning the system to pump fluids and reduce backflow into the fluid lines. The tubing collars were able to slide into the laser-cut motor brackets and sustain a desired tension on the tubing in order to deliver a consistent amount of fluid on all motors.

Customization and programming of the perfusion system

Peristaltic pumps are used to deliver fluid by alternating compression and relaxation of a tube around a pumphead. As the pumphead rotates, a seal is created between the roller and the tubing. This seal passes fluid forward, while a vacuum is created on the back end that draws more fluid forward. The ability to control the speed at which fluid is delivered is essential when operating pumps for perfusing engineered tissue. We have demonstrated that our Arduino code can be used to control six stepper motors, each at individual speeds, and allows for schedules that turn on and off motors and adjust speeds at designated times. This setup perfused hydrogels for over 21 days without any observed interruption of media delivery.

Perfusion system set-up and calibration

We sought to develop a system in which using a USB cable, users can upload code that controls the speed at which the motors turn, the amount of torque the individual motors output, the ability to increase or decrease volume rates, and the ability to turn individual motors on or off at specified times. To find the relationship between arbitrary unit speed values in the code, flow rate, and volume dispensed, we connected the inlet tubing to a water source and delivered water through a flow sensor. Using the data for 6 motors run at motor speeds ranging from 1 to 500 AU, a linear fit was applied to derive a conversion from motor speed to average fluid flow rate (Fig. 3.2). A

tubing length of 102 mm was selected for the final design because of the 1:1 relationship between AU and flow rate (in µL/min) with this setup. Beyond a motor speed of 500 AU, the relationship between AU and fluid flow rate became non-linear and eventually saturated. Using the linear fit for motor speeds from 1 to 500 AU, the resulting minimum and maximum flow rates using 1/16" ID tubing were 1 µL/min and 500 µL/min, respectively (Table 3.1). The range of possible flow rates can be adjusted to suit the specific needs of different applications by using tubing with a larger or smaller inner diameter. When used to perfuse channels in our hydrogels, we chose to use 1/16" ID tubing because the channels created in our hydrogels had a diameter of 1/16. After determining the relationship between motor speed and fluid flow rate, the accuracy of fluid volume delivery was verified by weighing water output after running each motor for 10 minutes at a given speed.

Motor Speed (AU)	Average Flow Rate (µL/min)	Standard Error (µL/min)
1	1.000	0.007
10	10.008	0.018
100	100.039	0.016
175	174.979	0.048
250	250.042	0.018
500	500.031	0.018

Table 3.1: Average flow rate for 6 motors for motor speeds ranging from 1 to 500 AU after calibration of each motor-tubing pair.

Long-term cell survival and small molecule diffusion in a hydrogel

RFP-expressing fibroblasts were embedded in 3D hydrogel scaffolds with two parallel large channels for perfusion (schematic in Fig. 3.3A). Cell-laden hydrogels were incubated in a media bath and perfused continuously by the pump system for 21 days (Fig. 3.3B). Long-term cell survival was assessed using confocal imaging of Calcein-AM delivered to RFP-fibroblasts after

21 days of incubation (Fig. 3.4). Fig. 3.4A shows RFP-expressing fibroblasts stained with Calcein-AM located approximately 3 mm deep inside the gel. Cells survived and proliferated within and across the surface of the hydrogel over the 21-day period as shown by a z-stack projection at 3 mm (Fig. 3.4B, D). Cells were imaged for RFP using a confocal z-stack on days 1, 4, 7, and 21. RFP was used to provide a total cell count for cell proliferation over the course of a 21-day period. Calcein-AM and Sytox Blue were used to assess cell viability ([Calcein-AM count] / [Calcein-AM + Sytox Blue count]) on days 1 and 21. On Day 1, 91.6% of the embedded cells were living. On day 21, 96.5% of the embedded cells were alive in the perfused hydrogel (Fig. 3.4D). Static culture of the cell-laden hydrogel resulted in nearly all cells dying (Fig. 3.4C).

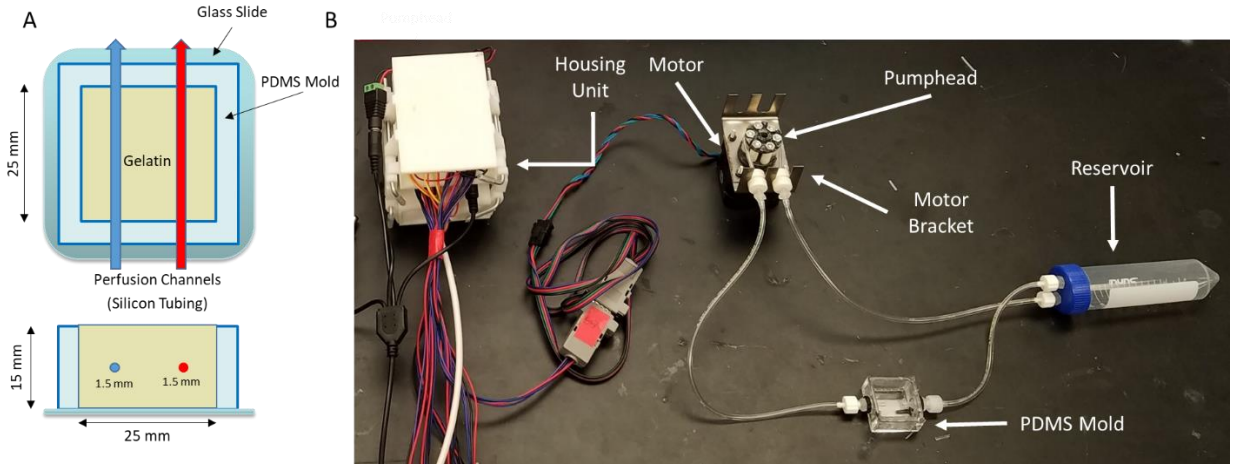

Figure 3.3: (A) Graphic representation of the hydrogel block in a PDMS mold with two perfusion channels. (B) Example of the custom perfusion system consisting of one 50ml conical tube, a PDMS mold to pour in the hydrogel, a motor with the pumphead and motor bracket and the electronics housing unit.

3.5 Discussion

In the field of tissue engineering, the development of 3D scaffolds that mimic native tissue is needed to further our understanding of the structure–function relationships in cellular

interactions [93–95]. Although tissue engineering has progressed from 2D to 3D systems in recent years [82,96,97], several limitations remain in the available to tissue engineering platforms. These limitations include the cost and size of specialized equipment (e.g. commercial peristaltic pumps, syringe pumps), compatibility of perfusion systems with incubator use, and have limited customizability and flexibility in control over the temporal and spatial presentation of fluids (e.g. media and morphogens). To address these limitations, we have developed a customizable, inexpensive, and portable pump system.

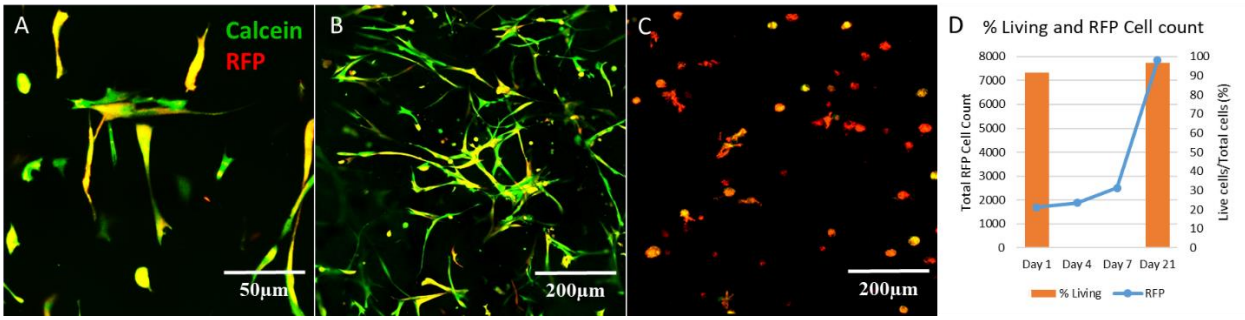

Figure 3.4: Images of gelatin hydrogel with RFP-expressing fibroblasts (Red) stained with Calcein (Green). Calcein staining of RFP-expressing fibroblasts shows cell viability on day 21 for cells embedded near the surface of the hydrogel (A) and cells approximately 3mm below the surface of the hydrogel (B). RFP-expressing fibroblasts seeded in a nonperfused hydrogel show little Calcein staining 48 hours after seeding because nearly all cells die without perfusion (C). Cell viability (% living = Calcein count / (Calcein + Sytox Blue), orange bars) and total cell count (RFP, blue line) are quantified in (D) and show an increase in the total number of cells as well as an increase in cell viability.

Commercially available pumps, such as the Harvard Apparatus Standard Infusion/Withdraw PHD ULTRA syringe pump, Thermo Fisher FH100M Multichannel Pump System, and the Ismatec IPC Low-Speed Digital Peristaltic Pump have been used successfully in tissue engineering applications[57,82,98]. However, there are drawbacks to each of these models. The PHD ULTRA syringe pump is a highly accurate system (0.25% of desired rate of delivery) with a maximum flow rate of 216 mL/min (140 mL syringe) and minimum flow rate of 1.56 pL/min (0.5 mL syringe). This pump system can be scheduled to perfuse a specific amount and

reverse to pull media through a system and back into the syringe. However, this device is 4.5 kg, large, can run 2 syringes at only one rate, and costs several thousand dollars. The FH100M multichannel pump system (Cole Palmer, Vernon Hills, IL) is programmable, can support up to 12 tubes, has a lower pulsation because of the nature of the rollers, has a valveless diaphragm, and is reversible with a maximum rate of 760 mL/min and minimum rate of 2 µL/min [98]. However, it is expensive ($2000-4000), large, and it can run only one speed for all 12 channels. The Ismatic IPC low-speed digital peristaltic pump (Cole Palmer, Vernon Hills, IL) is accurate (~1% of desired rate of delivery), can be scheduled, and can support up to 24 tubes. However, it weighs 4.5 kg, has large dimensions, can only run all 24 channels at one speed, and is expensive ($5000-7000). Recently, alternatives to these large pump systems have become available, such as the MP2 (Elemental Scientific, Omaha, NE) and nano3 (Elemental Scientific, Omaha, NE) peristaltic pump systems. These pumps have the advantage of being more compact size, cheaper in price and just as accurate as the models previously mentioned. The MP2 allows for multiple tubing attachments to a single pumphead to run at a one, programmable rate and the nano3 pumps consist of three independent pumpheads that can be programmed to run at three independent speeds. However, it would require six of the MP2 systems or two of the nano3 to match our system in terms of the number of individually controlled channels. The comparison of these commercial systems to our system is summarized in Suppl. Table 2.

In contrast, our pump system (composed of a compact, 3D-printed housing unit, stepper motors, EasyDriver chips, a power supply, and an Arduino board) weighs 0.42 kg and costs approximately $122 per unit. Additional common electrical supplies used in building our pump system (e.g. wiring, solder, serial connectors) cost approximately $200, but these stock supplies can be used for building at least 4 units. While this system requires more effort to assemble

compared to an off-the-shelf pump, the cost savings are significant and a single unit can be scheduled to deliver fluid to up to 12 separate hydrogels at 6 speeds (2 hydrogels per motor) or deliver fluid to multiple ports in fewer hydrogels. The Arduino board enables control over all six motors. While the Arduino and motor driver electronics are located outside of the incubator, the motors and associated pump hardware are placed in the incubator, resulting in a smaller footprint within the controlled incubator environment as compared to placing a commercial system in the incubator. In our lab, a single pump unit consisting of 6 stepper motors placed inside the incubator routinely runs without interruption or failure for months (the timeframe of the desired experiment). The code used for this system allows the user to run specific sets of motors for a specified period of time and then shut off, run motors at several speeds for a set length of time, or run motor/speed programs for a specified number of loops. This ability to control the number of motors, the schedule at which they run, rate at which they deliver fluid, and the number of cycles enables the user to set up complex perfusion experiments that run reliably for extended periods of time (on the order of months). This is a useful tool when studying the dynamics of cells requiring highly coordinated delivery or removal of specific environmental cues.

In this Chapter, I have described the construction of the pump system as well as the customizable programming that enables perfusion of 3D scaffolds with precise schedules and fluid flow rates. Each stepper motor is calibrated to determine the relationship between the program input values to flow rates (Table 1) and the corresponding actual volume dispensed (Suppl. Table 3). Our calibration experiments showed that our system can consistently deliver fluids at a minimum rate of ~1 µL/min (±0.0067) to a maximum rate of ~500 µL/min (±0.018) (Suppl. Table 3). However, the maximum and minimum rates increase and decrease with a change in the size of tubing (Suppl. Table 1). This range of flow rates is useful for tissue engineered scaffolds with

various cell types that may need high rates of fluid flow, such as human umbilical vein endothelial cells (HUVECs)[99], or cell types that do not require high flow but need constant delivery of media, such as mesenchymal stem cells (MSCs)[100].

We demonstrated the utility of the pump system by perfusing 3D gelatin scaffolds containing cells. In experiments with RFP-expressing fibroblasts embedded in these hydrogels, cell viability within the hydrogel was maintained for 21 days as evidenced by live-cell staining (Calcein) and spreading of fibroblasts (Fig. 4.4). The perfusion of large hydrogels and cell viability experiments demonstrate that our perfusion system is an effective means of sustaining cell viability for extended periods of time.

Overall, these results demonstrate that our pump system has a high level of customization compared to other easily obtained or constructed pumps. It can be used for automated and accurate control of fluid delivery to maintain cell viability through continuous perfusion.

3.6 Acknowledgments

This research was funded and supported by NSF BMAT 1506717 (LMB) and a NARSAD Young Investigator Award from the Brain and Behavior Research Foundation (ESL).

CHAPTER 4

SPATIOTEMPORAL CONTROL AND MODELING OF MORPHOGEN DELIVERY TO INDUCE GRADIENT PATTERNING OF STEM CELL DIFFERENTIATION USING FLUIDIC CHANNELS

Aim 1.B: Create and validate a computational model for temporal delivery of soluble factors to cells in a 3D hydrogel scaffold via embedded perfusion channels.

Aim 2: Differentiate mesenchymal stem cells into multiple tissue types in a single hydrogel system using opposing gradients of signaling factors controlled by a pump perfusion system and spatially tune differentiation based on varying morphogen concentration

Text for Chapter 4 taken from: O'Grady et al. Spatiotemporal Control and Modeling of Morphogen Delivery to Induce Gradient Patterning of Stem Cell Differentiation Using Fluidic Channels. Biomaterials Science. 2019

4.1 Abstract

The process of cell differentiation in a developing embryo is influenced by numerous factors, including various biological molecules whose presentation varies dramatically over space and time. These morphogens regulate cell fate based on concentration profiles, thus creating discrete populations of cells and ultimately generating large, complex tissues and organs. Recently, several in vitro platforms have attempted to recapitulate the complex presentation of extrinsic

signals found in nature. However, it has been a challenge to design versatile platforms that can dynamically control morphogen gradients over extended periods of time. To address some of these issues, we introduce a platform using channels patterned in hydrogels to deliver multiple morphogens to cells in a 3D scaffold, thus creating a spectrum of cell phenotypes based on the resultant morphogen gradients. The diffusion coefficient of a common small molecule morphogen, retinoic acid (RA), was measured within our hydrogel platform using Raman spectroscopy and its diffusion in our platform's geometry was modeled using finite element analysis. The model of spatial gradient formation was validated in a cell-free hydrogel, and temporal control of morphogen gradients was then demonstrated using a reporter cell line that expresses green fluorescent protein (GFP) in the presence of RA. Finally, the utility of this approach for regulating cell phenotype was demonstrated by generating opposing morphogen gradients to create a spectrum of mesenchymal stem cell differentiation states.

4.2 Introduction

Biological development relies upon highly regulated local concentrations of proteins and/or small molecules. These so-called morphogens can be interpreted by cells based on concentration (spatial dependence), as well as the amount of time cells are exposed to each signal (temporal dependence). The integration of these cues determines cell fate and the formation of large, complex tissues and organs. One example of morphogen-guided embryonic development is the spatial patterning of the spinal cord, prosencephalon, mesencephalon and rhombencephalon regions of the developing CNS[44,101]. Each region is controlled by simultaneous differentiation based on multiple opposing gradients to produce spatially organized domains. Another example can be found in the differentiation of the mesoderm layer into cardiac tissue in response to

transforming growth factor β (TGFβ) signaling3, where the cells sub-differentiate into atrial and ventricular cardiac cells to form the atrium and ventricles of the heart[102–104]. Moreover, cell differentiation is not limited to embryonic development. In the adult intestine, mitotically active, undifferentiated stem cells repopulate the epithelial lining of the intestine to renew, repair and effectively absorb food while maintaining a barrier against potentially harmful microorganisms. In response to opposing gradients of Wnt and bone morphogenic protein (BMP) signaling, spatially organized domains of the epithelial layer arise to form the crypts and villi of the intestinal wall[105–107].

Nearly every organ system in the body relies on morphogen signaling for proper differentiation and organization. Recreation of these developmental patterning events in human stem cells, from both embryonic and adult sources, is highly desirable for applications in disease modeling and regenerative medicine. Although patterning events involving temporal dependence have been reproduced in static well-plate cultures[108–110], those involving spatial morphogen gradients require more intricate engineering solutions[111–114].

Few platforms have been able to produce morphogen gradients over extended periods of time and across a large scale (on the order of centimeters) to guide differentiation and eventual proliferation and self-organization[20,110]. A large-scale culture platform is particularly necessary for long-term studies, as smaller platforms cannot accommodate continuous cell growth in the scaffold. One early approach to producing spatially-varying differentiation employed microspheres loaded with various concentrations of BMP2 and insulin-like growth factor 1 (IGF-1). These microspheres were embedded in alginate hydrogels, where one variety of microsphere (poly(lactic-co-glycolic acid)) released a large quantity of growth factor over a short period of time, and the other (silk) provided a sustained release over an extended period of time (weeks)[22].

Additionally, the researchers were able to include several different morphogens in each variety of microsphere, thereby creating gradients of multiple species within a single scaffold. Many other follow-up studies have successfully used this approach to create morphogen gradients with various growth factors for tissue regeneration[115–117]. However, due to eventual depletion of the morphogens, this approach is unable to sustain a heterogenous morphogen distribution for extended periods of time, as the crosslinked hydrogel cannot be reloaded with fresh microspheres without compromising the structural integrity of the matrix. In addition, because all parameters regarding the release rate of morphogens from the microspheres were preprogrammed prior to the experiment, it is difficult to produce more complex gradients (e.g. generate periodic concentration waves) after the microspheres have been loaded into the hydrogel.

Microfluidic systems provide an alternative means of delivering morphogens to cells in a scaffold and can be set up to maintain long term concentration profiles. In the past decade, several such platforms have been developed to study intracellular pathways involved in stem cell differentiation[118]. The use of microfluidics provides researchers with unprecedented control over the delivery and removal of soluble compounds to three-dimensional (3D), cell-laden scaffolds, and has the potential to create complex gradients of morphogens[119,120]. As a result, these systems have enabled physiologically relevant models for high throughput drug screening and a better understanding of the pathophysiology associated with several diseases[54,56,58,121]. One early approach utilized hydrogels with embedded microfluidic channels, wherein soluble factors diffused through the hydrogel to cells seeded on the surface. This configuration was used to deliver RA to a flat surface, creating gradients to study the differentiation of embryonic stem cells (ESCs) into neurons[120]. A more complex platform, consisting of four microfluidic channels adjacent to the top, bottom, left, and right sides of a cell-laden gel, has also been used to

create four separate gradients (RA, Sonic hedgehog, BMP, and FGF) to study neural tube patterning[101]. Overall, these creative approaches have made significant strides to the field by demonstrating the importance of controlled multifaceted morphogen presentation; however, they remain small in scale and lack extended temporal control due to the relatively short time frame (days) in which cells reach 100% confluence within the scaffold.

We sought to develop an experimental platform that provides spatial and long-term (months) temporal control of morphogen delivery in a hydrogel that is large enough to accommodate stem cell differentiation for patterning larger tissue structures. This system provides the ability to dynamically deliver and replenish morphogens via fluidic channels to a large cell-laden hydrogel, visualize cellular responses due to morphogen gradients, and run experiments over extended time periods. To validate this approach, we first measured the diffusion coefficient of RA with Raman spectroscopy, modeled its diffusion pattern using COMSOL, and verified the accuracy of this model by measuring RA concentrations in samples extracted from various locations in a hydrogel. Next, we assessed control of RA delivery in space and time using an RA-sensitive reporter cell line. Finally, using mesenchymal stem cells (MSCs) as a model system, we produced a spectrum of differentiation states by delivering two different morphogens from two parallel channels, thereby creating two opposing gradients. By changing the concentration of the morphogens in the fluidic channels, we demonstrate altered distributions of cell phenotype within the gel. Overall, these proof-of-principle studies lay the groundwork for more complex patterning applications involving stem cells.

4.3 Methods

Bioreactor system fabrication

In order to ensure reproducibility of the bioreactor construction, namely channel and port locations, a jig was designed using Creo Parametric and 3D printed from ABS (Acrylonitrile butadiene styrene, Stratasys F170) (Fig. 4.1). This jig was used to guide the drilling of two 1/4" holes on each end of the polystyrene box with 11 mm separation between the holes on each face. The drilling was completed using a mill and a plastic cutting drill bit (McMaster-Carr, 27465A84, specialized drill bit designed to avoid cracking plastic). The barbed end of female Luer bulkheads was cut off, and bulkheads were mounted to each of the four holes in the polystyrene box using locking nuts. A 1" piece of square stock was placed in the middle of the polystyrene box in contact with the four bulkheads. PDMS (10:1 PDMS:initiator) was then poured into the space between the square stock and the polystyrene box. After cross-linking the PDMS "walls" in an oven at 60C for 2 hours, the square stock was removed and 1.5 mL of PDMS was added to the bottom of the box and crosslinked to completely coat the inside of the polystyrene box with PDMS. The PDMS was used to act as a frame for the gelatin to adhere and serve as a gasket to prevent leaking. Finally, the bulkheads were removed and the resulting PDMS frame and polystyrene box were sterilized in bleach for 30 minutes then ethanol for 1 hour. The box and PDMS were then transferred to the biohood and were placed in a DI water bath for 1 hour. This was repeated 3 times. The devices were then dried on a heated surface (37C). After drying, the PDMS frame was placed back into the polystyrene box and new, sterile, female Luer bulkheads (with barbed end intact) were screwed into the four embedded locking nuts. The embedded locking nuts ensure that the integrity of the ports is maintained for several weeks of perfusion. Additionally, the hydrogel itself sticks to the PDMS walls, so the gelatin does not pull away from the ports and the channels do not leak when

perfused. Sterile 1/16” silicon tubing (Cole Palmer) was inserted through each pair of bulkheads to create a mold for the two parallel channels (9 mm apart) to be formed during hydrogel fabrication. For experiments, the PDMS-lined polystyrene box was placed in a larger polystyrene box to further protect the hydrogel from contamination. The larger box also contained the two media reservoirs (50 mL conical tubes with two holes drilled into the cap for tubing) for continuous, nonmixing, recirculation of media. Individual bioreactors were fabricated for each experiment; the polystyrene box, PDMS frame, and tubing were not re-used.

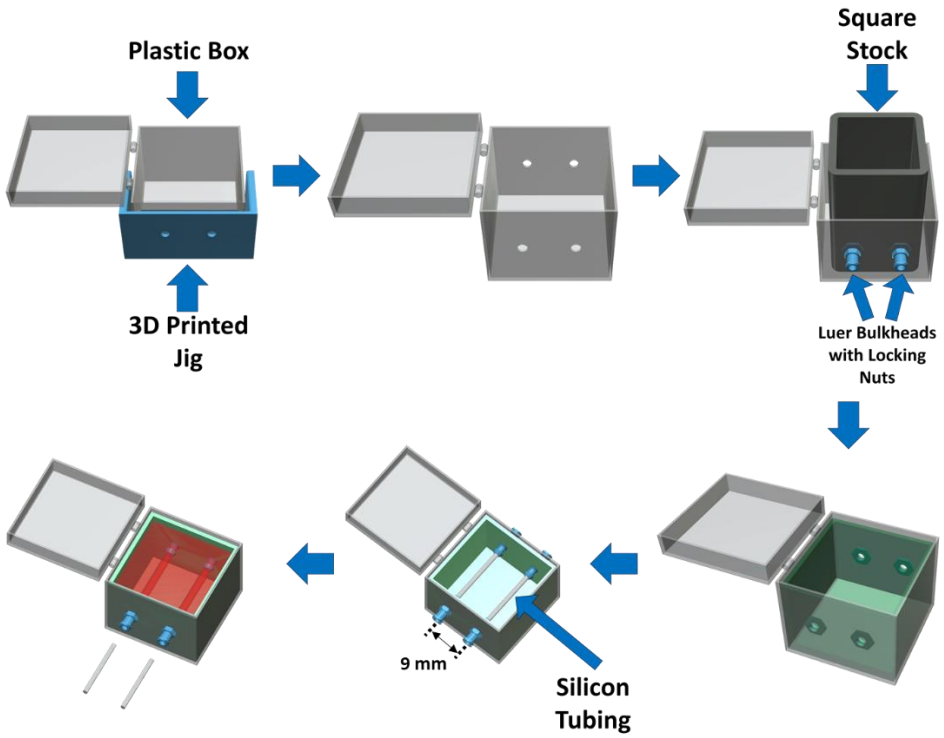

Figure 4.1: Bioreactor fabrication and assembly process. First, a 3D-printed jig is used to guide drilling of holes for the perfusion ports, which are then fitted with Luer bulkheads and locking nuts. One-inch square stock is placed within the outer box in contact with the Luer bulkheads to provide a temporary mold for a PDMS layer in which the locking nuts are embedded. The bottom of the box is also coated with PDMS to complete the inner frame. After the PDMS frame has crosslinked, silicon tubing is inserted to form a mold for two parallel perfusion channels located 9 mm apart. Finally, a hydrogel solution (with or without cells) is poured into the PDMS frame, the hydrogel is crosslinked, and the silicone tubing pieces are removed to leave embedded, parallel channels within the hydrogel. The overall hydrogel dimensions are 25 x 25 x 25 mm.

Cell culture and transfection

RFP-expressing fibroblasts and human bone marrow-derived MSCs were purchased from Angio-Proteomie (Boston, MA) and Lonza (Allendale, NJ), respectively. The cells were maintained in a humidified 5% CO2 environment at 37°C. MSC maintenance media consisted of DMEM supplemented with 20% v/v fetal bovine serum (FBS), 50 U/mL penicillin, and 50 μg/mL streptomycin, all procured from Life Technologies (Carlsbad, CA). Red fluorescent protein (RFP)-expressing fibroblasts were transfected with the pGreenFire1-RARE Lentivector virus[122–125] (System Bioscience, Palo Alto, CA). RARE-RFP-fibroblasts were seeded at 1 million cells/ml in a 6-well plate, where a multiplicity of infection of 5 was used to infect the cells. After 48 hours, cells were treated with 10 nM of RA (20 mg/ml RA in DMSO stock solution) and imaged for compromised green fluorescent protein (GFP; 2-hour half-life) expression to verify successful transduction.

Hydrogel scaffold fabrication for perfusion

Hydrogels were formed inside the PDMS frame as described previously, with the modification of using two isolated embedded prefusion channels[126]. Briefly, gelatin powder (Sigma Aldrich, St. Louis, MO) was dissolved in MSC maintenance media at a final concentration of 10% w/v. After 1 h of sonication at 37°C, the gelatin solution was sterile-filtered (0.2 μm, Thermo Fisher, Waltham, MA) and maintained at 37°C in a water bath. A 20% w/v solution of microbial transglutaminase (mTG, MooGloo, Eliot, ME) in PBS was prepared separately and sterile-filtered. The sterile mTG and gelatin solutions were then added to a conical tube containing

a pellet of trypsinized RARE-RFP-fibroblasts (3 million cells/mL) or MSCs (3 million cells/mL) in a 1:9 mTG to gel ratio for a total volume of 20 mL. The cells were resuspended by manual pipetting, and the solution was immediately poured over the silicone tubing in the PDMS frame. The bioreactor was incubated at 37°C for 30 minutes to crosslink the hydrogel. The silicone tubing pieces were then withdrawn from the hydrogel, leaving two parallel channels aligned with the Luer bulkheads (Fig. 4.2A). Autoclaved Tygon (E-3603) lab tubing (1/16 in. ID × 1/8 in. OD) (Cole Palmer, Vernon Hills, IL) was then washed 3 times with DI water and connected to the Luer bulkheads, and the bioreactor was perfused using a peristaltic pump perfusion system (Fig. 4.2B)[126].

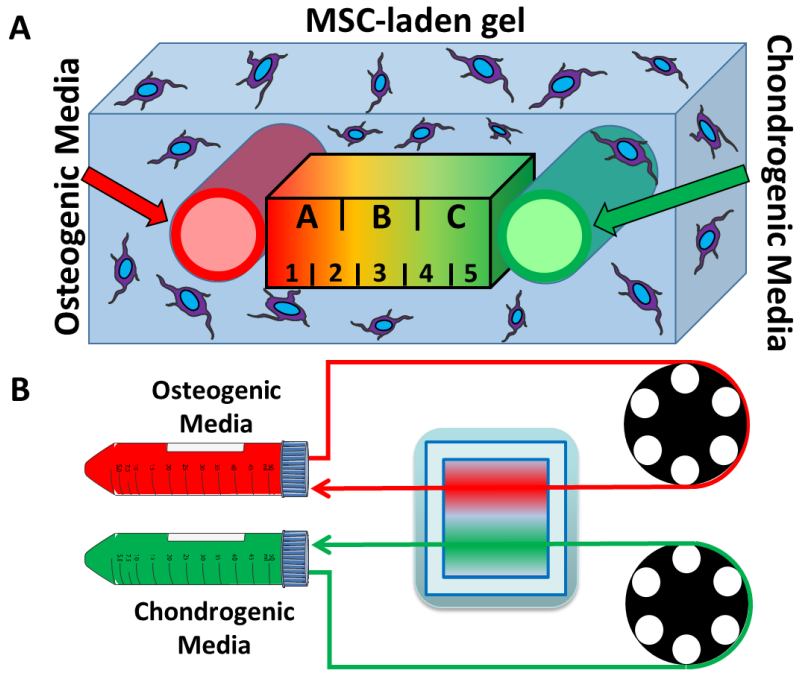

Figure 4.2: A closed-circuit microfluidic hydrogel platform allows for dual delivery of osteogenic and chondrogenic media. (A) An illustration of the cross-section between the two parallel channels. The area was divided into three regions, each with a width of 3mm (regions A-C), for the Western blot study and divided into five regions, each with a width of 1.8mm (regions 1-5),

for the immunofluorescence study. (B) An illustration of the perfusion setup shows how the media is drawn from a conical tube reservoir, around a pumphead, through the gel, and back into the reservoir.

Measuring the diffusion coefficients of small and large compounds

For measurement of the diffusion coefficient of RA (Sigma Aldrich, St. Louis, MO) in a gelatin hydrogel, 64x27x1.2mm glass slides were used as a mold. First, 5 glass slides were glued and stacked on top of each other and allowed to cure at 60C. The stack of slides was then placed in the center of a 100mm petri dish, where PDMS was poured over the glass slides and filled until the slides were thoroughly covered. This was allowed to crosslink for 1 hour at 60C, after which the crosslinked PDMS was cut out of petri dish. The glass slides were removed to create a well for the gel. On one of the short ends of the PDMS mold, two holes were created using a 1mm biopsy punch, and silicon tubing was placed to serve as ports for recirculating RA in DI water at a final concentration of 2μM. The same stack of glass slides was then placed vertically into the PDMS chamber against the face where the biopsy punches were made. A 1:9 solution of mTG to gelatin was mixed in DI water and poured into the mold. After 30 minutes of crosslinking at 37C, the glass slides were removed, leaving space for an RA reservoir on one end of the hydrogel.

For the RA diffusion experiment, the PDMS mold containing a crosslinked hydrogel was placed on the confocal Raman microscope stage (inVia Renishaw) and the laser was focused below the surface of the hydrogel at a location 0.2cm from the gel/reservoir interface. An external reservoir of 2μM RA in DI water was connected to the reservoir in the PDMS frame via a custom-built peristaltic pump described previously[58]. The internal reservoir was filled with 2μM RA and Raman spectra acquisition began immediately (Fig. 4.3A). The peristaltic pump recirculated RA from the large external reservoir, and Raman spectra were recorded every 30 minutes for 5 hours (532nm laser, 50% power, 5X magnification, 5 second acquisition time, grating 2400 l/mm). The

peak Raman intensity between 1590-1595cm^{-1}, corresponding to the RA C=C bond stretching Raman signal in our hydrogel, was plotted as a function of time after background subtraction (Fig. 4.3B). The data from 5 independent experiments were combined and analyzed with a modified equation developed for the diffusion of semi-infinite media by Crank[127,128]. At time equal to 0, the RA concentration throughout the gel is 0 and the gel/reservoir interface concentration of RA was maintained at C_0. As RA molecules diffuse into the gel, the concentration dependence on the distance in the gel from the gel/reservoir interface, defined as x = 0, is given by the equation below:

$$C = C_o \operatorname{erfc}\left\{\frac{x}{2\sqrt{(D_t t)}}\right\} + B,$$

where C is the concentration at distance x from the interface at an elapsed time t, and D_t is the mutual-diffusion coefficient. An additional constant term, B, was added to account for a small offset in the y-intercept, due to imperfect background subtraction. The data were fit using a nonlinear least-squares solver (*lsqcurvefit* function) in Matlab (Mathworks, Natick, MA).

Diffusion of a larger compound, fluorescently-labeled 10 kDa dextran (Thermo Fisher, Waltham, MA) was measured in a hydrogel with two perfusion channels fabricated as described in Fig. 4.1 without inclusion of cells. Syringe pumps were used to perfuse the left channel with 1 mM Texas red 10 kDa dextran and the right channel with 1 mM FITC 10 kDa dextran at 300 µl/minute (Fig. 4.4A). The fluorescence intensity of the Texas red dextran was measured 0.2 cm from the left channel every minute for 60 minutes using a confocal microscope (Zeiss LSM 710). To determine a diffusion coefficient, the resulting data were then fit using the above diffusion equation. Additionally, the entire length between the red and green channels was imaged after 60 minutes to map out the extent to which each variety of dextran diffused.

COMSOL model of diffusion and experimental validation

Diffusion of RA was modeled using the Transport of Diluted Species physics interface of the Chemical Reaction Engineering module included in the COMSOL Multiphysics 5.3 modeling suite (COMSOL AB, Stockholm, Sweden) with the experimentally-measured diffusion coefficient as an input. A model of diffusion in the hydrogel was generated using 8 mM RA in a channel, and the simulation was run to a 24-hour timepoint. At the 24-hour mark, the RA concentrations in the gel at 1 mm, 2 mm, and 3 mm from gel/reservoir interface were obtained. In order to experimentally verify the simulation, a gel was cast in the same geometry (using PBS instead of complete media for simplicity). The reservoir was then filled with recirculating 8 mM RA. After 24 hours, the gel was cross-sectionally cut into 10 equal sections. A 0.5 mm biopsy punch was used to punch out gel at distances of 1 mm, 2 mm, and 3 mm from the gel/reservoir interface. The punches were then placed into a sterile 0.45 μm pore centrifuge tube filter (Spin-X Centrifuge Tube Filters, Corning, New York, NY) and spun at 10,000xG to extract the liquid, and the RA concentration in the liquid phase was determined using a microplate reader (Synergy H1 Multi-mode Microplate Reader, BioTek) to measure absorbance at 350 nm.

The diffusion of 10 kDa dextran from two parallel channels in a hydrogel was modeled using the same COMSOL settings described for RA with the experimentally-measured diffusion coefficient as an input, and the simulation was run for 60 minutes. At the 60-minute mark, the dextran concentrations in the gel at 1 mm, 2 mm and 4 mm distances from the right channel (10 kDa FITC dextran) were obtained. In order to experimentally verify the simulation, a parallel perfusion channel hydrogel was cast (using PBS instead of complete media for simplicity). Each parallel channel was then connected to a syringe containing either 1mM of 10 kDa Texas red

dextran or 10 kDa FITC dextran. The hydrogel was then perfused at a rate of 300 µl/minute for 60 minutes. A 0.5 mm biopsy punch was used to punch out gel at distances of 1 mm, 2 mm, and 4mm from the right channel (FITC dextran side). The punches were then placed into a sterile 0.45 µm pore centrifuge tube filter (Spin-X Centrifuge Tube Filters, Corning, New York, NY) and spun at 10,000xG to extract the liquid, and the dextran concentrations in the liquid phase were determined using a microplate reader (Synergy H1 Multi-mode Microplate Reader, BioTek) to measure fluorescence using the FITC filter and the Texas red filter.

Validation of temporal control of morphogen delivery

Temporal control of a morphogen gradient was validated using the RARE-RFP-fibroblasts. These RA reporter cells were embedded in hydrogels in the dual port perfusion bioreactor for real-time visualization of the cellular response to the diffusion of RA. First, the left port of the gel was perfused with media containing 2 µM RA, while the right port was perfused with standard growth media. The hydrogel was perfused for 1 hour to allow for RA diffusion before the perfusion reservoir was changed to standard growth media. The RA-responsive GFP expression and the constitutively active RFP expression in the RARE-RFP-fibroblasts were then visualized using confocal microscopy. After 24 hours of perfusion with standard growth media in both channels, the right port was perfused with 2 µM RA in media while the left port received standard growth media. GFP and RFP expression were visualized again after 1 hour of RA diffusion from the right channel. Then, both channels were perfused with 2 µM RA after another 24-hour period of standard media perfusion and confocal microscopy was performed a third time after 1 hour of RA diffusion from both channels. Finally, after 24 hours of perfusion with standard growth media, GFP and RFP were visualized to confirm no GFP was being expressed. Survival of cells located in the entire region between the perfusion channels was verified by perfusing an RFP-fibroblast-

laden hydrogel with standard media for 14 days, then staining the cells with Calcein (ThermoFisher) and Sytox blue (ThermoFisher) to identify live and dead cells, respectively. The Calcein-AM and Sytox Blue images were analyzed in ImageJ to assess cell viability ([Calcein-AM count] / [Calcein-AM + Sytox Blue count]) on day 14.

Formation of gradients of MSC differentiation

To demonstrate heterogeneous morphogen presentation, one of the two fluidic channels were perfused with osteogenic media and the other was perfused with chondrogenic media. Osteogenic media consisted of high-glucose DMEM, 10 ng/ml BMP-2, 0.1 μM dexamethasone (Sigma Aldrich), 10 mM β-glycerol phosphate (Sigma Aldrich), 0.2 mM ascorbic acid (Sigma Aldrich), 20% FBS (ThermoFisher), and 1% Pen/Strep[129] (ThermoFisher)[62]. Chondrogenic media consisted of high-glucose DMEM with sodium pyruvate (Sigma Aldrich), 10% ITS Premix (ThermoFisher), 0.1 μM dexamethasone, 1 μM ascorbic acid, 4% Proline (Sigma Aldrich), 20 ng/ml or 10 ng/ml TGFβ-1 (Peprotech, Rocky Hill, NJ), 20% FBS, and 1% Pen/Strep[130]. After the cell laden hydrogels were crosslinked, the perfusion began immediately at a rate of 300 μl/minute. The osteogenic and chondrogenic media in the conical tube reservoirs were replaced with fresh differentiation media every 7 days, and the hydrogels were perfused continuously for 35 days.

On day 35, hydrogels were divided into two pieces by slicing the gel in the center, perpendicular to the two perfusion channels, so that each piece contained both osteogenic and chondrogenic regions. One half of the hydrogel was further subdivided into 5 sections using a razor to make cuts in the same direction as the initial cut (perpendicular to the channels). The intact half of the hydrogel was removed from the PDMS frame and immediately placed in a bath of 4% paraformaldehyde on a rocker for fixation prior to immunofluorescence staining. The 5 thin

sections of the other half of the hydrogel were removed from the PDMS frame and a 3 mm biopsy punch was used to collect three samples from each section. The samples were located 1) adjacent to the osteogenic channel, 2) at the midpoint between the two channels, and 3) adjacent to the chondrogenic channel. This resulted in 5 samples for each of the 3 locations, and the samples from a single hydrogel were combined for use in a Western blot (i.e. 5 biopsy samples collected for each location from 10 hydrogels resulted in n=10).

Predefined sections of the hydrogel designated for Western blot were cut and dissolved in Collagenase Type IV (2% W/V) for 1 hour. The resulting dissolved gel-cell mixture was centrifuged at 400*g to pellet the cells. The pellet was washed 3 times with DPBS (without magnesium or calcium) with centrifugation. The pellet was then resuspended in RIPA buffer (Sigma Aldrich) with 1:100 v/v protease and phosphatase inhibitors (Sigma Aldrich) for 5-10 minutes on ice followed by centrifugation at 12,000*g for 15 minutes at 4C. The supernatant was then removed and frozen at -20C for future use.

Protein concentrations were determined using the Pierce BCA Protein Assay Kit (ThermoFisher Scientific). 10 µg of protein were pipetted from each protein sample, and the appropriate amount of RIPA buffer, Laemmli buffer (BioRAD), and betamercapto ethanol (Sigma Aldrich) were added to yield a total volume of 25 µl. These samples were boiled at 95C for 5 minutes, and then cooled on ice. 4-20% Criterion TGX Precast Midi Protein Gels (BioRAD) were pre-run at 70V for 20 minutes in running buffer (product info) during this boiling and cooling period. Boiled protein samples and appropriate loading ladder were added to the gel and was then run at 80V until the protein samples had run down the majority of the gels. Gels were then transferred to nitrocellulose membranes on an iBlot 2 dry blotting system (ThermoFisher Scientific) according to the manufacturer's protocol.

The membrane was blocked with TBS-based Odyssey blocking buffer (Li-COR Biosciences) for 30 minutes at room temperature on a shaker plate. Primary antibodies were dissolved in the Odyssey blocking buffer with 0.05% Tween 20 (Sigma Aldrich) at the following concentrations: RUNX2 (1:1000, Abcam ab23981), SOX9 (1:1000, Cell Signaling Technology, 82630S), and GAPDH (1:5000, Cell Signaling Technology, 14C10). Primary antibody incubation was performed at 4C overnight on a shaker plate. Membranes were then washed with TBS (product info) containing 0.05% Tween 20 (3 washes for 5 minutes each on a shaker plate). Appropriate Li-COR 800CW secondary antibodies were diluted in TBST at 1:15,000, and then incubated on the membranes for 2 hours at room temperature on a shaker plate. Membranes were again washed with TBST (3 washes for 5 minutes each on a shaker plate) before being imaged on a Li-COR Odyssey scanner, and imaging processing was performed in the manufacturer's software.

After 7 minutes in the paraformaldehyde bath, the half of each hydrogel designated for immunofluorescence was further subdivided into 5 equal sections and washed 3 times with PBS. The slices were then placed in a 5% normal goat serum for blocking and membrane permeabilization. After 1 hour of blocking, 10µl of Runx2 conjugated Alexa fluor 647, Sox9 conjugated Alexa fluor 488, Rhodamine Phalloidin (actin), and Hoechst 33342 (nuclear stain) were added to the blocking solution and allowed to bind overnight where they were then visualized with confocal microscopy (Zeiss LSM 710). Separate slices were immunostained with 10µl of Osteocalcin conjugated Alexa fluor 680, Collagen II conjugated Alexa fluor 488, Rhodamine Phalloidin (actin), and Hoechst 33342 (nuclear stain) and allowed to bind overnight where they were then visualized with confocal microscopy. Confocal z-stacks were acquired for the 9-mm area located between the two perfusion channels in each hydrogel section. The two nuclear markers (Runx2 and Sox9) were used for quantification of cell differentiation fate. Five 1.8-mm regions

were defined in 2D projection images of the z-stacks for quantification of differentiation status as a function of location relative to each channel. The images were thresholded using ImageJ software, and the number of positive cells (Runx2 and Sox9) were counted and normalized to the total cell number (Hoechst) in each region. The actin marker provided visualization of cell morphology.

4.4 Results and Discussion

The process of stem cell differentiation is challenging to model in vitro on a biologically relevant scale with currently available technology. Therefore, we developed a platform in which large, 3D tissue constructs (on the order of centimeters) could be provided with time-varying morphogen gradients over long periods of time (on the order of weeks to months).

Modeling small and large molecule diffusion gradients

After fabricating the bioreactor and hydrogel perfusion system, we sought to develop a predictive model for designing gradients for stem cell differentiation using small and large compounds. To do so, we used RA as a model small biomolecule as its strong Raman signal allows for sensitive, label-free detection with non-destructive imaging in the hydrogel scaffolds[131,132]. In addition to its strong Raman signal, RA is also relevant for modeling diffusion in our platform because it is an important morphogen in biological development (e.g. spatial organization of the neural tube)[44,101]. First, confocal Raman microscopy was used to measure RA concentration in the hydrogel over time in order to calculate a diffusion coefficient. We set up our system such that RA could diffuse into the hydrogel from a reservoir as shown in Fig. 4.3A. Raman measurements collected at a distance of 0.2 cm from the gel/reservoir interface showed increases in the intensity of the RA peak over time[131,132] (Fig. 4.3B). The peak intensity of the RA signal (maximum

intensity between 1590-1595 cm-1) as a function of time was fit using the equation for diffusion in semi-infinite media[128,133], resulting in a diffusion coefficient of 3.4 ± 0.3 x 10-7 cm2/s (Fig. 4.3C). Although the diffusion coefficient of RA in gelatin hydrogels has not been previously reported, this result is in the expected range based on published diffusion coefficients for other molecules tested in a collagen film.[134] Dodson et al. measured diffusion coefficients of 2.4 to 3.0 x 10-6 cm2/s for various retinoids in a solution of CD3OD and D2O (1:1) and 2.3 x 10-6 cm2/s for all-trans-retinoic acid in a bi-phase assay (agarose matrix and a toluene-based fluid)[135]. The difference between the diffusion coefficient measured in our study and that previously reported is likely due to differences in hydrogel density and composition (i.e. 10% gelatin vs. 5% agarose).

The diffusion of RA through the hydrogel was then modeled using COMSOL with the Raman-derived diffusion coefficient applied as an input parameter. A representative concentration gradient after 24 hours is shown in Fig. 4.3D. The resulting values were further validated experimentally by perfusing RA through channels in a gelatin hydrogel for 24 hours and subsequently quantifying the RA concentration at different locations using a microplate reader (Fig. 4.3E). The experimental and model data show good agreement, suggesting the COMSOL model is a good predictor of small molecule diffusion.

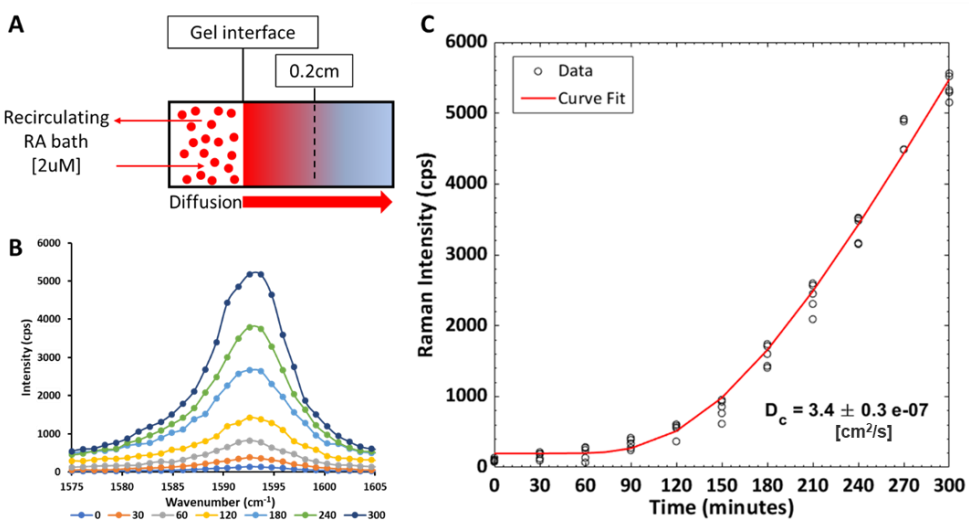

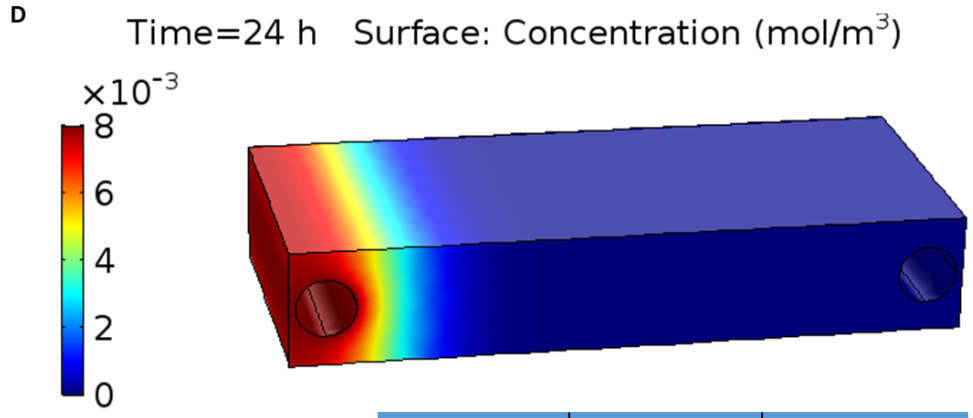

E

	1mm	2mm	3mm
Predicted [RA] mM	2.170	0.331	0.017
Experimental [RA] mM	2.006	0.285	0.018

Figure 4.3: The diffusion coefficient of a model small compound (RA) in the hydrogel scaffold was measured using Raman spectroscopy. (A) A schematic of the experiment shows the reservoir of RA maintained at a concentration of 2 μM adjacent to a hydrogel contained within a PDMS frame. Confocal Raman microscopy measurements were collected at a focal point below the surface of the gel at a location 0.2 cm from the reservoir-gel interface. (B) The intensity of the RA-associated Raman peak (1590-1595cm^{-1}) increased over time as RA diffused into the hydrogel. (C) The maximum intensity of the Raman peak for RA was plotted as a function of time (n=5 independent experiments), and the data were fit with a modified equation developed for the diffusion of semi-infinite media in order to determine the diffusion coefficient of RA. (D) COMSOL model of RA diffusion in a hydrogel with two fluidic channels. Delivery of RA from the left channel is simulated and the RA concentration gradient is shown at 24 hours of perfusion. (E) Values of RA from the COMSOL model were validated experimentally at distances from 1-3 mm.

To model diffusion gradients of larger molecules, hydrogel channels were perfused with 10 kDa dextran conjugated to Texas red and 10 kDa dextran conjugated to FITC. The fluorescence intensity of 10 kDa Texas red dextran in the hydrogel was measured over time at a single location and fit with the diffusion equation (Fig. 4.4A). Fluorescence intensity measurements collected at a distance of 0.2 cm from the channel showed increases in intensity over time, resulting in a calculated diffusion coefficient of 3.6 ± 0.18 x 10-6 cm2/s. This result closely agrees with previously published diffusion coefficients for 10 kDa dextran[136,137]. After 60 minutes of perfusion, opposing gradients of both fluorescent molecules were apparent as shown in an image of the entire length between the red and green channels (Fig. 4.4B) and a plot of the intensity profiles of the two varieties of dextran as a function of distance from the respective channels (Fig. 4.4C). Although the crossover point for the two profiles is dependent on the relative gain settings for each color channel during imaging, the opposing diffusion gradients are clearly present, and the profiles intersect near the center of the hydrogel.

The diffusion of Texas red-conjugated 10 kDa dextran and FITC-conjugated 10 kDa dextran from two parallel channels in a perfused hydrogel was modeled using COMSOL (Fig. 4.4D-E). The simulated diffusion gradients were validated experimentally by perfusing a hydrogel for 60 minutes with the two dextran molecules in isolated channels (Fig. 4.4B) and subsequently quantifying the concentrations of both dextrans at distances of 1 mm, 2 mm, and 4 mm from the right (FITC-perfused) channel (x=8, 7, and 5 mm in COMSOL simulation) with a microplate reader (Fig. 4.4F). The experimental and model data show good agreement, suggesting the COMSOL model is a good predictor of large molecule diffusion.

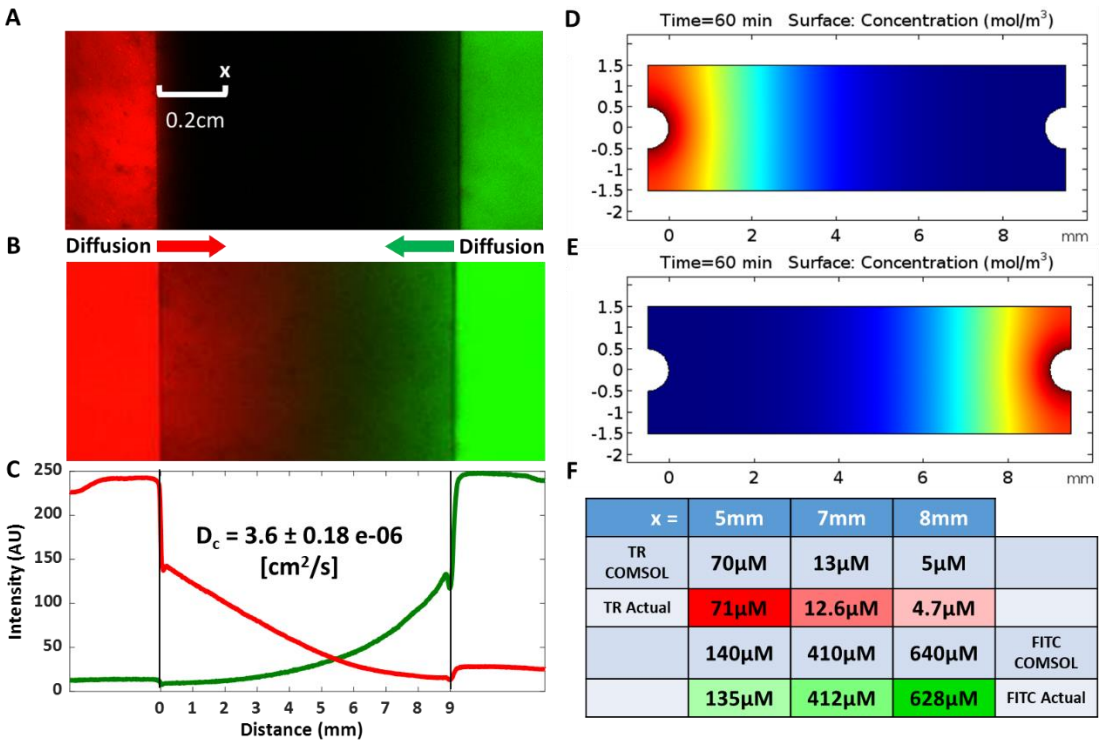

x =	5mm	7mm	8mm	
TR COMSOL	70µM	13µM	5µM	
TR Actual	71µM	12.6µM	4.7µM	
	140µM	410µM	640µM	FITC COMSOL
	135µM	412µM	628µM	FITC Actual

Figure 4.4: The diffusion coefficient of a model large compound (fluorescently-labeled 10 kDa dextran) in the hydrogel scaffold was measured using confocal microscopy. (A) A fluorescent image of the experiment shows the left perfusion channel (red) and the right perfusion channel (green) under perfusion with a syringe pump. Fluorescence intensity of Texas red dextran at a spot 0.2 cm from the left channel was measured over time to determine the diffusion coefficient. (B-C) After 60 minutes of perfusion, opposing gradients of both Texas red- and FITC-dextran molecules were apparent. (D-E) Using the acquired diffusion coefficient, a COMSOL model was created to simulate Texas red dextran diffusion from the left port and FITC dextran diffusion from the right port. (F) Local concentrations of both dextrans obtained from the COMSOL simulation were validated experimentally at positions corresponding to x=5, 7, and 8 mm.

Demonstration of temporal control of morphogen delivery

RFP-expressing fibroblasts were transduced with a lentivirus to report RA signaling via GFP expression. These RA reporter cells were embedded in the dual port perfusion bioreactor for real-time, dynamic visualization of cellular response to the diffusion of RA. The cell-laden hydrogel was imaged with confocal microscopy to visualize constitutively active RFP and the reporter GFP expression after 4 conditions: 1) perfusion of the left channel with 2 µM RA for 1

hour, 2) perfusion of the right channel with 2 µM RA for 1 hour, 3) perfusion of both channels with 2 µM RA for 1 hour, and 4) perfusion with standard media for 24 hours. Standard media was perfused for 24 hours between each RA condition. As shown in Fig. 4.5 A-D, the GFP signal was localized to the region of the gel near the channels(s) perfused with RA. This signal was reversible as shown by conditions 2-4 and that this on/off experiment demonstrates both spatial and temporal control of morphogen delivery to the hydrogel. Because the cells near the center of the hydrogel were not exposed to RA and did not express GFP in this experiment, an additional hydrogel containing RFP-expressing fibroblasts was perfused with standard media for 14 days and stained with Calcein and Sytox blue to confirm cell viability throughout the hydrogel region between the two channels (Fig. 4.5E). This experiment confirmed that 97% of the cells in the region between the two channels were alive at 14 days.

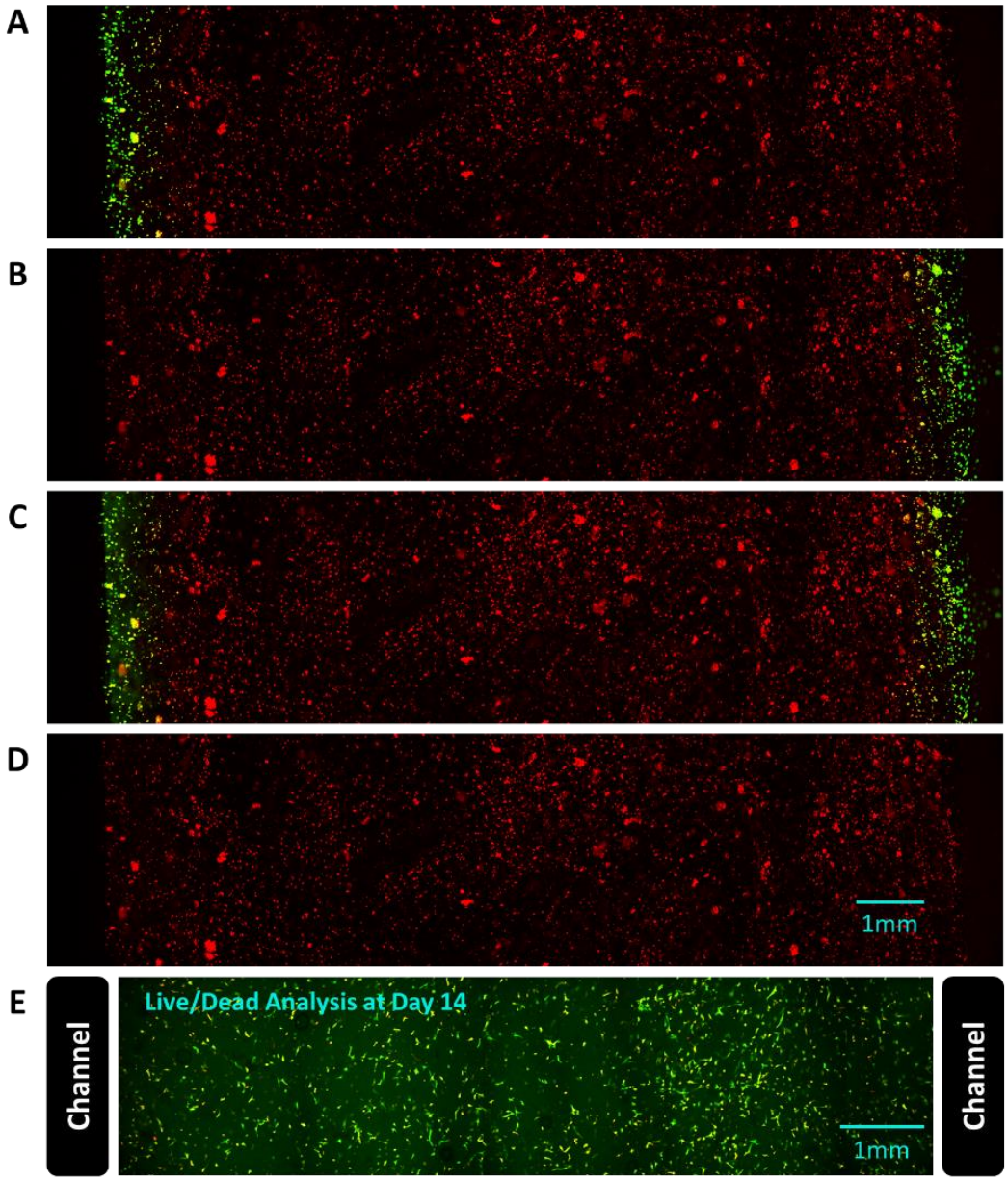

Figure 4.5: Live-cell imaging of the response to RA in RFP-expressing fibroblasts that report RA signaling via GFP expression. The dual perfusion channel, cell-laden hydrogel was imaged to visualize constitutively active RFP and the reporter GFP expression after exposing the device sequentially to the following conditions: (A) perfusion of the left channel with 2 µM RA for 1 hour, (B) perfusion of the right channel with 2 µM RA for 1 hour, (C) perfusion of both channels with 2 µM RA for 1 hour, and (D) perfusion with standard media for 24 hours. Standard media was perfused for 24 hours between each RA condition. The GFP signal was localized to the region of the gel near the channels(s) perfused with RA, and the signal was reversible. (E) To confirm the cells remain viable in the entire region between the perfusion channels, RFP-expressing fibroblasts embedded in a hydrogel perfused with standard media for 14 days were stained with Calcein and Sytox blue (97% live cells).

One difficult aspect of replicating *in vivo* developmental progression is the inability to control and manipulate temporal changes in morphogen concentrations in large 3D scaffolds. Traditionally, stem cell differentiation protocols have been developed and optimized in 2D cultures. This approach focuses on the direct delivery of soluble morphogens to a monolayer of cells, resulting in a large yield of differentiated cells. However, these results are not indicative of the complex stem cell niche that arises when cells react to the endogenous cues of 3D physical environments, including morphogen gradients, cell-to-scaffold, and cell-to-cell interactions. These concerns have prompted the development of systems to better control morphogen delivery in 3D culture. Our device, as demonstrated using the RARE reporter cells, allows researchers to introduce a morphogen such as RA to the cells through diffusion and monitor real-time responses to morphogen exposure. In addition, this platform enables users to turn off the morphogen signal by simply changing the perfusion media.

Spatially tuned control of MSC fate with morphogen gradients

MSCs were uniformly embedded in 3D hydrogels and the two parallel channels were perfused with osteogenic (containing 10ng/ml BMP-2) or chondrogenic (containing 20 ng/ml TGFβ1) media provided by two separate conical tube reservoirs (Fig. 4.2A-B). Stem cell differentiation was characterized using immunofluorescence and Western blot after 35 days of perfusion. High-magnification images of nuclear (Runx2 and Sox9) and extracellular matrix (Osteocalcin and Collagen II) markers of osteogenic and chondrogenic differentiated MSCs confirm that both cell fates were achieved in the hydrogels (Fig. 4.6). Immunofluorescence of Runx2 (a marker of osteocytes) and Sox9 (a marker of chondrocytes) was first used to visualize (Fig. 4.7A) and quantify (Fig. 4.7C-D) MSC differentiation in response to each morphogen. The number of Runx2-positive cells (osteocytes, normalized to total cell count (Fig. 4.7B)) was

maximized within a 3.6 mm distance from the channel (Fig. 4.7C, Regions 1 and 2) and decreased significantly at 3.6-7.2 mm (Regions 3 and 4, $p<0.05$). The region of the gel furthest from the channel (7.2-9 mm, Region 5) had an additional significant reduction in differentiation of MSCs into osteocytes (Fig. 4.7C, $p<0.05$). The Sox9 immunofluorescence showed a steeper gradient (Fig. 4.7D), with a significant decrease in the percentage of positive cells in Regions 3 and 4 relative to Region 5 (1.8-5.4 mm from channel). The differentiation of cells into chondrocytes further decreased significantly at distances 5.4-7.2 mm and 7.2-9 mm from the channel (Fig. 4.7D, $p<0.05$). Protein expression for Runx2 and Sox9 was also confirmed and quantified using Western blot ($p<0.05$, Fig. 4.7E-F) and showed significant decreases in protein expression at each 3 mm increment in distance from the channel perfused with morphogens.

Together, these immunofluorescence and Western blot results confirm that spatial gradients of stem cell differentiation were achieved, resulting in both bone and cartilage regions within a single, 3D hydrogel. The differentiation of MSCs into bone and cartilage using these morphogens has been well-characterized in previous 2D and 3D studies[129,138,139]. Thus, we used these differentiation protocols as a proof-of-concept validation of our stem cell differentiation platform and observed the expected behavior of MSC differentiation. Additionally, we addressed an aspect of in vitro stem cell differentiation that has been underdeveloped: the ability to control morphogen gradients presented to cells for extended periods of time in a 3D construct.

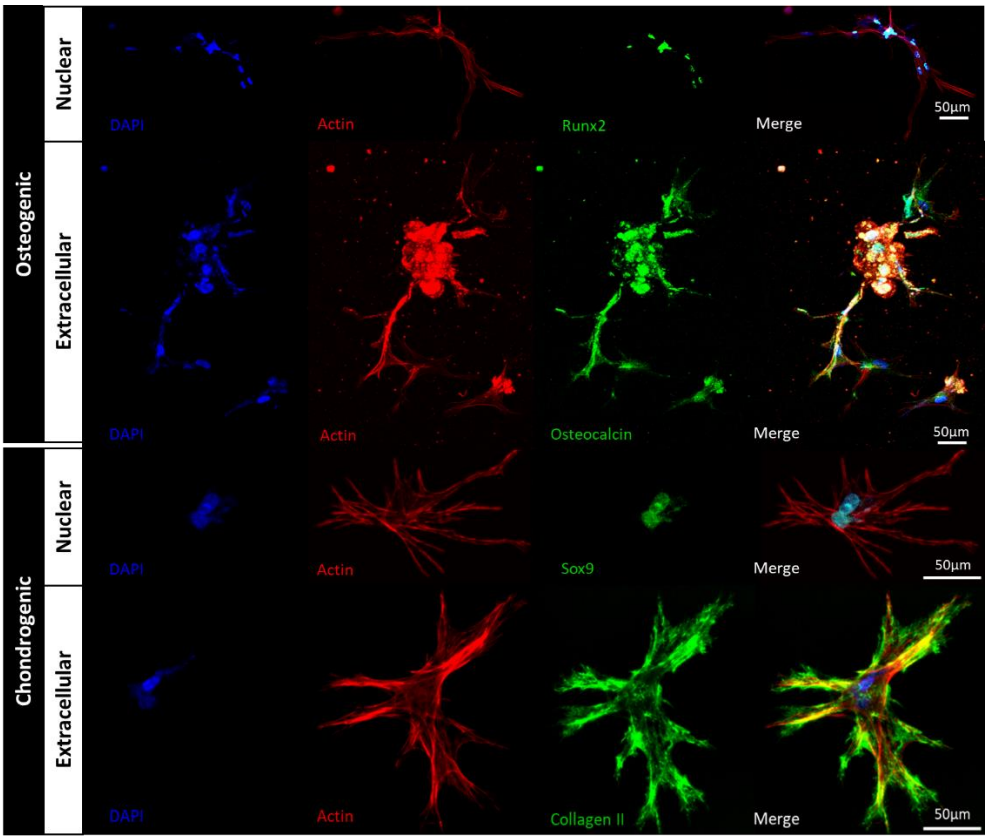

Figure 4.6: Osteogenic and chondrogenic MSC fates were examined using immunofluorescence after 35 days of hydrogel perfusion with differentiation media. Cells in the osteogenic region expressed Runx2 in the nucleus and osteocalcin in the extracellular matrix. Cells in the chondrogenic regions expressed Sox9 in the nucleus and Collagen II in the extracellular matrix. Hoechst and actin stains were used to visualize cell nuclei and cell morphology, respectively.

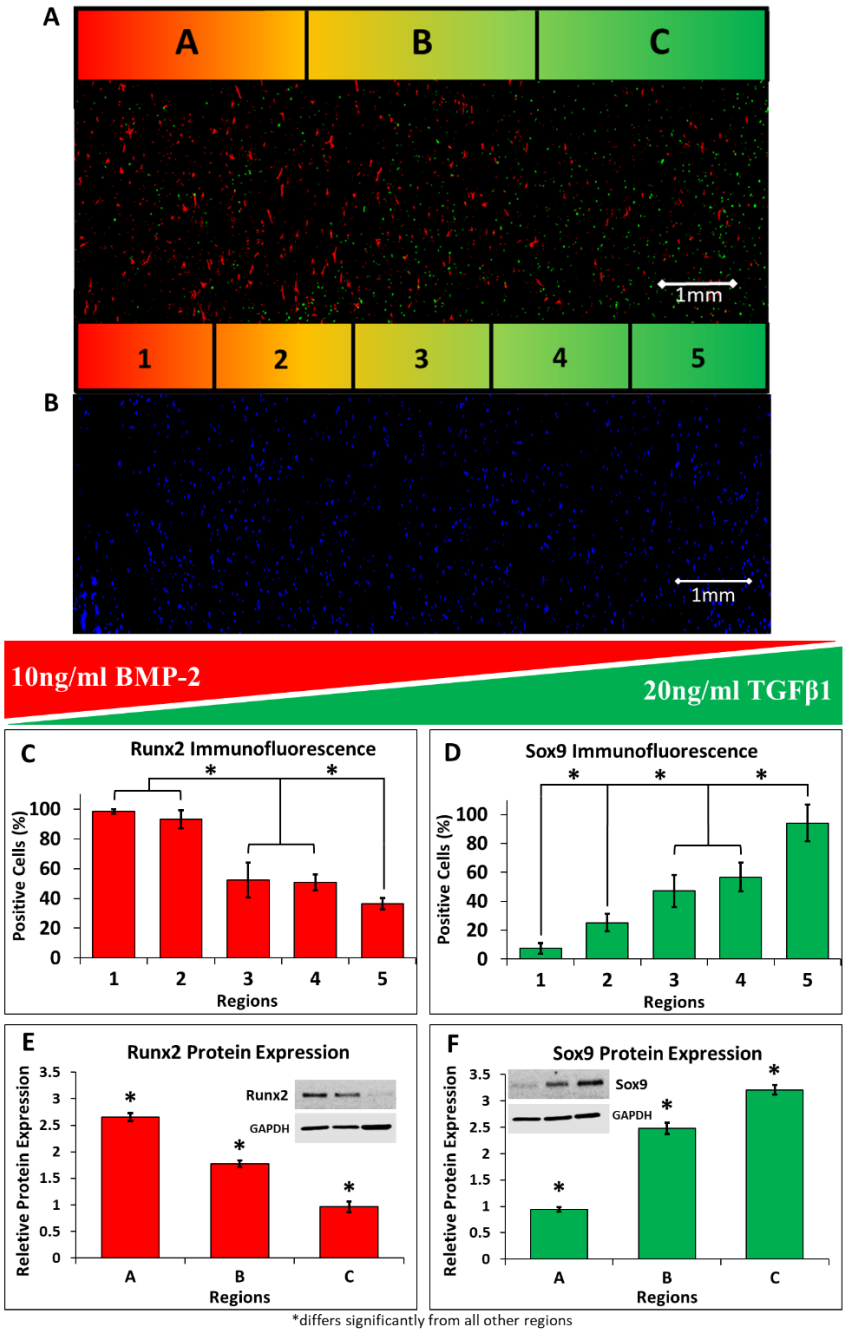

Figure 4.7: Opposing gradients of osteogenic and chondrogenic differentiation can be generated by delivery of soluble morphogens localized to isolated channels. (A) MSCs demonstrated gradient patterns of differentiation with respect to osteogenic and chondrogenic media. This representative immunofluorescence image shows spatially opposing gradients of osteogenic and chondrogenic differentiation of MSCs, with the highest level of Runx2 expression (red, marker of osteogenic cells) located near the osteogenic media channel (region 1) and more prominent Sox9 expression (green, marker of chondrogenic cells) located closer to the chondrogenic media channel (region 5). (B) A Hoechst nuclear counterstain was used to visualize the whole-cell population for

normalization of the Runx2 and Sox9 positive cell counts. (C) Osteogenic differentiation induced by 10 ng/ml BMP-2 had the highest immunofluorescence expression of the differentiation protein Runx2 in region 1 and significantly decreased as distance increased from the source channel (regions 2-5). (D) Similarly, chondrogenic differentiation induced by 20ng/mL of TGFβ1 had the highest immunofluorescence expression of the differentiation protein Sox9 in the region closest to the chondrogenic media channel (region 5) and significantly decreased further away from the source channel (regions 1-4). (C-D) The immunofluorescence results were further validated by protein expression measured by Western blot. The highest expression of Runx2 (E) occurred nearest to the osteogenic media channel (region A), and significantly decreased as distance increased (regions B and C). The highest expression of Sox9 (F) was measured nearest to the chondrogenic media channel (region C), and significantly decreased further away from the source channel (regions A and B). *$p<0.05$, n=10 hydrogels.

Previous microfluidic platforms have been designed for tight control of the spatial presentation of morphogens through simple Fickian diffusion principles[19,101,118,140]. However, these systems often not well suited for long term cell culture due to cellular overgrowth in the small 3D environment. In the current work, we explored the ability to further tune the MSC differentiation gradient over a 35-day period by modulating the morphogen concentration in the chondrogenic differentiation media (10 ng/mL TGFβ1 compared to 20 ng/mL TGFβ1, Fig. 4.8). The lower concentration of TGFβ1 produced a steeper gradient of Sox9 expression as shown by both immunofluorescence (Fig. 4.8A) and Western blot (Fig. 4.8B). While the percentage of positive cells was equivalent for both concentrations of TGFβ1 within the first 1.8 mm region next to the channel as detected with immunofluorescence of Sox9, perfusion with the lower morphogen concentration resulted in significantly fewer differentiated cells within each of the other 4 regions relative to the higher TGFβ1 concentration (†$p<0.001$, Fig. 4.8A). Western blot analysis showed that protein expression differed significantly between the two concentrations of TGFβ1 within all three 3-mm regions (*$p<0.05$, Fig. 4.8B). These results indicate that the spectrum of differentiation states can be further modulated by varying the concentration of a morphogen provided to the hydrogel via the perfusion channel[22,56,119,120]. Because our platform is designed with external

reservoirs that can be replenished or replaced, and perfusion circuits that could employ valves to automatically switch between reservoirs, we have an additional level of control for designing complex morphogen presentation gradients in space and time.

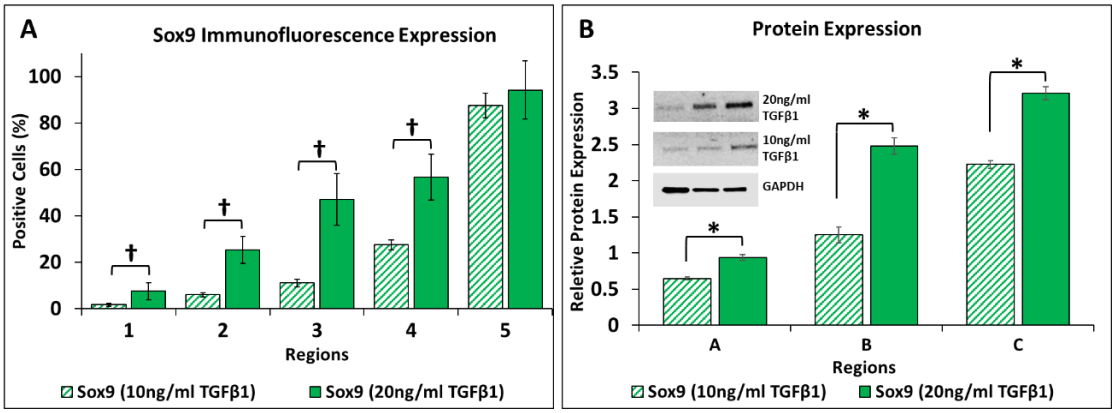

Figure 4.8: MSC differentiation gradients generated by TGFβ1 can be tuned based on source channel concentration. (A) Quantitative analysis of Sox9 immunofluorescence reveals a decrease in the percentage of differentiated cells when the concentration of TGFβ1 is decreased from 20ng/mL (solid bars) is decreased to 10ng/mL (striped bars). Regions 1-4 showed a statistical difference (†$p<0.001$) between the 20ng/mL and 10ng/mL TGFβ1 conditions. (B) Quantitative analysis of protein expression of Sox9 showed a decrease in chondrogenic differentiation with a decrease in TGFβ1 concentration from 20ng/mL (solid bars) to 10ng/mL (striped bars). Regions A-C showed a statistical difference (*$p<0.05$) between the two TGFβ1 conditions. n=10 hydrogels per TGFβ1 concentration.

As stem cell studies increase in complexity, so must the versatility of the platforms needed to perform experiments. Several novel approaches have been developed to study the precise mechanisms by which individual components regulate stem cell differentiation in 3D. For example, vertebral neural development[141], kidney development[142], liver development[143], and cardiac development[144] have been studied using 3D, multicellular masses known as organoids[145] to mimic *in vivo* architectures and complex functions. These structures can grow to millimeters in size over the course of months and exhibit layered differentiation. However, to

achieve proper organization, organoids derived from stem cells require complex, region-specific dynamic cues to differentiate into a multifaceted, functional organoid. One approach to growing more complex organoids is to manually fuse separate, differentiated organoids such as individual brain regions[146]; however, human intervention may impart heterogeneity and fusion of more than two regions remains challenging. Our perfused scaffold-based platform represents an alternative approach for generating large, complex architectures, as it allows for differentiation of stem cells into multiple tissue types within a single, large-scale hydrogel without the need for joining separate constructs. However, our large-scale scaffold still presents finite boundaries to the cells, which is a common limitation for in vitro models of developmental processes, regardless of the size of the construct. An advantage of using a large, 3D hydrogel is the ability to dissect and analyze spatially discrete regions using several common readouts (e.g. immunofluorescence and Western blot) that would be difficult to obtain in microfluidic system. Another limitation in this study is the absence of cellular metabolic activity and consumption of morphogens in the COMSOL model. While simulated diffusion gradients at early timepoints can be validated experimentally, the model does not account for the complex cellular binding and uptake of morphogens which is beyond the scope of the current work. Together with the diffusion model, our hydrogel perfusion platform, with external reservoirs that can be turned on/off or replenished as desired, would allow users to predict and tune spatial and temporal morphogen gradients to achieve control over a targeted range of stem cell lineages/commitments localized to specific regions of a scaffold.

4.5 Acknowledgments

This research was funded and supported by NSF BMAT 1506717 (LMB), NIH R00EB013630 (LMB) and a NARSAD Young Investigator Award from the Brain and Behavior Research Foundation (ESL). EKN was supported through NSF Graduate Research Fellowship DGE-1445197. YCO and RB were supported through CMMI-1634856. DAB was partially by NIH T32GM007347.

CHAPTER 5

DEVELOPMENT OF BIOFUNCTIONALIZED MOLDABLE HYDROGELS TO SUPPORT FORMATION OF NEURONAL NETWORKS

Aim 3.A: Develop a hydrogel system to support formation of a neuronal network that can serve as a platform for studying neurological diseases.

5.1 Abstract

Due to the inability to acquire live human brain tissue, most studies of neurological development and neurodegenerative diseases have been limited to animal models. However, *in vivo* models do not fully mimic the human brain and disease conditions. A biomaterial for promoting neural cell growth and network formation that is rigid enough to support patterning of perfusion channels would be highly advantageous, but to date has yet to be developed. Typical hydrogels used (e.g. hyaluronic acid, Matrigel) support many types of neural cells but lack the ability to be molded and do not promote effective survival of single-cell neuron suspensions through exogenous cues. This study evaluates gelatin methacrylate modified with N-cadherin, a short peptide that promotes synaptic formation and plasticity, ("GelMA-Cad") as a biomaterial solution to this problem.

5.2 Introduction

Neurodegenerative diseases are estimated to affect 1 in 7 people[23]. These disorders (e.g. Alzheimer's disease, Parkinson's disease, Huntington's disease, Amyotrophic Lateral Sclerosis and Multiple Sclerosis) all have different brain region-specific presentation and cell-cell signaling

paradigms, making it difficult to understand the mechanism and propagation of the disease and thus limiting effective treatments. As such, there has been a growing interest in developing *in vitro* models for studying neurodegeneration. This interest has been primarily driven by the lack of clinical translation of prospective therapeutics that were initially deemed promising based on efficacy in animal models [25,66,147–150]. 2D neural cell culture systems have been extensively utilized for initial therapeutic development, while useful, these culture platforms are generally not able to recapitulate appropriate cell morphology, electrophysiological activity, and robust neuronal communication between various cell types[151]. Meanwhile, recent advancements in 3D neural tissue models have generated much excitement due to their prospective ability to mimic the structure and function of human brain regions. It is hoped that such 3D models will lead to an improved understanding of disease biology and serve as platforms for screening of potential therapeutics.

At present, there are many examples of 3D human neural tissue models in the literature, each aiming to create clusters of neurons and other relevant cells (such as astrocytes and oligodendrocytes) to form interconnected neural circuits[29,30,152,153]. These tissue models are often constructed from human induced pluripotent stem cell (iPSC)-derived progenies and typically consist of either organized multicellular structures (e.g. spheroids or organoids) or random assortments of cells embedded in ECM. One common approach is to embed iPSC-derived organoids in Matrigel and culture these structures in spinning flasks or bioreactors[28,154]. The Matrigel ECM supports the self-organization of the neuroepithelium to induce neuroepithelial buds and facilitates growth by providing a structural matrix for cells to attach and grow[26]. These buds further develop into structures that are analogous to the developing human brain and can be used for studying developmental pathways. Additionally, Matrigel has a stiffness that matches the

developing human brain (500 Pa-1kPa)[25], which facilitates neuron survival/maturation[155,156]. Other materials that have been developed for extended culture of iPSC-derived neural progenitor cells (NPCs) and neurons include silk, collagen, hyaluronic acid (HA), elastin-like peptides, and polyethylene glycol (PEG)[25,29,51,157–159]. Scaffolds constructed from these highly-porous materials allow for diffusion of essential nutrients and morphogens throughout the entire construct, which helps avoid mass transfer limitations often seen in larger organoid-based systems. Using these materials to make small 3D constructs has allowed researchers to maintain NPCs and neuronal cultures for extended studies (months), monitor differentiation and behavior such as axon formation, growth, and pruning[30,152,157]. Additionally, these platforms have demonstrated utility for assessing disease phenotypes when the iPSCs are sourced from patients that harbor genetic risk factors for each disorder[29].

Herein, we focused on engineering an ECM material to facilitate neuronal survival and maturation within large, perfusable tissue constructs. This endeavor was motivated by some of the intrinsic downsides of existing ECM platforms mentioned in Chapter 2.3. In terms of tissue structure fabrication, many ECMs such as Matrigel and HA collapse under their own weight (too compliant), and are therefore too soft for molding; as such, these materials are incompatible for incorporating vasculature using top-down fabrication approaches and thereby cannot overcome mass transfer limitations that can result in hypoxia-mediated apoptotic regions in larger structures. In addition, the ECM platforms used for neural tissue constructs are not typically designed to present physical cues (e.g. N-cadherin, RGD motif) that promote cell-cell or cell-ECM interactions to facilitate neuronal maturation. Of the aforementioned materials, only Matrigel (e.g. primarily laminin) and HA have physiological relevance to brain tissue. Indeed, iPSC-derived organoids embedded in Matrigel yield functional neurons[25,30] and iPSC-derived NPCs embedded in HA

rapidly mature into neurons (as compared to NPCs in 2D culture)[158], but the previous issue of the hydrogels being too compliant remains. Additionally, most naturally-derived or synthetic ECM materials are relatively expensive, which can render fabrication of larger structures cost-prohibitive. To overcome some of these challenges, we synthesized a biomaterial termed GelMA-Cad, which consists of gelatin methacrylate (GelMA) conjugated with a peptide from an extracellular epitope of N-cadherin (a proposed graphical representation of cell-to-ECM interaction is represented in Fig. 5.1A). Herein, we demonstrate that GelMA-Cad facilitates neuron survival and extension of neurite processes. We further demonstrate that this novel biomaterial has physiological stiffness and can be used in large hydrogel blocks patterned with perfusable channels that remain patent throughout long-term experiments.

5.3 Methods

Cell Culture

CC3 iPSCs[160] were maintained on Matrigel (VWR) coated plates with E8 medium (produced according to a previously described protocol)[161]. When the cells were about 60-70% confluent, they were passaged using Versene (Thermo Fisher). The iPSCs were differentiated into cortical glutamatergic neurons using a previously described protocol[162] with some modifications. Briefly, CC3 iPSCs were dissociated from the plates using Accutase (Thermo Fisher) and seeded onto Matrigel coated plates at a cell density of 250k/cm2 and then cultured in E8 and 10 μM Y27632 (Tocris). The following day, the iPSCs were given E6 (produced according to a previously described protocol)[161] supplemented with 10 μM SB431542 (Tocris) and 0.4 μM LDN1931189 (Tocris) for 5 days. The media was gradually transitioned from E6 to N2

Medium (DMEM/F12 medium, Thermo Fisher, supplemented with 5 mL of N2 supplement, Gibco) supplemented with 10 μM SB431542 and 0.4 μM LDN193189 over the next 5 days. On the 11th day of the differentiation protocol, the neural precursors were passaged using Accutase and re-plated onto Matrigel in Neural Maintenance Medium at a cell density of 100k/cm2. Neural Maintenance Medium was produced by mixing a 1:1 ratio of N2 Medium and B27 Medium (Neurobasal Medium; Thermo Fisher; 200 mM Glutamax, Gibco, and B27 Supplement, Gibco). Cells were then maintained Neural Maintenance Medium, with a media change every day for the next 20 days and a media change every 3-4 days afterwards. Neurons were used for experiments between days 70-100.

GelMA Synthesis and Characterization

Methacrylated gelatin was synthesized as described previously[163]. Briefly, type A porcine skin gelatin was mixed at 10% (w/v) into phosphate buffered saline (PBS) at 60°C and stirred until fully dissolved. Methacrylic Acid (MA) (Sigma) was added to the gelatin solution at a rate of 0.5 mL/min under stirred conditions at 50°C until the target volume was reached and allowed to react for 1 h. Following a 5X dilution with additional warm (40°C) PBS to stop the reaction, the mixture was dialyzed against distilled water to remove salts and MA using 12–14 kDa cutoff dialysis tubing for 1 week at 40°C. The resulting GelMA solution was lyophilized for 1 week and stored at −80°C.

Peptide Conjugation and Characterization

N-cadherin peptide conjugation was performed as previously reported [164] with slight modifications. Briefly, a 10% GelMA solution was reconstituted in TEOA (triethanolamine) buffer and stirred at 37°C for one hour until fully dissolved. Scrambled (Ac-AGVGDHIGC) or N-cadherin mimic (Ac-HAVDIGGGC) peptides were mixed with the GelMA/TEOA buffer at 1%

w/v solution. The cystine residue at the C-terminal end permitted Michael-type addition reaction with GelMA. All peptides were obtained from GenScript. The reaction was stirred at 37°C overnight for peptide conjugation. Conjugation was verified through 1H NMR for the presence of the amino acid valine (Fig. 5.1B).

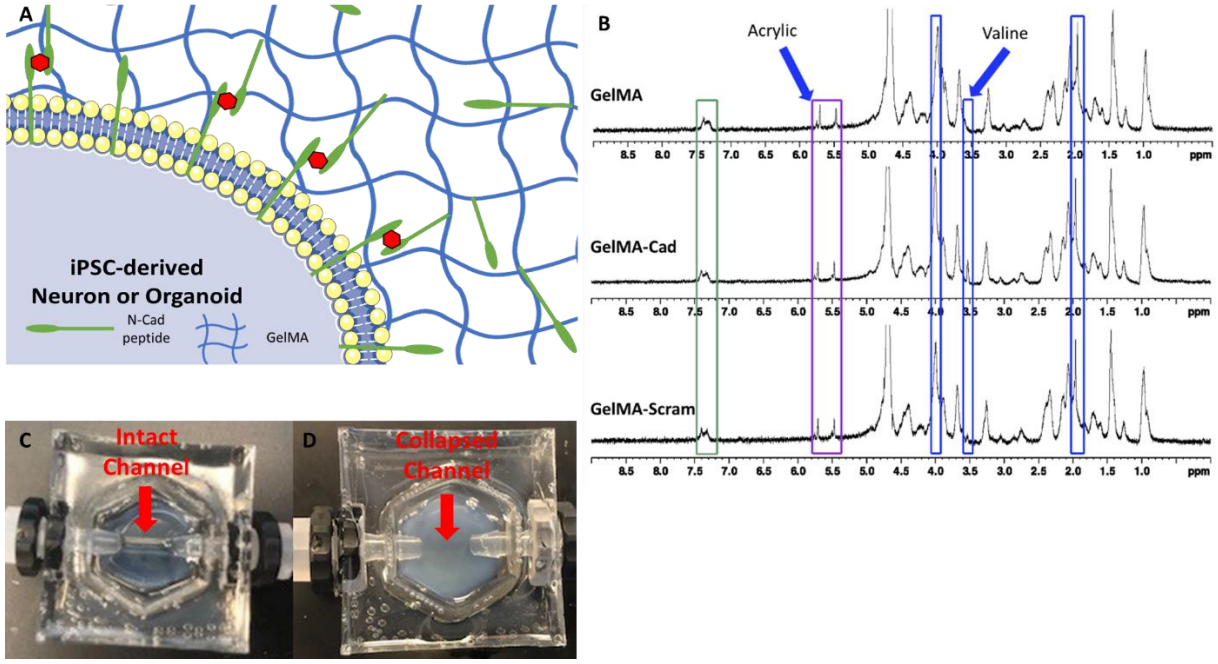

Figure 5.1: A graphical representation of the GelMA-Cad hydrogel and the proposed interaction between the cell and the ECM (A). NMR confirming the conjugation of methacrylated groups to gelatin (GelMA) and the peptide conjugation to GelMA (GelMA-Cad and GelMA-Scram). PDMS mold with crosslinked GelMA-Cad (C) showing an intact channel that can be perfused and Matrigel showing a collapsed channel after crosslinking (D).

Mechanical Properties

GelMA, GelMA-Scrambled (GelMA-Scram) and GelMA-Cad were reconstituted in complete media to make a 10% solution with 0.1% lithium phenyl-2,4,6-trimethylbenzoylphosphinate (LAP) initiator. The solutions were added to PDMS molds (8mm diameter x 8mm height cylinders) and the hydrogels were crosslinked using ultraviolet (UV) light (Thorlabs CS2010) at either 25mW/cm2 or 45mW/cm2 for 10 seconds followed by 30 minutes in

a 37°C incubator. For mechanical testing, each hydrogel was removed from the PDMS mold and placed on the center of the lower anvil of an Instron 5944 mechanical tester, after which the top anvil was brought down to an 8mm distance from the plate. Unidirectional compression was performed at room temperature with a 50N load cell at a rate of 1mm/min to obtain a stress-strain curve and derive the Young's modulus for each hydrogel and UV exposure condition (5 replicates per gel/UV condition). The compression was stopped at 4mm (50% compression) for each trial.

Fabrication of Hydrogels Containing Perfusable Channels

GelMA, GelMA-Scram and GelMA-Cad were reconstituted to a 10% w/v solution and mixed with 0.1% LAP. Once fully dissolved, 1.5 ml of the hydrogel was poured into a mold with a single piece of stiff silicon tubing (1/16" outer diameter) running through the center to form a straight channel. The gels were exposed to 45mW/cm2 for 10 seconds. Matrigel and HA hydrogels were also prepared in similar molds with a straight channel for comparison. After allowing the hydrogels to crosslink, the silicon tubing was removed and the resulting channel was perfused with PBS to check for patency.

Scaffold Seeding

GelMA, GelMA-Scram and GelMA-Cad were reconstituted in complete media to make a 10% solution with 0.1% LAP initiator. iPSC derived neurons that were between 70-100 days old were detached from 6-well plates and spun down in a conical tube. After a cell count, the appropriate volume of cells was added to the reconstituted hydrogel/initiator solution to achieve a 100k/ml cell density. 50µl of the solution was then added to a 48-well plate and exposed to 45mW/cm2 UV light for 10 seconds, then allowed to crosslink in the 37°C incubator for 30 minutes. After the hydrogel crosslinked, media was added to each of the wells.

Confocal Imaging and Analysis

To assess long term cell viability in the 3D hydrogel, the cell-laden hydrogels were exposed to 5% v/v Calcein AM and Sytox Blue for one hour. This staining occurred at 48 hours, 72 hours, and 10 days after embedding. The scaffolds were imaged using a Zeiss 710 confocal microscope and cell viability was assessed using ImageJ.

Raw microscope images were exported in 16-bit TIF format and imported into Matlab 2017 for quantification using a custom image analysis script. Briefly, images were smoothed using a 3x3 pixel smoothing filter to mitigate noise, and in-focus axon segments were identified by isolating regions at least 5% brighter than the mean pixel intensity in the surrounding 50-pixel radius[165]. Cell bodies and axons were distinguished by successive erosion of the resulting binary mass. The erosion radius at which the total cell mass declined most steeply was used to define the radius required to erode axons while sparing cell bodies. Following segmentation of axons and cell bodies, algorithms previously developed for analysis of mitochondrial networks[165] were used to measure the average length and width of each axonal segment.

5.4 Results

Peptide Conjugation

GelMA hydrogels were functionalized with N-cadherin or scrambled peptides, and a control group consisting of only GelMA was used for comparison. Peptide binding efficiency was determined to be 91% ± 0.2 and 90.5 ± 0.2 of the theoretical amount for N-cadherin and scrambled

groups, respectively. NMR confirmed presence of a valine peak at ~3.5ppm in the GelMA-Cad and GelMA-Scram hydrogels (Fig. 5.1B).

GelMA Hydrogels Support Perfusion Channels

Matrigel, HA, GelMA, GelMA-Scram and GelMA-Cad hydrogels were crosslinked in a mold with a single straight channel. After allowing the hydrogels to crosslink, the straight channel template (silicon tubing) was removed and the resulting channel was perfused with PBS (Fig. 5.1C and D). GelMA, GelMA-Scram and GelMA-Cad were all able to be perfused through the channel without rupture of the hydrogel. Matrigel and HA hydrogels could not be perfused, because the channel collapsed immediately after removing the tubing (Fig. 5.1C).

Mechanical Properties

Young's modulus was derived from a stress-strain curve for GelMA, GelMA-Scram and GelMA-Cad hydrogels measured with an Instron mechanical tester. The GelMA samples had an average Young's Modulus of 63 kPa ± 1 when crosslinked with 45mW/cm2 UV light and 40 kPa ± 1 with 25 mW/cm2 UV light (Fig. 5.2). The GelMA-Scram and GelMA-Cad yielded similar results when using 45 mW/cm2.

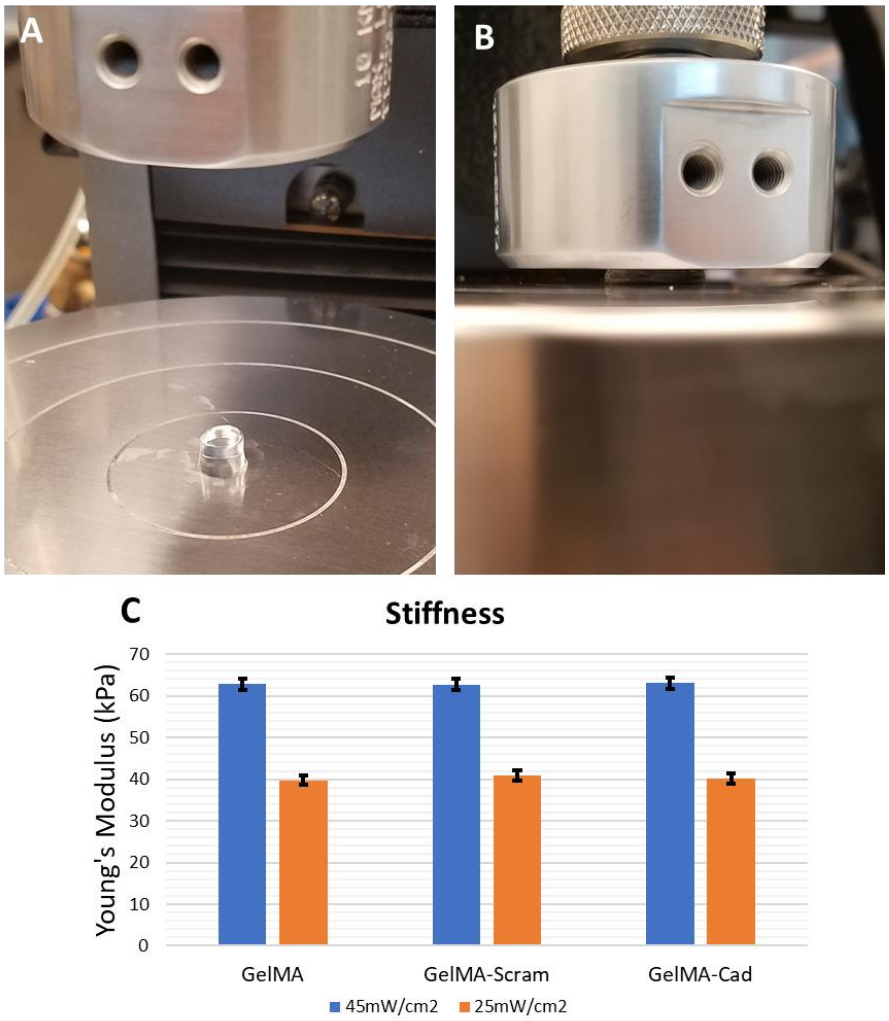

Figure 5.2: Example of GelMA-Cad crosslinked in an 8x8mm column and placed on Instron lower anvil (A). Instron testing showing 4mm compression of the hydrogel (B) and the subsequent Young's Modulus for each of the biomaterials.

N-cadherin Peptide Enhances Cell Viability in 3D Culture

iPSC derived neurons were embedded in 3D GelMA, GelMA-Scram and GelMA-Cad 3D hydrogels crosslinked in a 48 well plate (45mW/cm2 UV intensity for 10 seconds). Long-term cell survival was assessed using confocal imaging of Calcein-AM and Sytox Blue signals at 48 hours, 72 hours, 5 days and 10 days of incubation (Fig. 5.3-5.4). Fig. 5.3A shows iPSC derived neurons stained with Calcein-AM and Sytox Blue located approximately 2 mm deep inside the

gel. Imaging of the GelMA and GelMA-Scram hydrogels showed nearly all cells were dead within 48 hours of embedding (6% ± 2 and 7% ± 3 living, respectively) (Fig. 5.3 A and B). At 48 hours and 72 hours, nearly all of the embedded cells in GelMA-Cad were alive (85% ± 6 and 96% ± 2, respectively) (Fig. 5.3 C and D). On days 5 and 10, the GelMA-Cad hydrogels were again stained with Calcein and Sytox Blue. In GelMA-Cad, cells survived and proliferated within the hydrogel over the 10-day period as shown by a z-stack projection at approximately 2 mm inside the gel (Fig. 5.3C and 5.4). The cells had grown to near confluence by day 10 (Fig. 5.4), however they remained viable with 97% ± 3 living.

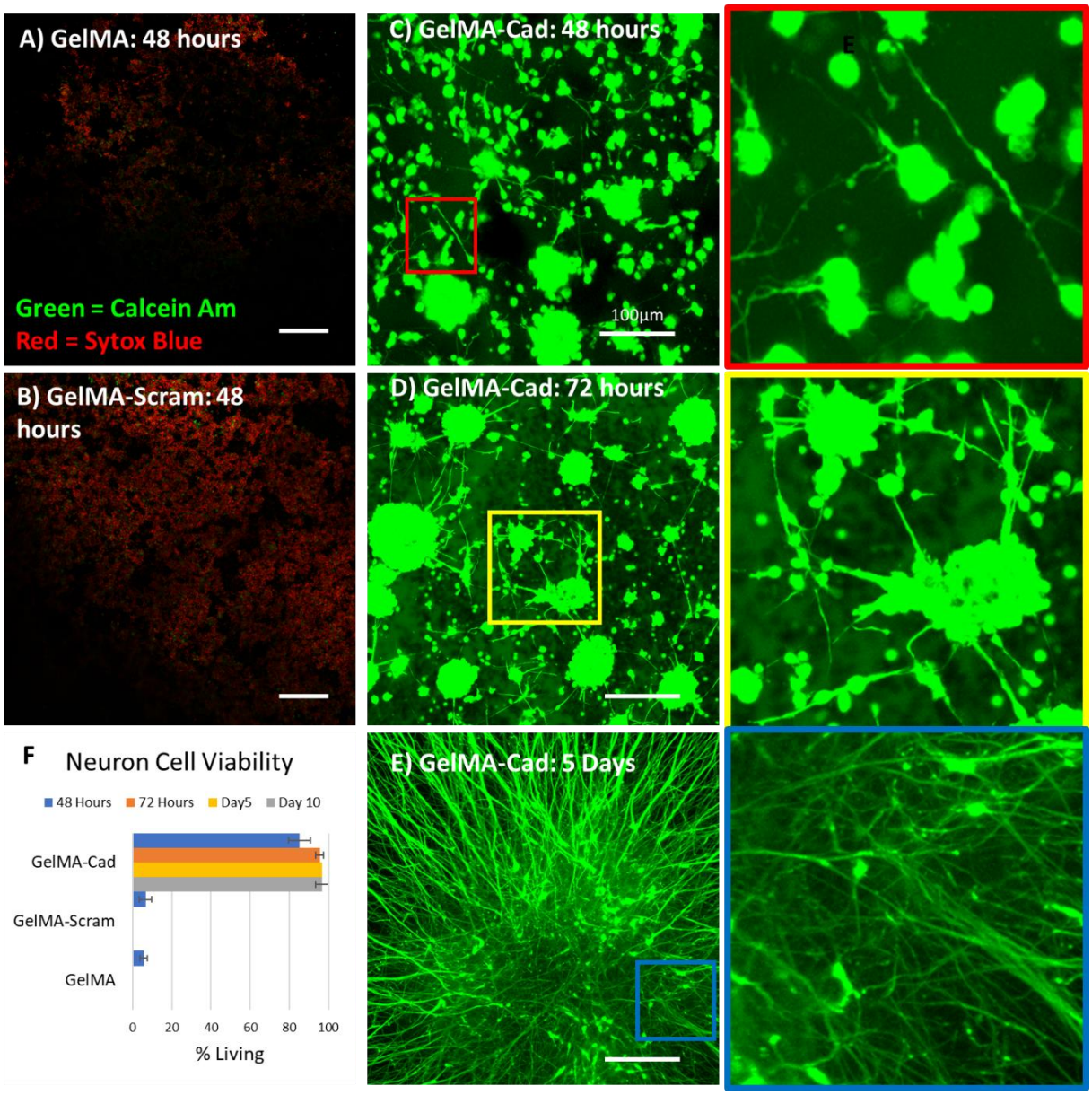

Figure 5.3: Single cells suspensions of neurons survive in GelMA-Cad, but not GelMA or GelMA-Scram after 48 hours. (A) In the GelMA scaffold, only 5.5% of the cells are alive at 48 hours as shown by Calcein/Sytox Blue staining for live/dead cells. (B) Only 6.6% of cells were alive in the GelMA-Scram Scaffold at 48 hours. In the GelMA-Cad scaffold, 85.1%, 95.5%, 96.6%, and 96.7% of cells were alive at 48 hours (C), 72 hours (D), 5 days (E), and 10 days, respectively (F).

Neuronal Network Analysis

For image analysis, confocal z-slice images were individually masked to subtract out the background (Fig. 5.4B and E). The images were then used to identify cell bodies (red) and axon projections (green) (Fig. 5.4C and F)

On day 5 and 10, cells in GelMA-Cad hydrogels were loaded with Calcein for one hour and imaged (Fig. 5.3C and 5.4). Confocal images were then processed in Matlab to determine cell count, average axon width and average axon length. At day 5, the cell body count had an average of 55.6 cells per z-slice and was not uniform over the imaged distance. However, the average axon length was consistent (4.4 μm ± 0.1). At day 10, cell body counts had increased with distance from the bottom surface of the hydrogel with over 250 cell bodies identified in the deepest slice of the z-stack and an average of 162.3 cells per z-slice. The mean axon width (~4-7μm) and length (15μm) were largely consistent across all z-stack slices.

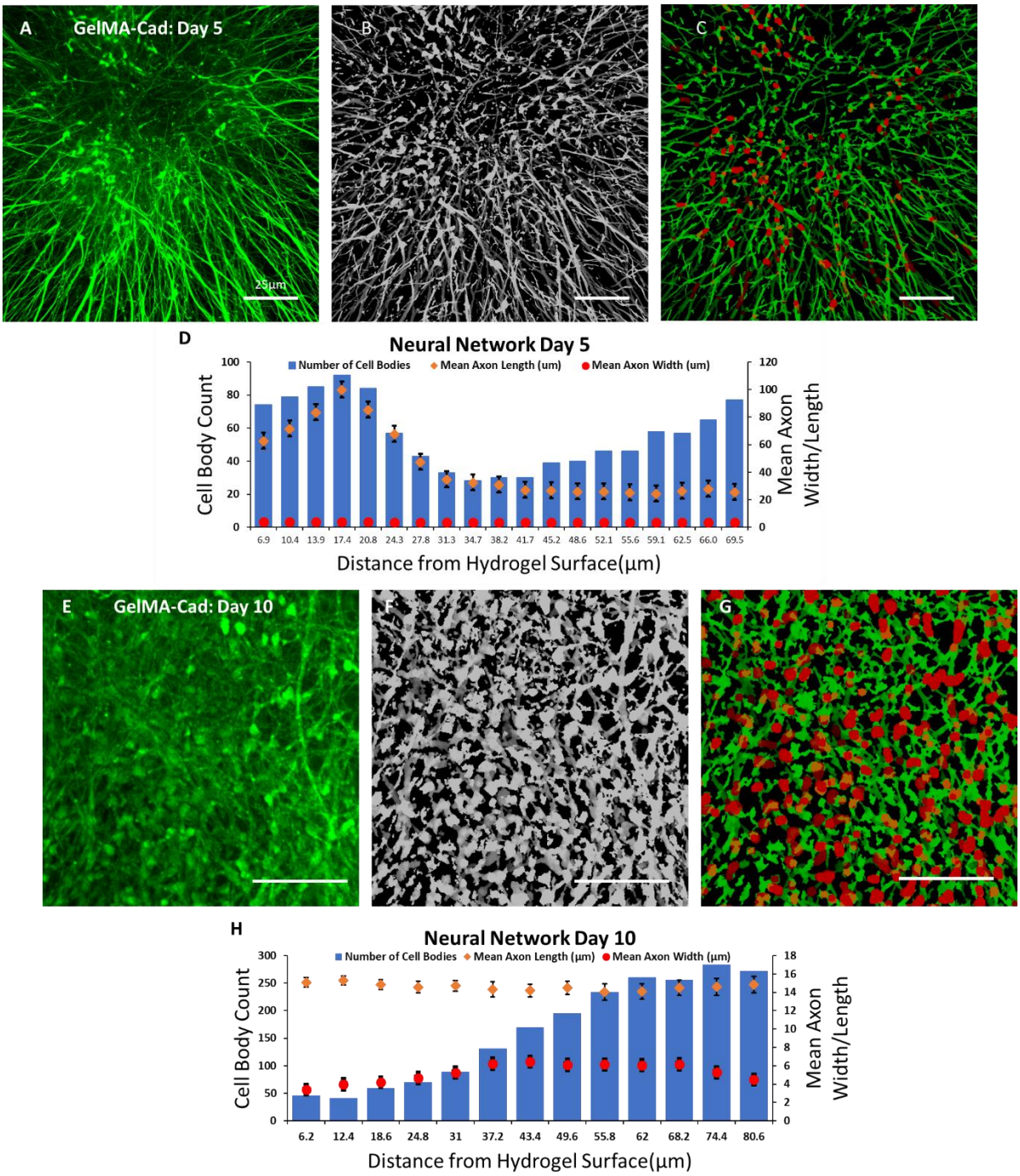

Figure 5.4: Z-stack confocal images of the neuronal networks in the GelMA-Cad scaffold were analyzed to assess cell body count, axon length and axon width. At 5 days (A), cell bodies and axons were identified via masking (B), skeletonizing, and labeling (C) the neuronal network images. (D) The cell body count at 5 days ranged from 30 to 90 per 6.9 µm z-stack slice. The average axon length (per z-slice) ranged from ~25-100 µm and the average axon width was consistent throughout the imaged volume at ~4 µm. At 10 days (E-G), the cell body count increased with distance from the surface up to ~275 cell bodies (H). The average axon width and length across all image slices were 3-6 µm and ~15 µm, respectively.

5.5 Discussion

A 3D model enabling the culture of suspensions of single neural cells and astrocytes would provide a unique advantage for studying disease pathology, progression and propagation at the level of single cells[25,26,30,66,157]. However, efforts towards such studies have been limited due to the lack of materials that can be patterned with embedded perfusable channels while simultaneously providing a soft enough environment to support neuronal cell growth and axon/dendrite formation.

One problem with current hydrogels when used to culture neurons in 3D is the lack of ECM signaling that is present *in vivo* (RGD motif, N-cadherin). There are many factors that contribute to neural cell survival, dendrite growth and synaptic formation in a 3D environment, including neurotrophins, morphogens, and cell adhesion molecules. Some combination of intrinsic programs and extrinsic signals are known to induce development of axons and dendrites. However, these intracellular pathways and extracellular signals are not well understood[151]. Studies employing 2D culture have shown that elevated N-cadherin levels lead to increased dendrite and axon projections[166,167]. The presence of this cell adhesion molecule activates the catenin cascade, which is known to promote axonal outgrowth and suppresses apoptosis. However, these cells must be grown in large 3D spheroids, as neurons that were seeded as individual cells did not project axons and dendrites to neighboring cells in these earlier studies [168]. Another important cell adhesion molecule that has been shown to enhance neural cell behavior is the RGD motif. Recent studies have shown that the presence of RGD domains are neuroprotective and promote neurite outgrowth through integrin activation and integrin-dependent MAPK signaling[169]. Our novel GelMa-Cad hydrogel successfully incorporates a short peptide containing the N-cadherin motif (HAVDI) that has been found to enhance cellular responses in the 3D scaffold [164](Fig. 5.1B).

NMR spectra confirmed the presence of the peptide with a peak from the amino acid Valine at ~3.5ppm. Additionally, this chemical modification did not interfere with the RGD motif that is naturally present in gelatin (peaks at ~4.0 and ~2.0ppm). Thus, it is possible that both of these biochemical signals (N-cadherin and RGD) might simultaneously enhance the integration of iPSC derived neural cells in a 3D scaffold.

To test the theory that N-cadherin and RGD support a single cell neuron suspension, we crosslinked iPSC derived neurons within GelMA, GelMA-Scram and GelMA-Cad hydrogels. 48 hours after formation of cell-laden hydrogels, cells in the GelMA and GelMA-Scram hydrogels were nearly all dead (Fig. 5.3), while the GelMA-Cad cells can be seen growing axons into the 3D matrix (Fig. 5.3). After 72 hours, robust axon projections can be seen interconnecting from cell to cell (Fig. 5.3). And finally, by day 10, the cells in GelMA-Cad hydrogels have formed a high-density network of axons (Fig. 5.4). These results are, to our knowledge, the first demonstration of single neural cells surviving in a 3D hydrogel for an extended time.

Another challenge presented by the use of Matrigel or HA hydrogels is their inability to be patterned with perfusable channels, as they collapse under their own weight[25]. This limits the size of the construct to a radius of ~200μm (the allowable maximum diffusion distance for nutrients from media) and leaves limited room for cell growth before confluence is reached. GelMA, the main component of our hydrogel, has been used in several areas of tissue engineering including cardiac[144], bone[170] and cancer models[171]. The versatility of this hydrogel is due, in part, to the ability to induce free-radical polymerization via UV light. This control makes photopatterning structures in GelMA possible, while retaining a soft environment with mechanical properties similar to brain tissue. The GelMA-Cad hydrogel was reconstituted to 10% solution and exposed to 45 mW/cm2 of 365nm light for 10 seconds in a single channel PDMS mold. This

exposure and subsequent crosslinking formed a gel mechanically robust enough to enable the fabrication of a single straight, perfusable channel in a large hydrogel (Fig. 5.1C), while the Matrigel and HA controls both collapsed and the perfusion channel did not remain patent (Fig. 5.1D). Another advantage of GelMA over existing hydrogel materials is the ability to tune the stiffness of the construct. GelMA hydrogels polymerize as a function of UV light intensity, time and initiator concentration. In the current work, 10% GelMA, GelMA-Scram and GelMA-Cad were polymerized under 45 mW/cm2 or 25 mW/cm2 of UV light for 10 seconds to demonstrate tunable stiffness via measurement of Young's modulus.

GelMA-Cad allows for single cell iPSC derived neural stem cells to be embedded in a 3D matrix for long term culture with minimal cell death and represents a significant advance over prior *in vitro* platforms for neural cell culture. The inclusion of both an N-cadherin short peptide and the RGD motif already present in the gelatin, combined with a soft but moldable 3D matrix, resulted in increased cell survival, increased axon/dendrite projections, and formation of a neuronal network. This platform is expected to enable new studies of neural disease pathology and signal propagation on the single cell level which may lead to more effective therapeutics for a number of neurological diseases.

5.6 Acknowledgments

This research was funded and supported by NSF BMAT 1506717 (LMB), NIH R00EB013630 (LMB) and a NARSAD Young Investigator Award from the Brain and Behavior Research Foundation (ESL). EKN was supported through NSF Graduate Research Fellowship DGE-1445197. YCO and RB were supported through CMMI-1634856. DAB was partially by NIH T32GM007347.

CHAPTER 6

PERFUSED TISSUE CONSTRUCT TO MODEL THE HUMAN DUCTUS ARTERIOSUS FOR RAPID DRUG SCREENING

Aim 3.B: Develop a perfused tissue construct to model the human ductus arteriosus.

6.1 Abstract

Closure of the ductus arteriosus (DA) is a crucial process, necessary to ensure infant viability and health[32]. *In utero,* the DA connects the pulmonary artery and aorta, shunting more than half of the deoxygenated cardiac output away from the developing lungs and into the systemic placental circulation where gas exchange occurs. At birth, the DA must permanently close to facilitate perfusion of the newly inflated lungs. DA closure occurs in two phases: (1) functional occlusion of the lumen via smooth muscle cell contraction, followed by (2) anatomical remodeling of the structure resulting in a permanent fibrous remnant. In normal healthy term infants, functional occlusion of the vessel occurs within the first 12-72 hours of life. However, in some cases, the DA fails to close resulting in a condition termed patent ductus arteriosus (PDA). Several comorbidities including neurodevelopmental impairment, intraventricular hemorrhage and pulmonary hemorrhage have been attributed to or associated with prolonged patency of the DA[34]. Despite a large body of basic science studies using animal models of PDA as well as numerous retrospective clinical analyses, only three drugs are currently available to treat PDA and little progress has been made to establish a standard of care[35]. This lack of therapeutic options and clinical consensus has resulted in substantial heterogeneity in the approach to treating PDA

pharmacologically and/or surgically, and clinical outcomes vary widely. Therefore, this field would benefit significantly from an *in vitro* platform that physically and biologically resembles human DA structure and enables high-throughput screening of novel pharmacology-based therapeutics in an environment closely mimicking that found *in vivo*. To address this need, we have developed and characterized the first (to our knowledge) artificial ductus arteriosus 3D construct using a hydrogel tube with embedded human DA smooth muscle cells.

6.2 Introduction

The ductus arteriosus (DA) is a vascular structure developed in utero that shunts blood from the right ventricle to the descending aorta in order to bypass pulmonary circulation. Upon birth, the DA constricts via the muscular wall and becomes functionally closed after 72 hours[172]. This causes a shift in blood flow, driving blood away from the DA and directly from the right ventricle to the lungs. It is known that this occurrence is associated with an increase in the partial pressure of oxygen that coincides with the first breath. However, in preterm infants this artery is underdeveloped, and closure is delayed by an average of 4 days and remains patent in 10% of preterm infants born at 30-37 weeks of gestation, 80% in those born at 25-28 weeks, and 90% of those born at 24 weeks[173]. After day 7 those rates decline to 2%, 65% and 87%, respectively. Although extensive research has been done *in vivo* and *in situ*, there are few pharmacological therapies that are effective in closing the DA in pre-term infants.

Therapies for closing patent DA (PDA) were developed in the mid-1970s and consisted predominantly of drugs that inhibited cyclooxygenase (COX) enzymes. Indomethacin, a nonsteroidal anti-inflammatory drug (NSAID), was the most commonly used drug for many years, despite the numerous off-target drug interactions (e.g. renal disfunction, intestinal perforation,

altered cerebrovascular regulation, chronic lung disease)[173–175]. More recently, clinical trials have experimented with less aggressive therapeutic strategies for PDA. In such trials, the NSAID drug ibuprofen (COX inhibitor) was shown to be as effective as indomethacin in closing a PDA and cause fewer peripheral side effects on the renal system. Although the use of ibuprofen yields better outcomes compared to indomethacin, it is not ideal given the increased risk of pulmonary hypertension, systemic vasoconstriction, and long-term adverse side effects[176,177]. In the last decade, cardiac catheters have been developed to bridge the gap between invasive surgical intervention and drug treatment[178,179]. These devices are long thin tubes that are placed in a vein or artery, where they are then threaded to the heart in order to occlude the PDA with a biocompatible plug. This technique has been used worldwide and has had some success. However, this procedure requires access to first-world healthcare, has an increased risk of breaking through the blood vessel wall, and can at times lead to undesired dislocation and biodegradation of the implant. Due to the many risks that come with this surgical intervention and existing pharmacological treatments, animal models for testing DA-targeted therapies have been developed for pre-clinical validation of novel drugs.

Animal models of PDA have been widely used and have given invaluable information regarding disease pathology and intracellular pathways[180]. Specific mouse lines have been genetically engineered to have a high prevalence of PDA, making them popular for testing novel drug therapeutics. However, the mouse models have a different intracellular mechanism for PDA (deletion of Myocd gene) compared to humans (mutations in both MYH11 and ACTA2 genes)[76]. For these reasons, current models and tools have not led to significant clinical translation of new therapies. Therefore, a significant need exists for a new platform to be developed for high-throughput screening of novel drug candidates for treating PDA.

Herein, we focused on engineering a human ductus arteriosus (hDA) smooth muscle cell-laden, perfusable artificial artery construct. This engineered artery was perfused in a custom bioreactor for extended time periods. The construct was characterized to determine cellular alignment with respect to fluid flow through the lumen, protein expression, and matrix mechanical properties. Many of the current treatments for PDA are not ideal due to the numerous side effects. Therefore, the development of a human-based *in vitro* system that enables high-throughput screening of novel pharmacological therapies in an environment that closely mimics properties found *in vivo* would be of great benefit.

6.3 Methods

Cell culture

The human DA (hDA) smooth muscle cells were a kind gift from Dr. Elaine Shelton and Dr. Jeff Reese. The cells were maintained in a humidified 5% CO2-containing atmosphere (37°C). Culture medium consisted of DMEM supplemented with 10% v/v fetal bovine serum (FBS), 50 U/mL penicillin and 50 µg/mL streptomycin, all procured from Life Technologies (Carlsbad, CA).

Bioreactor system fabrication

To facilitate the perfusion of the artery construct, a round plastic container made of polystyrene was used (Ted Pella). A 1/4" hole was drilled through the wall of the plastic container using a plastic cutting drill bit (McMaster-Carr, 27465A84, specialized drill bit designed to avoid cracking plastic). A 1/16" barbed female Luer bulkhead was threaded with a gasket and mounted to the drilled hole using locking nuts (Cole Parmer). Soft silicon tubing (1/16" OD, Cole Parmer, 1/2" in length) was then placed over the barb in the chamber. The open end of the soft silicon

tubing was then fitted with a piece of 1/16” stiff silicon tubing; this tubing was used to mount the artificial artery and prevent the construct from disconnecting from the perfusion system. Autoclaved Tygon lab tubing (E-3603, 1/16 in. ID × 1/8 in. OD) (Cole Palmer, Vernon Hills, IL) was washed 3 times with DI water and connected to the Luer bulkheads, and the bioreactor was perfused using a peristaltic pump[126].

Hydrogel scaffold fabrication and perfusion

To create an artificial artery construct, a ¼” ID silicon tube was used to form a mold for the outer wall and a 3/32” OD stiff silicon tubing was used to form the inner channel to serve as the vessel lumen and perfusion channel (Fig. 6.1). Female Luer bulkheads with end caps were used on each end of the tubing to contain the gelatin scaffold for crosslinking. Cells were resuspended in a 10% gelatin solution at a concentration of 10 million cells/mL. Then, 20% microbial transglutaminase (mTG) was added to the solution to make a 9:1 ratio of gelatin to mTG. The gelatin, mTG and cells were immediately poured in between the 3/32” tube and the ¼” tube, the Luer was positioned on the end to prevent leaking, and the entire construct was placed in a 37°C incubator to allow for crosslinking. After 30 minutes, the construct was removed from the tubing, attached to the perfusion system and perfused at 100 µL/min for 7 days (Fig. 6.1B). The media was refreshed every 3 days.

Cell viability

To assess long term cell viability in the gelatin hydrogels supported by the perfusion platform, cell-laden hydrogels were continuously perfused at 100 µl/min for 7 days (“flow” group), while control cell-laden gels (with identical geometry) were not perfused (“no-flow” group). On the last day of culture, all hydrogels were perfused with 5% v/v Calcein-AM and Sytox Blue for one hour (Thermo Fisher, Waltham, MA). Intracellular signals from Calcein and Sytox blue in the

flow and no-flow constructs were imaged on a Zeiss 710 confocal microscope (Zeiss Microscopy, Munich, Germany). Cell viability was assessed using ImageJ (National Institute of Health, Bethesda, MD).

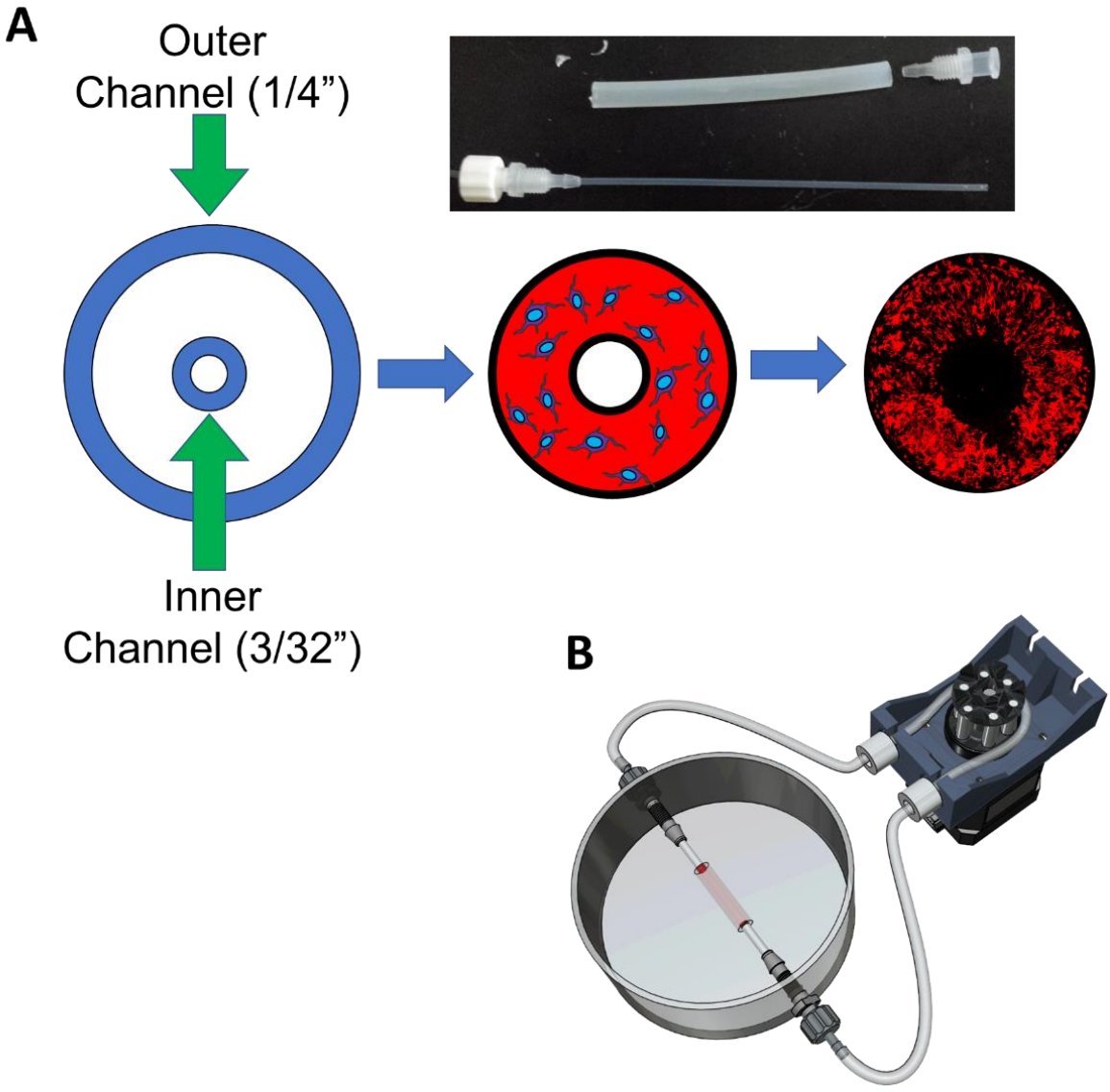

Figure 6.1: Artificial artery construct. (A) ¼" inner diameter tubing was used to serve as the outer wall and 3/32" inner diameter tubing was used to create the inner channel. Human ductus arteriosus cells were mixed into 10% gelatin and crosslinked in the tubing. (B) After the hydrogel was

sufficiently crosslinked, the construct was then perfused in a custom bioreactor consisting of a stepper motor.

Artificial ductus arteriosus characterization

For immunofluorescence characterization, perfused hydrogels were fixed in 4% PFA after 7 days of perfusion. The fixed hydrogels were then washed three times with PBS and then placed in a 5% goat serum blocking solution on a rocker overnight. The hydrogels were immunostained for nuclear, α-smooth muscle actin conjugate Cy3 (αSMA, ThermoFisher), ZO-2 conjugated Alexa Fluor 568 (ThermoFisher). Constructs were imaged on a Zeiss 710 confocal microscope.

For Western blot analysis, the hydrogel was cut into several small pieces and dissolved in Collagenase Type IV (2% W/V) for 1 hour. The resulting dissolved gel-cell mixture was centrifuged at 400*g to pellet the cells. The pellet was washed 3 times with DPBS (without magnesium or calcium) with centrifugation. The pellet was then resuspended in RIPA buffer (Sigma Aldrich) with 1:100 v/v protease and phosphatase inhibitors (Sigma Aldrich) for 5-10 minutes on ice followed by centrifugation at 12,000*g for 15 minutes at 4C. The supernatant was then removed and frozen at -20 °C for future use.

Protein concentrations were determined using the Pierce BCA Protein Assay Kit (ThermoFisher). 10 μg of protein was extracted, and the appropriate amount of RIPA buffer, Laemmli buffer (BioRAD), and betamercapto ethanol (Sigma Aldrich) were added to yield a total volume of 25 μl. These samples were boiled at 95°C for 5 minutes, then cooled on ice. 4-20% Criterion TGX Precast Midi Protein Gels (BioRAD) were pre-run at 70V for 20 minutes in running buffer during this boiling and cooling period. Boiled protein samples and appropriate loading ladder were added to the gel and was then run at 80V until the protein samples had run down the majority of the gels. Gels were then transferred to nitrocellulose membranes on an iBlot 2 dry

blotting system (ThermoFisher) according to the manufacturer's protocol. The membrane was blocked with TBS-based Odyssey blocking buffer (Li-COR Biosciences) for 30 minutes at room temperature on a shaker plate. Primary antibodies were dissolved in the Odyssey blocking buffer with 0.05% Tween 20 (Sigma Aldrich) at the following concentrations: ZO-2 (1:1000, ThermoFisher), Collagen IV (1:1000, ThermoFisher), α-SMA (1:1000, ThermoFisher). Primary antibody incubation was performed at 4C overnight on a shaker plate. Membranes were then washed with TBS containing 0.05% Tween 20 (3 washes for 5 minutes each on a shaker plate). Appropriate Li-COR 800CW secondary antibodies were diluted in TBST at 1:15,000, and then incubated on the membranes for 2 hours at room temperature on a shaker plate. Membranes were again washed with TBST (3 washes for 5 minutes each on a shaker plate) before being imaged on a Li-COR Odyssey scanner, and image processing was performed in the manufacturer's software.

Mechanical testing

The perfused (flow), nonperfused (no-flow), and blank control (no cells) constructs were fitted with 1/16" stiff silicon tubing on both openings of the constructs. The silicon tubing was then super-glued (Loctite ULTRA Control Gel) to the hydrogel and allowed to cure for 5 minutes in a 37°C incubator. Unconfined tensile tests were conducted by using an Instron 5944 materials testing system (Instron Corporation, Norwood, MA) fitted with a 50 N load cell (Fig. 6.5). Specimen diameter and thickness were measured. A 10 mN preload was applied before each test, and each test was performed at a rate of 1mm/minute. The Young's modulus was subsequently extracted from the resulting stress-strain data using the Bluehill software.

6.4 Results

Long-term cell survival

hDA SMCs were embedded in 3D hydrogel scaffolds and perfused continuously through a central channel in the construct (the artery "lumen"). Calcein-AM and Sytox Blue were used to quantify cell viability ([Calcein-AM count] / [Calcein-AM + Sytox Blue count]) on days 1 and 7 (Fig. 6.2A). On Day 1, 91.0% of cells in the perfused constructs were living and 54.9% of cells were living in the nonperfused constructs. On day 7, 96.4% of the embedded cells were alive in the perfused hydrogel and 50.9% were alive in the nonperfused hydrogel (Fig. 6.2A).

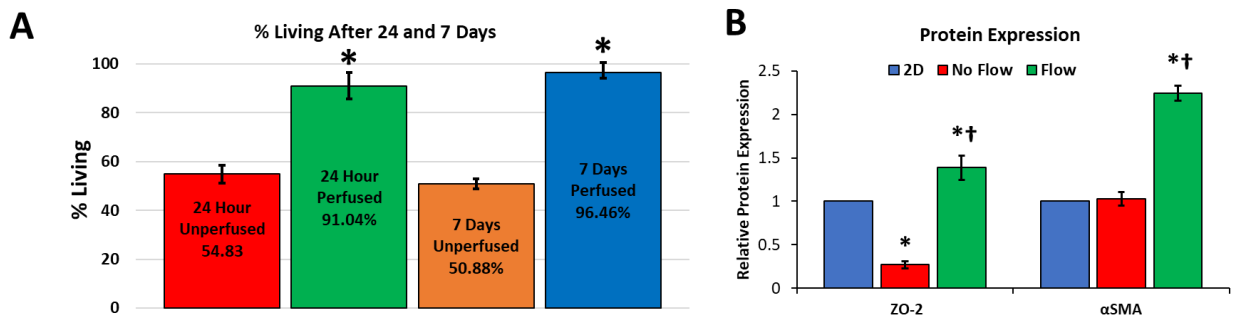

Figure 6.2: hDA cells in the perfused 3D constructs were more integrated than the 3D nonperfused constructs. (A) Cell viability at 24 hours and 7 days in the perfused artificial artery were significantly higher than the 3D nonperfused construct. (B) ZO-2 and αSMC were significantly higher expressed than in the 3D nonperfused and 2D control experiment.

Protein expression

The features of this perfused hydrogel were further characterized by quantification of protein expression via Western blot. The data obtained from the perfused hydrogel showed significant increases in protein expression in the case of the 3D construct under flow conditions relative to 2D hDA cell culture and no-flow 3D construct conditions for all proteins assessed (Fig. 6.2B, ANOVA $p<0.01$, post-hoc Tukey test). Protein expression in the 3D, no-flow condition was

significantly lower than the 2D condition for ZO-2 and Collagen IV (ANOVA $p<0.01$, post-hoc Tukey test). ZO-2 is indicative of cell-to-cell contact and high levels of αSMA confirms the cells maintain their phenotype in the 3D construct.

Cellular alignment

In Fig. 6.3, 3D confocal imaging of the inner lumen of the perfused hydrogel showed that the cells grew radially around the hydrogel and perpendicular to the direction of flow. Fig. 6.3 provides a higher magnification image of this inner lumen and alignment. Using the plugin Orientationj in Imagej, directionality of cell alignment was quantified. On day 4 of perfusion, the hDA SMCs had a 65% (±0.3) perpendicular orientation between the angles of -5 to 5° (Fig. 6.3 A and B). In the nonperfused constructs, orientation perpendicular between angles -5 to 5° was at 16% (±0.3) (Fig. 6.3 C and D). After 7 days of perfusion, the hDA cells had a 97% (±0.2) perpendicular orientation between angles -5 to 5° of perpendicular to the flow (Fig. 6.4 E and F). In the nonperfused constructs, orientation perpendicular to flow was at 18% (±0.3) alignment between the angles 0-5° (Fig. 6.4 G and H).

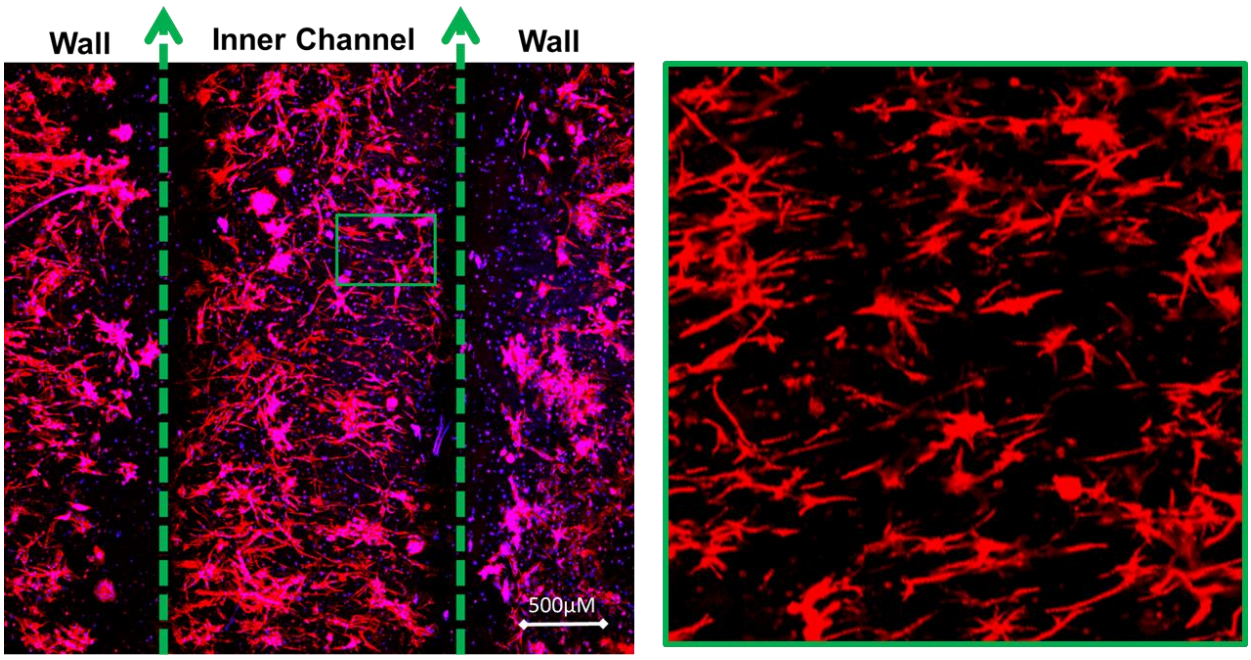

Figure 6.3: Immunofluorescence image of α-smooth muscle actin (αSMA) expression in a cell-laden hydrogel perfused for 4 days. (A) Confocal imaging of a cross-sectional cut of the artificial artery stained against αSMA and DAPI. (B) Higher magnification view of the cells in the inner wall of the artificial artery

Mechanical testing for hydrogel stiffness

Young's modulus was obtained for each 3D construct condition (flow, no-flow, and blank) using tensile testing. The perfused construct had an average of 3.0 kPa (±0.2, n=5) and was significantly less stiff than the nonperfused construct (6.3 kPa ± 0.1, n=5, ANOVA $p<0.05$). The blank hydrogel's stiffness was significantly higher than both the perfused and nonperfused constructs (7.8 ± 0.3 kPa, n=5 ANOVA $p<0.05$).

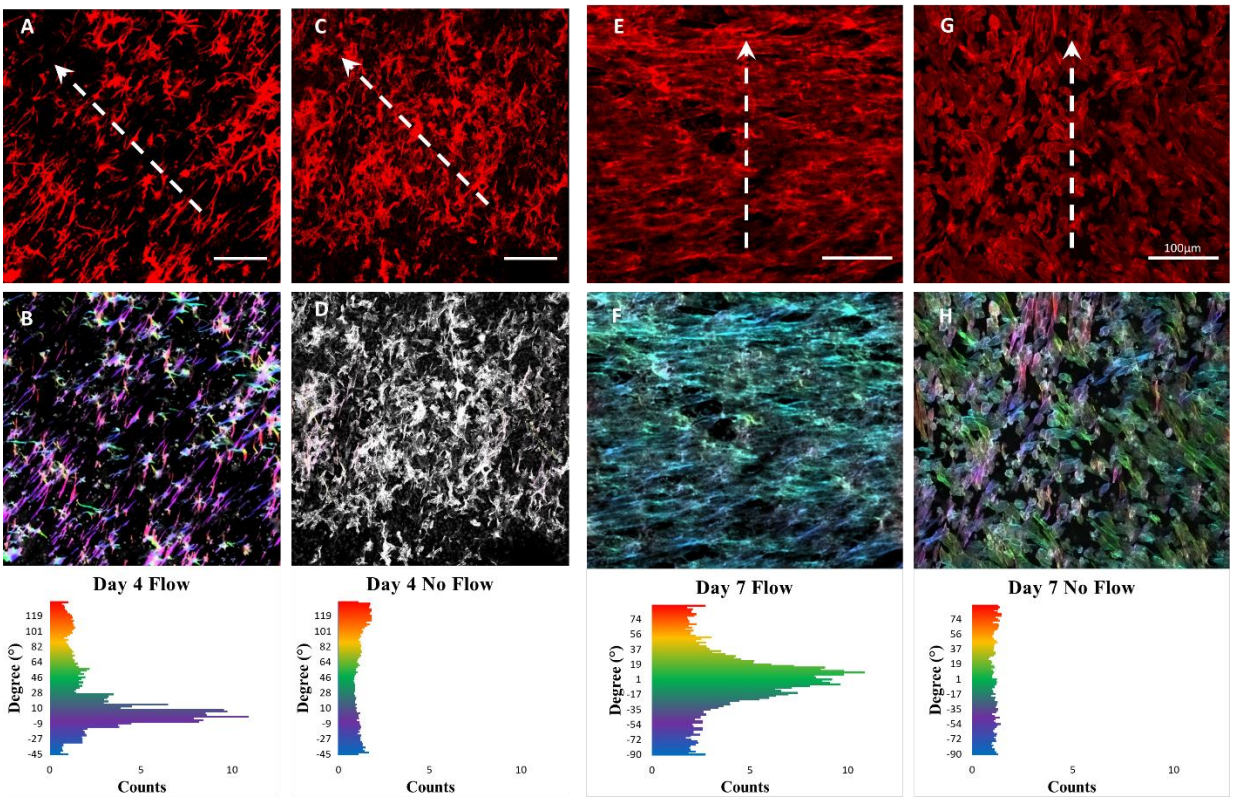

Figure 6.4: 3D constructs under pulsatile perfusion align perpendicular to the direction of flow, similar to the *in vivo* system. (A-B) Day 4 perfused constructs were stained for αSMA for quantification of directionality of the cells. (C-D) The 4 day no flow was stained for αSMC and quantified, however the cells did not have an orientation. Day 7 perfused constructs showed a high degree of alignment (E-F), while the no flow condition was randomly oriented and more round in shape.

6.5 Discussion

Despite the high morbidity rate associated with persistent PDA, there has been relatively little progress in novel therapeutic approaches to inducing DA closure[177]. This lack of progress has driven the need for new technologies for high-throughput screening of potential therapeutics. In the present study, a bioreactor was developed for perfusing the central channel of a hDA SMC-laden tubular hydrogel. To the best of our knowledge, this is the first artificial construct for modeling the human ductus arteriosus.

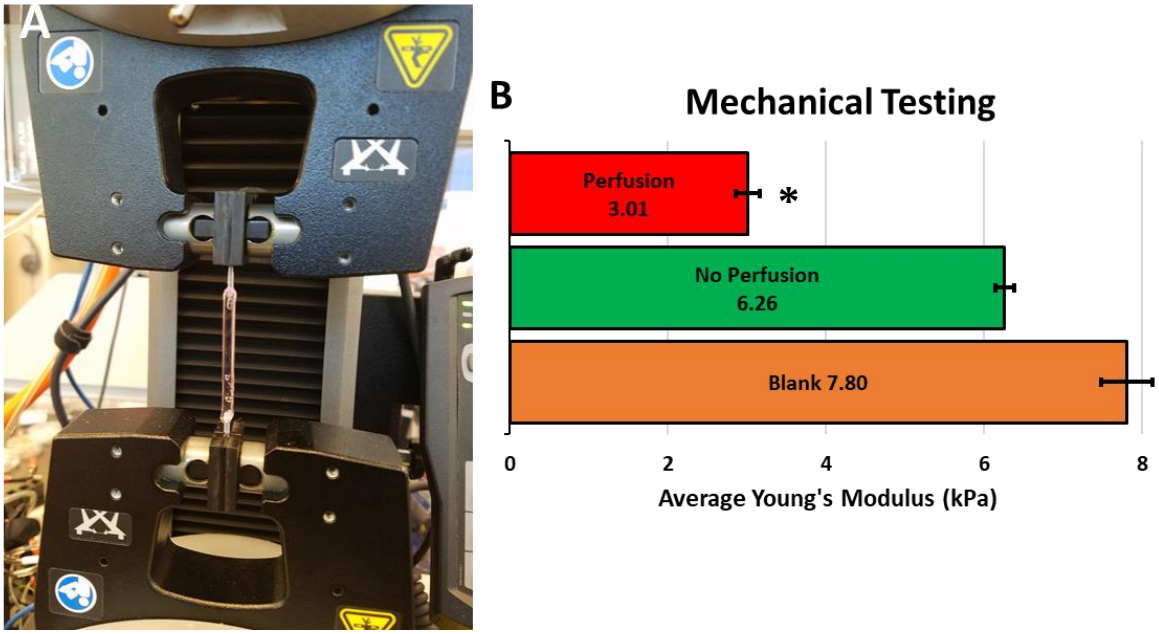

Figure 6.5: Mechanical testing of the perfused cell laden hydrogel was softer than the no perfusion and the blank hydrogel. (A) Representative image of the tensile test between the two Instron grips for the hDA perfusion channels. (B) Perfused constructs were significantly weaker than the nonperfused channels and black controls.

There are multiple protocols for generating SMC-laden 3D constructs for perfusion studies. For example, decellularized donor tissue has been used to enzymatically decellularize the artery, then repopulate the construct with new cells. Another example is the use of monolayer sheets of cells rolled into a tubular shape to create a perfusable construct [33,79,181]. While each of these studies have been proven to be effective at integrating vascular cells, human ductus arteriosus cells have never been introduced into a 3D perfusable construct. In our system, we successfully engineered an artificial artery construct that could be imaged for cell growth and integration of human cells in the system over time frames relevant to the time scale for healthy DA closure in infants. hDA SMCs were embedded into a tubular hydrogel system and perfused using a peristaltic pump. After 24 hours of perfusion, most of the cells embedded in the perfused construct had survived in the hydrogel (91.0%), while the nonperfused constructs only had 54.8% cells living.

On the 7th day, 96.5% of the embedded cells in the perfused construct were alive and the nonperfused had 50.9% living (Fig. 6.2 A). Another marker for healthy SMCs is the expression of ZO-2 and αSMC[182]. It is known that in arterial cells upregulation of ZO-2 and αSMC (a tight-junction marker and structural protein, respectively) are increased when cells are proliferating. In our experiments, the cells in the 2D culture and nonperfused constructs expressed significantly lower ZO-2 and αSMC compared to the perfused constructs (Fig. 6.2 B). These results, in conjunction with the day 7 live/dead staining, show that the perfused constructs were overall healthier. Moreover, in perfused constructs but not in nonperfused constructs, hDA SMCs align perpendicular to the direction of perfusion.

Imaging on day 4 revealed alignment perpendicular to the direction of flow in the perfused constructs (Fig. 6.4 A-B), while the no flow control did not seem to align in any particular direction (Fig. 6.4 C-D). This was quantitatively confirmed using ImageJ. In the perfused constructs 65% of the cells were aligned perpendicular to the direction of flow (between -5 to 5°; 0° being perfectly perpendicular) while the nonperfused constructs were randomly oriented or circular in shape. On day 7, in the perfused construct there was near complete confluence of cells and nearly all the cells were aligned perpendicular between the angles of -5 to 5° (Fig. 6.4 E-F). However, the nonperfused constructs were not nearly as confluent, and cells exhibited no preferred alignment (Fig. 6.4 G-H). There are several factors that may be contributing to cell survival and perpendicular alignment under perfusion. It is known that SMCs are mechano-sensitive and respond to extracellular stimuli, one of which is pulsatile flow[183–186]. This flow is sensed as cyclical stretching and relaxing due to the pulsatile effects on the matrix. In normal physiology, flowing blood is a pulsatile process that causes smooth muscle cell to display a contractile phenotype. It has been shown that smooth muscle cells respond by aligning circumferentially in tubular scaffolds[187,188]. This alignment

allows for the SMCs to constrict/dilate when necessary. In a constant flow environment (without pulsatile perfusion), SMCs change phenotype to become synthetic SMCs; this is a component of atherosclerosis or arterial wall hardening [189]. In this study a peristaltic pump is used to create pulsed waves while pumping. Thus, the high degree of alignment in the perfused compared to the nonperfused is most likely due to the mechanical stimulation from the peristaltic pumping[79].

6.6 Acknowledgments

This research was funded and supported by NSF BMAT 1506717 (Leon M. Bellan), NIH R00EB013630 (Leon M. Bellan) and NIH KL2TR002245 (Elaine Shelton). Haley Antoine was supported by the Vanderbilt University School of Engineering Summer Research Program.

CHAPTER 7

SYNOPSIS AND FUTURE DIRECTIONS

7.1 Summary

In Aim 1, an inexpensive perfusion system was developed to meet the unique demands of perfusing 3D tissue constructs that are much more physiologically relevant than monolayer cell culture. The perfusion system provides a reliable pumping platform that can be programmed to schedule and run multiple motors at various speeds and enables scalable perfusion of large, 3D constructs. Importantly, we demonstrated the ability to perfuse multiple, separate channels inside cell-laden hydrogel slabs, and cell viability was sustained over several weeks. Additionally, using this perfusion system we were able to create and validate a computational model for spatially and temporally varying delivery of soluble factors to cells in a 3D hydrogel scaffold via the embedded perfusion channels.

In Aim 2, the effect of creating opposing gradients of morphogens to induce a spectrum of differentiation of MSCs in a 3D hydrogel scaffold was investigated. Using the pump perfusion system and two isolated parallel channels, BMP-2 and TGFβ1 were used to create a spectrum of differentiation into osteocytes and chondrocytes, respectively. Additionally, we demonstrated spatial control over the gradient of differentiation by varying the concentration of TGFβ1 delivered via perfusion channels.

Finally, Aim 3 demonstrated the versatility of a unique biomaterial with mechanical properties enabling patterning (i.e. perfusion channels) and capable of supporting the formation of

neuronal networks. This material is thus promising as a component of platforms to study neurological diseases. The peptide N-cadherin, which is known to promote synaptic formation and plasticity, was conjugated to GelMA. The addition of this extracellular marker, in combination with the naturally present RGD motif, enabled long term (relative to prior strategies) single neuron cell viability in a hydrogel and the formation of interconnected neuronal networks, results that have been previously unattainable. This material may yield new insight regarding neuronal pathophysiology and drug discovery of new compounds for a wide range of neurological disease.

Additionally, Aim 3 demonstrated the development of a perfusable, SMC-laden construct to model the human ductus arteriosus. Over the course of a week, the embedded hDA SMCs aligned perpendicular to the direction of perfusion, similar to architecture seen *in vivo*. This new system has the potential to facilitate rapid screening of drug candidates for treating patent ductus arteriosus, a critical need for addressing a prevalent and common congenital heart defect.

Together, these studies show that the combination of a new pump perfusion system and novel biomaterials can be applied to a wide range of applications to address current gaps in tools used for biological studies. Additionally, these tissue construct approaches may be applied to study more relevant *in vitro* models of neurological and arterial diseases to evaluate disease progression, drug efficacy and screening of novel therapeutics.

7.2 Limitations

The pump perfusion system has been successfully applied to support perfusable hydrogel constructs and is more equipped to meet unique user demands compared to the expensive commercial systems. However, it should be noted that this system requires a non-trivial amount of time to build and assemble. The total time to construct the pump perfusion system is

approximately 24 hours, including the time to 3D print the housing unit, pumpheads and stepper motor brackets. This time also includes soldering, crimping and programming, which for inexperienced users would likely take more time in the process of assembling the unit. While the required level of prior knowledge of electronics and CAD software is low, soldering and understanding the basics of electronics is necessary.

The hydrogel platforms developed in this work also have some limitations. First, the gelatin hydrogel with embedded perfusion channels developed for spatiotemporal control of morphogen delivery used only two parallel channels (Chapter 4). More complex geometries would be useful for additional presentation of factors to control stem cell fate. Additionally, the computational diffusion model requires input of a measured diffusion coefficient using methods such as Raman microscopy or confocal microscopy. Many molecules of interest, including BMP-2 and TGFβ1, are not detectable with either of these methods so it is a challenge to determine the diffusion coefficient of the morphogens themselves in specific hydrogels. However, one strategy to overcome this limitation is to find molecules of similar size and charge that are Raman active or fluorescent.

As mentioned in Chapter 5, the GelMA-Cad hydrogel has the potential to support embedded perfusion channels and single cell neurons. However, this work was focused on the development and characterization of the material and survival of single cell neurons; perfusion channels have not been incorporated into cell laden GelMA-Cad hydrogels. Data from Chapters 4 and 5 indicate that this next step is achievable.

Finally, the artificial artery construct described in Chapter 6 has a few limitations. First, the human ductus artery is a multilayered vessel that has multiple cell types. Our system contains only one cell type (SMCs) and does not have the ordered layering present. While this study is

intended as a proof of concept for studying hDA cells in a 3D perfusable matrix (which is more physiologically relevant than 2D culture), the addition of a layer of endothelial cells lining the inner lumen of the "vessel" would provide an additional level of physiological similarity. Second, the size of the current construct is larger than that of the native vessel. The human ductus arteriosus in a 34-week gestational stage is approximately 3.49mm in diameter. This is a significantly smaller diameter than that of our in vitro model (6.35mm diameter). An hDA hydrogel construct with a diameter more similar to that of the native vessel would likely improve the future characterization of the functional response to drugs that are meant to constrict and occlude the ductus arteriosus.

7.3 Future Directions

The limitations described in 7.2 can be addressed with several future studies. First, the perfused hydrogel construct with spatiotemporal control of morphogen presentation can be expanded to include different cell types and more complex channel geometries. These modifications would allow for differentiation of stem cells into other, more spatially complex tissues. Current techniques for creating multi-cellular organoids often include fusing two spheroids together. This state-of-the-art technique is limited by the small surface area of the spheroids. Thus, limiting the available space to fuse multiple organoids together to generate multiple region-specific areas (like that found in the neural tube). In the system developed in Chapter 4, a 4-channel structure could be patterned in the hydrogel to direct morphogen delivery for an *in vitro* model of neural tube formation. In the top and bottom channel, the anterior-posterior axis can be generated through opposing gradients of RA and FGF. These morphogens could be delivered in the two isolated channels to induce a gradient of differentiation, much like what is seen in the developing neural tube. In the other two channels, the dorso-ventral axis, opposing gradients of SHH and BMP

can be generated to induce differentiation into the notochord and the floor plate, respectively. Applying this system to develop more complex gradients would advance the field of stem cell differentiation and deepen our understanding of the stem cell niche.

The next step for the GelMA-Cad biomimetic hydrogel in neuronal network research is to introduce disease pathology to the system. For example, an unanswered question in Alzheimer's disease pathology is how amyloid beta propagates and spreads throughout the brain. To date, the ability to observe this phenomenon in vitro in a neuronal network within which individual cells and axons can be distinguished has been unobtainable. Current attempts to embed single cell iPSC derived neurons in 3D networks have used Matrigel, silk and hyaluronic acid. In each of these systems, single cell neurons migrate towards each other and create large cell masses. This migration and growth does not allow the real-time visualization of disease progression. There has been progress in the use of neural organoids to study disease pathology; however, the same issue with the aforementioned biomaterials still exists: individual neurons/axons cannot be distinguished within the confluent organoid. Here we have demonstrated that we can support single cell seeding and the formation of a neuronal network upon which disease studies can be performed and results can be obtained with single cell resolution. Future studies would incorporate the use of our novel biomaterial for the single cell suspension, neuronal network formation and incorporation of disease pathology. In neurobiology studies, Nanoject devices have been used to deliver nanoliter amounts of substances. In these future studies, the use of this technology to deliver amyloid beta or tau to single cell neurons would enable users to track the disease progression using non-destructive and noninvasive imaging techniques. Additionally, with the use of the image analysis software applied to the neuronal network in this thesis, users would be able to quantify real time changes in cell

body counts, axon diameter, and axon length. Such tools would benefit the field of neuroscience by enabling users to visualize the progression of disease and gain insight into disease propagation.

Future work with hDA cell laden hydrogel constructs developed in this thesis should incorporate the concentric seeding of other cell types, such as endothelial cells, and the reduction of the construct diameter. Many existing microfluidic devices incorporate monolayers of endothelial cells in the perfusion channel with smooth muscle cells embedded in a 3D matrix around the endothelial cells. These smaller constructs are closer in diameter to the native human DA than the hydrogel construct developed in this thesis. However, in these devices the embedded smooth muscle cells do not orient perpendicular to the direction of flow which is a characteristic of the current construct that mimics the native vessel. In combination with incorporating multiple cell layers, decreasing the construct diameter and introducing pulsatile perfusion are the next steps for increasing the physiological relevance of our *in vitro* hDA model and strengthening its utility as a basic science tool and drug screening platform.

7.4 Conclusion

An engineered system that models diffusion and allows for dynamic, user-controlled delivery of multiple morphogens has been developed in this dissertation to overcome current constraints to manipulate cell fate in a large 3D system. Additionally, this work describes an innovative bioinstructive material that allows for single cell neuronal suspension in a perfusable construct. This biomaterial has allowed for the visualization, growth and quantification of single cell bodies and axons in a 3D environment and can serve as a platform for modeling disease progression. Finally, this work describes the embedding of human ductus arteriosus cells in a perfusable construct that induces the smooth muscle cells to align perpendicular to the direction of

flow and constricts similarly to the *in vivo* artery. This system can be used to develop new drug therapies for patent ductus arteriosus.

REFERENCES

1. V. Prasad, Translation failure and medical reversal: Two sides to the same coin, Eur. J. Cancer. (2016). doi:10.1016/j.ejca.2015.08.024.

2. A.J. London, J. Kimmelman, Why clinical translation cannot succeed without failure, Elife. (2015). doi:10.7554/eLife.12844.

3. I.W.Y. Mak, N. Evaniew, M. Ghert, Lost in translation: Animal models and clinical trials in cancer treatment, Am. J. Transl. Res. (2014). doi:1943-8141/AJTR1312010.

4. D.B. Fogel, Factors associated with clinical trials that fail and opportunities for improving the likelihood of success: A review, Contemp. Clin. Trials Commun. (2018). doi:10.1016/j.conctc.2018.08.001.

5. M.J. Fromer, FDA Introduces New Phase 0 for Clinical Trials, Oncol. Times. (2013). doi:10.1097/01.cot.0000293387.34124.a8.

6. A.Y. Hsiao, Y.C. Tung, X. Qu, L.R. Patel, K.J. Pienta, S. Takayama, 384 hanging drop arrays give excellent Z-factors and allow versatile formation of co-culture spheroids, Biotechnol. Bioeng. (2012). doi:10.1002/bit.24399.

7. Y.C. Tung, A.Y. Hsiao, S.G. Allen, Y.S. Torisawa, M. Ho, S. Takayama, High-throughput 3D spheroid culture and drug testing using a 384 hanging drop array, Analyst. (2011). doi:10.1039/c0an00609b.

8. W. Ma, T. Tavakoli, E. Derby, Y. Serebryakova, M.S. Rao, M.P. Mattson, Cell-extracellular matrix interactions regulate neural differentiation of human embryonic stem cells, BMC Dev. Biol. (2008). doi:10.1186/1471-213X-8-90.

9. L. Pan, Y. Ren, F. Cui, Q. Xu, Viability and differentiation of neural precursors on hyaluronic acid hydrogel scaffold, J. Neurosci. Res. (2009). doi:10.1002/jnr.22142.

10. A.M. Hopkins, L. De Laporte, F. Tortelli, E. Spedden, C. Staii, T.J. Atherton, J.A. Hubbell, D.L. Kaplan, Silk hydrogels as soft substrates for neural tissue engineering, Adv. Funct. Mater. (2013). doi:10.1002/adfm.201300435.

11. B. V. Sridhar, J.L. Brock, J.S. Silver, J.L. Leight, M.A. Randolph, K.S. Anseth, Development of a cellularly degradable PEG hydrogel to promote articular cartilage extracellular matrix deposition, Adv. Healthc. Mater. (2015). doi:10.1002/adhm.201400695.

12. E. Alsberg, K.W. Anderson, A. Albeiruti, R.T. Franceschi, D.J. Mooney, Cell-interactive alginate hydrogels for bone tissue engineering, J. Dent. Res. (2001). doi:10.1177/00220345010800111501.

13. T.R. Sodunke, K.K. Turner, S.A. Caldwell, K.W. McBride, M.J. Reginato, H.M. Noh,

Micropatterns of Matrigel for three-dimensional epithelial cultures, Biomaterials. (2007). doi:10.1016/j.biomaterials.2007.05.021.

14. K.L. Sodek, T.J. Brown, M.J. Ringuette, Collagen I but not Matrigel matrices provide an MMP-dependent barrier to ovarian cancer cell penetration, BMC Cancer. (2008). doi:10.1186/1471-2407-8-223.

15. Y. Fang, R.M. Eglen, Three-Dimensional Cell Cultures in Drug Discovery and Development, SLAS Discov. (2017). doi:10.1177/1087057117696795.

16. X. Guan, M. Avci-Adali, E. Alarçin, H. Cheng, S.S. Kashaf, Y. Li, A. Chawla, H.L. Jang, A. Khademhosseini, Development of hydrogels for regenerative engineering, Biotechnol. J. 12 (2017). doi:10.1002/biot.201600394.

17. S. Giulitti, E. Magrofuoco, L. Prevedello, N. Elvassore, Optimal periodic perfusion strategy for robust long-term microfluidic cell culture, Lab Chip. 13 (2013) 4430. doi:10.1039/c3lc50643f.

18. J.S. Miller, K.R. Stevens, M.T. Yang, B.M. Baker, D.H.T. Nguyen, D.M. Cohen, E. Toro, A.A. Chen, P.A. Galie, X. Yu, R. Chaturvedi, S.N. Bhatia, C.S. Chen, Rapid casting of patterned vascular networks for perfusable engineered three-dimensional tissues, Nat. Mater. 11 (2012) 768–774. doi:10.1038/nmat3357.

19. R.L. Smith, C.J. Demers, S.D. Collins, Microfluidic device for the combinatorial application and maintenance of dynamically imposed diffusional gradients, Microfluid. Nanofluidics. 9 (2010) 613–622. doi:10.1007/s10404-010-0574-7.

20. R. Thakur, Y. Zhang, A. Amin, S. Wereley, Programmable microfluidic platform for spatiotemporal control over nanoliter droplets, Microfluid. Nanofluidics. 18 (2015) 1425–1431. doi:10.1007/s10404-014-1507-7.

21. F. Yanagawa, S. Sugiura, T. Kanamori, Hydrogel microfabrication technology toward three dimensional tissue engineering, Regen. Ther. 3 (2016) 45–57. doi:10.1016/j.reth.2016.02.007.

22. X. Wang, E. Wenk, X. Zhang, L. Meinel, G. Vunjak-Novakovic, D.L. Kaplan, Growth factor gradients via microsphere delivery in biopolymer scaffolds for osteochondral tissue engineering, J. Control. Release. 134 (2009) 81–90. doi:10.1016/j.jconrel.2008.10.021.

23. B. K.H., D. S., H. B., H. A., J. A., J. K.-J., K. K., K. H.J., M. L., M. R., M. S., T. Y.-S., V.D.M. A.D., V. R., Y. M., P. K.K., Engineered in vitro disease models, Annu. Rev. Pathol. Mech. Dis. (2015). doi:http://dx.doi.org/10.1146/annurev-pathol-012414-040418.

24. A.M. Yakoub, M. Sadek, Development and Characterization of Human Cerebral Organoids: An Optimized Protocol, Cell Transplant. (2018). doi:10.1177/0963689717752946.

25. P. Zhuang, A.X. Sun, J. An, C.K. Chua, S.Y. Chew, 3D neural tissue models: From spheroids to bioprinting, Biomaterials. (2018). doi:10.1016/j.biomaterials.2017.10.002.

26. H. Wang, Modeling Neurological Diseases With Human Brain Organoids, Front. Synaptic Neurosci. (2018). doi:10.3389/fnsyn.2018.00015.

27. V. Iefremova, G. Manikakis, O. Krefft, A. Jabali, K. Weynans, R. Wilkens, F. Marsoner, B. Brändl, F.J. Müller, P. Koch, J. Ladewig, An Organoid-Based Model of Cortical Development Identifies Non-Cell-Autonomous Defects in Wnt Signaling Contributing to Miller-Dieker Syndrome, Cell Rep. (2017). doi:10.1016/j.celrep.2017.03.047.

28. M.A. Lancaster, M. Renner, C.A. Martin, D. Wenzel, L.S. Bicknell, M.E. Hurles, T. Homfray, J.M. Penninger, A.P. Jackson, J.A. Knoblich, Cerebral organoids model human brain development and microcephaly, Nature. (2013). doi:10.1038/nature12517.

29. W.L. Cantley, C. Du, S. Lomoio, T. Depalma, E. Peirent, D. Kleinknecht, M. Hunter, M.D. Tang-Schomer, G. Tesco, D.L. Kaplan, Functional and Sustainable 3D Human Neural Network Models from Pluripotent Stem Cells, ACS Biomater. Sci. Eng. (2018). doi:10.1021/acsbiomaterials.8b00622.

30. K. Chwalek, D. Sood, W.L. Cantley, J.D. White, M. Tang-Schomer, D.L. Kaplan, Engineered 3D Silk-collagen-based Model of Polarized Neural Tissue, J. Vis. Exp. (2015). doi:10.3791/52970.

31. D.J. Schneider, J.W. Moore, Patent ductus arteriosus, Circulation. 114 (2006) 1873–1882. doi:10.1161/CIRCULATIONAHA.105.592063.

32. W.E. Benitz, Patent Ductus Arteriosus in Preterm Infants, Pediatrics. 137 (2016) e20153730. doi:10.1542/peds.2015-3730.

33. J.D. Kakisis, C.D. Liapis, C. Breuer, B.E. Sumpio, Artificial blood vessel: The Holy Grail of peripheral vascular surgery, J. Vasc. Surg. (2005). doi:10.1016/j.jvs.2004.12.026.

34. J. Reese, Patent Ductus Arteriosus: Mechanisms and Management, Semin. Perinatol. 36 (2012) 89–91. doi:10.1053/j.semperi.2011.09.017.

35. E.L. Shelton, G.K. Singh, C.G. Nichols, Novel drug targets for ductus arteriosus manipulation: Looking beyond prostaglandins, Semin. Perinatol. (2018). doi:10.1053/j.semperi.2018.05.004.

36. F. Guillemot, Spatial and temporal specification of neural fates by transcription factor codes, Development. (2007). doi:10.1242/dev.006379.

37. F. Ulloa, J. Briscoe, Morphogens and the control of cell proliferation and patterning in the spinal cord, Cell Cycle. (2007). doi:10.4161/cc.6.21.4822.

38. Y.K. Bae, N. Trisnadi, S. Kadam, A. Stathopoulos, The role of FGF signaling in guiding coordinate movement of cell groups guidance cue and cell adhesion regulator?, Cell Adhes. Migr. (2012). doi:10.4161/cam.21103.

39. G.M. Morrison, I. Oikonomopoulou, R.P. Migueles, S. Soneji, A. Livigni, T. Enver, J.M. Brickman, Anterior Definitive Endoderm from ESCs Reveals a Role for FGF Signaling, Cell Stem Cell. (2008). doi:10.1016/j.stem.2008.07.021.

40. Y.-K. Bae, N. Trisnadi, S. Kadam, A. Stathopoulos, The role of FGF signaling in guiding coordinate movement of cell groups, Cell Adh. Migr. (2012). doi:10.4161/cam.21103.

41. R. Mayor, S. Etienne-Manneville, The front and rear of collective cell migration, Nat. Rev. Mol. Cell Biol. (2016). doi:10.1038/nrm.2015.14.

42. A. Aulehla, O. Pourquié, Signaling gradients during paraxial mesoderm development., Cold Spring Harb. Perspect. Biol. (2010). doi:10.1101/cshperspect.a000869.

43. G. Le Dréau, E. Martí, Dorsal-ventral patterning of the neural tube: A tale of three signals, Dev. Neurobiol. (2012). doi:10.1002/dneu.22015.

44. T.W. Sadler, Embryology of neural tube development, in: Am. J. Med. Genet. - Semin. Med. Genet., 2005: pp. 2–8. doi:10.1002/ajmg.c.30049.

45. K. Lage, K. Møllgård, S. Greenway, H. Wakimoto, J.M. Gorham, C.T. Workman, E. Bendsen, N.T. Hansen, O. Rigina, F.S. Roque, C. Wiese, V.M. Christoffels, A.E. Roberts, L.B. Smoot, W.T. Pu, P.K. Donahoe, N. Tommerup, S. Brunak, C.E. Seidman, J.G. Seidman, L.A. Larsen, Dissecting spatio-temporal protein networks driving human heart development and related disorders, Mol. Syst. Biol. (2010). doi:10.1038/msb.2010.36.

46. P. Buske, J. Galle, N. Barker, G. Aust, H. Clevers, M. Loeffler, A comprehensive model of the spatio-temporal stem cell and tissue organisation in the intestinal crypt, PLoS Comput. Biol. (2011). doi:10.1371/journal.pcbi.1001045.

47. K. Duval, H. Grover, L.-H. Han, Y. Mou, A.F. Pegoraro, J. Fredberg, Z. Chen, Modeling Physiological Events in 2D vs. 3D Cell Culture, Physiology. (2017).

48. E. Sjögren, B. Abrahamsson, P. Augustijns, D. Becker, M.B. Bolger, M. Brewster, J. Brouwers, T. Flanagan, M. Harwood, C. Heinen, R. Holm, H.P. Juretschke, M. Kubbinga, A. Lindahl, V. Lukacova, U. Münster, S. Neuhoff, M.A. Nguyen, A. Van Peer, C. Reppas, A.R. Hodjegan, C. Tannergren, W. Weitschies, C. Wilson, P. Zane, H. Lennernäs, P. Langguth, In vivo methods for drug absorption - Comparative physiologies, model selection, correlations with in vitro methods (IVIVC), and applications for formulation/API/excipient characterization including food effects, Eur. J. Pharm. Sci. (2014). doi:10.1016/j.ejps.2014.02.010.

49. A.I. Pearce, R.G. Richards, S. Milz, E. Schneider, S.G. Pearce, Animal models for implant biomaterial research in bone: A review, Eur. Cells Mater. (2007). doi:10.22203/eCM.v013a01.

50. C.L. Watson, M.M. Mahe, J. Múnera, J.C. Howell, N. Sundaram, H.M. Poling, J.I. Schweitzer, J.E. Vallance, C.N. Mayhew, Y. Sun, G. Grabowski, S.R. Finkbeiner, J.R. Spence, N.F. Shroyer, J.M. Wells, M.A. Helmrath, An in vivo model of human small intestine using pluripotent stem cells, Nat. Med. (2014). doi:10.1038/nm.3737.

51. C.M. Madl, B.L. Lesavage, R.E. Dewi, C.B. Dinh, R.S. Stowers, M. Khariton, K.J. Lampe, D. Nguyen, O. Chaudhuri, A. Enejder, S.C. Heilshorn, Maintenance of neural progenitor cell stemness in 3D hydrogels requires matrix remodelling, Nat. Mater. (2017).

doi:10.1038/nmat5020.

52. N.S. Bhise, J. Ribas, V. Manoharan, Y.S. Zhang, A. Polini, S. Massa, M.R. Dokmeci, A. Khademhosseini, Organ-on-a-chip platforms for studying drug delivery systems, J. Control. Release. 190 (2014) 82–93. doi:10.1016/j.jconrel.2014.05.004.

53. D. Huh, G.A. Hamilton, D.E. Ingber, From 3D cell culture to organs-on-chips, Trends Cell Biol. 21 (2011) 745–754. doi:10.1016/j.tcb.2011.09.005.

54. S. Kim, S. Takayama, Organ-on-a-chip and the kidney, Kidney Res. Clin. Pract. 34 (2015) 165–169. doi:10.1016/j.krcp.2015.08.001.

55. C.J. Demers, P. Soundararajan, P. Chennampally, G.A. Cox, J. Briscoe, S.D. Collins, R.L. Smith, Development-on-chip: *in vitro* neural tube patterning with a microfluidic device, Development. (2016). doi:10.1242/dev.126847.

56. I. Maschmeyer, A.K. Lorenz, K. Schimek, T. Hasenberg, A.P. Ramme, J. Hübner, M. Lindner, C. Drewell, S. Bauer, A. Thomas, N.S. Sambo, F. Sonntag, R. Lauster, U. Marx, A four-organ-chip for interconnected long-term co-culture of human intestine, liver, skin and kidney equivalents, Lab Chip. 15 (2015) 2688–2699. doi:10.1039/c5lc00392j.

57. P. Loskill, T. Sezhian, K.M. Tharp, F.T. Lee-Montiel, S. Jeeawoody, W.M. Reese, P.-J.H. Zushin, A. Stahl, K.E. Healy, WAT-on-a-chip: a physiologically relevant microfluidic system incorporating white adipose tissue, Lab Chip. 17 (2017) 1645–1654. doi:10.1039/C6LC01590E.

58. M.W. van der Helm, A.D. van der Meer, J.C.T. Eijkel, A. van den Berg, L.I. Segerink, Microfluidic organ-on-chip technology for blood-brain barrier research, Tissue Barriers. 4 (2016). doi:10.1080/21688370.2016.1142493.

59. R. Morizane, J. V. Bonventre, Kidney Organoids: A Translational Journey, Trends Mol. Med. (2017). doi:10.1016/j.molmed.2017.01.001.

60. K.J. Jang, A.P. Mehr, G.A. Hamilton, L.A. McPartlin, S. Chung, K.Y. Suh, D.E. Ingber, Human kidney proximal tubule-on-a-chip for drug transport and nephrotoxicity assessment, Integr. Biol. (United Kingdom). (2013). doi:10.1039/c3ib40049b.

61. J.U. Lind, T.A. Busbee, A.D. Valentine, F.S. Pasqualini, H. Yuan, M. Yadid, S.J. Park, A. Kotikian, A.P. Nesmith, P.H. Campbell, J.J. Vlassak, J.A. Lewis, K.K. Parker, Instrumented cardiac microphysiological devices via multimaterial three-dimensional printing, Nat. Mater. (2017). doi:10.1038/nmat4782.

62. J. Yang, Y.S. Zhang, K. Yue, A. Khademhosseini, Cell-laden hydrogels for osteochondral and cartilage tissue engineering, Acta Biomater. 57 (2017) 1–25. doi:10.1016/j.actbio.2017.01.036.

63. A.H. Nguyen, J. McKinney, T. Miller, T. Bongiorno, T.C. McDevitt, Gelatin methacrylate microspheres for controlled growth factor release, Acta Biomater. 13 (2015) 101–110. doi:10.1016/j.actbio.2014.11.028.

64. K.M. Poole, C.E. Nelson, R. V. Joshi, J.R. Martin, M.K. Gupta, S.C. Haws, T.E. Kavanaugh, M.C. Skala, C.L. Duvall, ROS-responsive microspheres for on demand antioxidant therapy in a model of diabetic peripheral arterial disease, Biomaterials. (2015). doi:10.1016/j.biomaterials.2014.11.016.

65. K. Chwalek, M.D. Tang-Schomer, F.G. Omenetto, D.L. Kaplan, In vitro bioengineered model of cortical brain tissue, Nat. Protoc. (2015). doi:10.1038/nprot.2015.091.

66. D. Zhang, M. Pekkanen-Mattila, M. Shahsavani, A. Falk, A.I. Teixeira, A. Herland, A 3D Alzheimer's disease culture model and the induction of P21-activated kinase mediated sensing in iPSC derived neurons, Biomaterials. (2014). doi:10.1016/j.biomaterials.2013.11.028.

67. D. Zhang, M. Pekkanen-Mattila, M. Shahsavani, A. Falk, A.I. Teixeira, A. Herland, A 3D Alzheimer's disease culture model and the induction of P21-activated kinase mediated sensing in iPSC derived neurons, Biomaterials. (2014). doi:10.1016/j.biomaterials.2013.11.028.

68. U.A. Aregueta-Robles, P.J. Martens, L.A. Poole-Warren, R.A. Green, Tissue engineered hydrogels supporting 3D neural networks, Acta Biomater. (2018). doi:10.1016/j.actbio.2018.11.044.

69. D.G.R. Tervo, B.Y. Hwang, S. Viswanathan, T. Gaj, M. Lavzin, K.D. Ritola, S. Lindo, S. Michael, E. Kuleshova, D. Ojala, C.C. Huang, C.R. Gerfen, J. Schiller, J.T. Dudman, A.W. Hantman, L.L. Looger, D. V. Schaffer, A.Y. Karpova, A Designer AAV Variant Permits Efficient Retrograde Access to Projection Neurons, Neuron. (2016). doi:10.1016/j.neuron.2016.09.021.

70. N.L. Chamberlin, B. Du, S. De Lacalle, C.B. Saper, Recombinant adeno-associated virus vector: Use for transgene expression and anterograde tract tracing in the CNS, Brain Res. (1998). doi:10.1016/S0006-8993(98)00169-3.

71. B. Zingg, X. lin Chou, Z. gang Zhang, L. Mesik, F. Liang, H.W. Tao, L.I. Zhang, AAV-Mediated Anterograde Transsynaptic Tagging: Mapping Corticocollicular Input-Defined Neural Pathways for Defense Behaviors, Neuron. (2017). doi:10.1016/j.neuron.2016.11.045.

72. A. Chatzigeorgiou, A. Halapas, K. Kalafatakis, E.F. Kamper, The use of animal models in the study of diabetes mellitus, In Vivo (Brooklyn). (2009). doi:23/2/245 [pii] ET - 2009/05/06.

73. G. Csányi, F.J. Miller, Oxidative stress in cardiovascular disease, Int. J. Mol. Sci. (2014). doi:10.3390/ijms15046002.

74. I. Falcao-Pires, A.F. Leite-Moreira, Animal models of cardiovascular diseaseines, in: Introd. to Transl. Cardiovasc. Res., 2015. doi:10.1007/978-3-319-08798-6_19.

75. Y.-T. Hsieh, N.M. Liu, E. Ohmori, T. Yokota, I. Kajimura, T. Akaike, T. Ohshima, N. Goda, S. Minamisawa, Transcription Profiles of the Ductus Arteriosus in Brown-Norway

Rats With Irregular Elastic Fiber Formation, Circ. J. (2014). doi:10.1253/circj.CJ-13-1029.

76. X. Feng, L.T. Krebs, T. Gridley, Patent ductus arteriosus in mice with smooth muscle-specific Jag1 deletion, Development. (2010). doi:10.1242/dev.052043.

77. K. Sato, M. Nitta, A. Ogawa, A Microfluidic Cell Stretch Device to Investigate the Effects of Stretching Stress on Artery Smooth Muscle Cell Proliferation in Pulmonary Arterial Hypertension, Inventions. (2018). doi:10.3390/inventions4010001.

78. J. Schöneberg, F. De Lorenzi, B. Theek, A. Blaeser, D. Rommel, A.J.C. Kuehne, F. Kießling, H. Fischer, Engineering biofunctional in vitro vessel models using a multilayer bioprinting technique, Sci. Rep. (2018). doi:10.1038/s41598-018-28715-0.

79. A. Tan, K. Fujisawa, Y. Yukawa, Y.T. Matsunaga, Bottom-up fabrication of artery-mimicking tubular co-cultures in collagen-based microchannel scaffolds, Biomater. Sci. (2016). doi:10.1039/c6bm00340k.

80. B. De Bruyne, N.H.J. Pijls, B. Kalesan, E. Barbato, P. a Tonino, Z. Piroth, N. Jagic, S. Mobius-Winkler, G. Rioufol, N. Witt, P. Kala, P. MacCarthy, T. Engstrom, K.G. Oldroyd, K. Mavromatis, G. Manoharan, P. Verlee, O. Frobert, N. Curzen, J.B. Johnson, P. Juni, W.F. Fearon, Fame Trial Investigators, P.P. Transmission, B. De Bruyne, W.F. Fearon, N.H.J. Pijls, E. Barbato, P. a Tonino, Z. Piroth, N. Jagic, S. Mobius-Winckler, G. Rioufol, N. Witt, P. Kala, P. MacCarthy, T. Engström, K.G. Oldroyd, K. Mavromatis, G. Manoharan, P. Verlee, O. Frobert, N. Curzen, J.B. Johnson, A. Limacher, E. Nüesch, P. Jüni, Fractional flow reserve-guided PCI for stable coronary artery disease., N. Engl. J. Med. (2014). doi:10.1056/NEJMoa1205361.

81. M.W. Laschke, M.D. Menger, Life is 3D: Boosting Spheroid Function for Tissue Engineering, Trends Biotechnol. 35 (2017) 133–144. doi:10.1016/j.tibtech.2016.08.004.

82. D.B. Kolesky, K.A. Homan, M.A. Skylar-Scott, J.A. Lewis, Three-dimensional bioprinting of thick vascularized tissues, Proc. Natl. Acad. Sci. 113 (2016) 3179–3184. doi:10.1073/pnas.1521342113.

83. R. Edmondson, J.J. Broglie, A.F. Adcock, L. Yang, Three-Dimensional Cell Culture Systems and Their Applications in Drug Discovery and Cell-Based Biosensors, Assay Drug Dev. Technol. 12 (2014) 207–218. doi:10.1089/adt.2014.573.

84. G.Y. Huang, L.H. Zhou, Q.C. Zhang, Y.M. Chen, W. Sun, F. Xu, T.J. Lu, Microfluidic hydrogels for tissue engineering., Biofabrication. 3 (2011) 012001. doi:10.1088/1758-5082/3/1/012001.

85. I.K. Zervantonakis, C.R. Kothapalli, S. Chung, R. Sudo, R.D. Kamm, Microfluidic devices for studying heterotypic cell-cell interactions and tissue specimen cultures under controlled microenvironments, Biomicrofluidics. 5 (2011) 013406. doi:10.1063/1.3553237.

86. J.W. Song, W. Gu, N. Futai, K.A. Warner, J.E. Nor, S. Takayama, Computer-controlled

microcirculatory support system for endothelial cell culture and shearing, Anal. Chem. 77 (2005) 3993–3999. doi:10.1021/ac050131o.

87. L. Prodanov, R. Jindal, S.S. Bale, M. Hegde, W.J. Mccarty, I. Golberg, A. Bhushan, M.L. Yarmush, O.B. Usta, Long-term maintenance of a microfluidic 3D human liver sinusoid, Biotechnol. Bioeng. 113 (2016) 241–246. doi:10.1002/bit.25700.

88. D.E. Mogosanu, R. Verplancke, P. Dubruel, J. Vanfleteren, Fabrication of 3-dimensional biodegradable microfluidic environments for tissue engineering applications, Mater. Des. 89 (2016) 1315–1324. doi:10.1016/j.matdes.2015.10.046.

89. M. Karimi, S. Bahrami, H. Mirshekari, S.M.M. Basri, A.B. Nik, A.R. Aref, M. Akbari, M.R. Hamblin, Microfluidic systems for stem cell-based neural tissue engineering, Lab Chip. 16 (2016) 2551–2571. doi:10.1039/C6LC00489J.

90. S.A. Roberts, K.A. DiVito, F.S. Ligler, A.A. Adams, M.A. Daniele, Microvessel manifold for perfusion and media exchange in three-dimensional cell cultures, Biomicrofluidics. 10 (2016) 054109. doi:10.1063/1.4963145.

91. Z. Zhang, B. Wang, D. Hui, J. Qiu, S. Wang, 3D bioprinting of soft materials-based regenerative vascular structures and tissues, Compos. Part B Eng. 123 (2017) 279–291. doi:10.1016/j.compositesb.2017.05.011.

92. Q. Gao, Z. Liu, Z. Lin, J. Qiu, Y. Liu, A. Liu, Y. Wang, M. Xiang, B. Chen, J. Fu, Y. He, 3D Bioprinting of Vessel-like Structures with Multilevel Fluidic Channels, ACS Biomater. Sci. Eng. 3 (2017) 399–408. doi:10.1021/acsbiomaterials.6b00643.

93. J.M. Middendorf, D.J. Griffin, S. Shortkroff, C. Dugopolski, S. Kennedy, J. Siemiatkoski, I. Cohen, L.J. Bonassar, Mechanical properties and structure-function relationships of human chondrocyte-seeded cartilage constructs after in vitro culture, J. Orthop. Res. 35 (2017) 2298–2306. doi:10.1002/jor.23535.

94. G. Vunjak-Novakovic, Tissue engineering of the heart: An evolving paradigm, J. Thorac. Cardiovasc. Surg. 153 (2017) 593–595. doi:10.1016/j.jtcvs.2016.08.057.

95. K. Shimomura, B.B. Rothrauff, R.S. Tuan, Region-Specific Effect of the Decellularized Meniscus Extracellular Matrix on Mesenchymal Stem Cell-Based Meniscus Tissue Engineering, Am. J. Sports Med. 45 (2017) 604–611. doi:10.1177/0363546516674184.

96. F.S. Frueh, M.D. Menger, N. Lindenblatt, P. Giovanoli, M.W. Laschke, Current and emerging vascularization strategies in skin tissue engineering, Crit. Rev. Biotechnol. 37 (2017) 613–625. doi:10.1080/07388551.2016.1209157.

97. S. Fleischer, R. Feiner, T. Dvir, Cutting-edge platforms in cardiac tissue engineering, Curr. Opin. Biotechnol. 47 (2017) 23–29. doi:10.1016/j.copbio.2017.05.008.

98. N.D. Legband, Development of Peritoneal Microbubble Oxygenation As an Extrapulmonary Treatment for Hypoxia, (2017). http://search.proquest.com/openview/c0f69198b39f95cb2f1aac71c01ef125/1?pq-origsite=gscholar&cbl=18750&diss=y (accessed July 10, 2017).

99. L.L. Munn, R.J. Melder, R.K. Jain, Analysis of cell flux in the parallel plate flow chamber: implications for cell capture studies, Biophys. J. 67 (1994) 889–895. doi:10.1016/S0006-3495(94)80550-8.

100. S. Sart, S.N. Agathos, Y. Li, T. Ma, Regulation of mesenchymal stem cell 3D microenvironment: From macro to microfluidic bioreactors, Biotechnol. J. 11 (2016) 43–57. doi:10.1002/biot.201500191.

101. M. Bond, G. Vadasz, A. V. Somlyo, A.P. Somlyo, Subcellular calcium and magnesium mobilization in rat liver stimulated in vivo with vasopressin and glucagon, J. Biol. Chem. 262 (1987) 1884–1892. doi:10.1242/dev.126847.

102. M. Buckingham, S. Meilhac, S. Zaffran, Building the mammalian heart from two sources of myocardial cells, Nat. Rev. Genet. 6 (2005) 826–835. doi:10.1038/nrg1710.

103. M.J. Birket, M.C. Ribeiro, A.O. Verkerk, D. Ward, A.R. Leitoguinho, S.C. Den Hartogh, V. V. Orlova, H.D. Devalla, V. Schwach, M. Bellin, R. Passier, C.L. Mummery, Expansion and patterning of cardiovascular progenitors derived from human pluripotent stem cells, Nat. Biotechnol. 33 (2015) 970–979. doi:10.1038/nbt.3271.

104. M.D. Schneider, Upstairs, Downstairs: Atrial and Ventricular Cardiac Myocytes from Human Pluripotent Stem Cells, Cell Stem Cell. 21 (2017) 151–152. doi:10.1016/j.stem.2017.07.006.

105. J.-F. Beaulieu, Differential expression of the VLA family of integrins along the crypt-villus axis in the human small intestine., J. Cell Sci. 102 (1992) 427–36. http://www.ncbi.nlm.nih.gov/pubmed/1506425.

106. N. Barker, Adult intestinal stem cells: Critical drivers of epithelial homeostasis and regeneration, Nat. Rev. Mol. Cell Biol. 15 (2014) 19–33. doi:10.1038/nrm3721.

107. S.W. Lane, D.A. Williams, F.M. Watt, Modulating the stem cell niche for tissue regeneration, Nat. Biotechnol. 32 (2014) 795–803. doi:10.1038/nbt.2978.

108. E.S. Lippmann, C. E.williams, D.A. Ruhl, M.C. Estevez-Silva, E.R. Chapman, J.J. Coon, R.S. Ashton, Deterministic HOX patterning in human pluripotent stem cell-derived neuroectoderm, Stem Cell Reports. 4 (2015) 632–644. doi:10.1016/j.stemcr.2015.02.018.

109. M. Gouti, A. Tsakiridis, F.J. Wymeersch, Y. Huang, J. Kleinjung, V. Wilson, J. Briscoe, In vitro generation of neuromesodermal progenitors reveals distinct roles for wnt signalling in the specification of spinal cord and paraxial mesoderm identity, PLoS Biol. 12 (2014). doi:10.1371/journal.pbio.1001937.

110. M.A. Kinney, T.C. McDevitt, Emerging strategies for spatiotemporal control of stem cell fate and morphogenesis, Trends Biotechnol. 31 (2013) 78–84. doi:10.1016/j.tibtech.2012.11.001.

111. T.N. Meyer, C. Schwesinger, K.T. Bush, R.O. Stuart, D.W. Rose, M.M. Shah, D.A. Vaughn, D.L. Steer, S.K. Nigam, Spatiotemporal regulation of morphogenetic molecules during in vitro branching of the isolated ureteric bud: Toward a model of branching

through budding in the developing kidney, Dev. Biol. 275 (2004) 44–67. doi:10.1016/j.ydbio.2004.07.022.

112. U. Dhawan, H.A. Pan, M.J. Shie, Y.H. Chu, G.S. Huang, P.C. Chen, W.L. Chen, The Spatiotemporal Control of Osteoblast Cell Growth, Behavior, and Function Dictated by Nanostructured Stainless Steel Artificial Microenvironments, Nanoscale Res. Lett. 12 (2017) 1–10. doi:10.1186/s11671-016-1810-1.

113. D. Barati, S.R.P. Shariati, S. Moeinzadeh, J.M. Melero-Martin, A. Khademhosseini, E. Jabbari, Spatiotemporal release of BMP-2 and VEGF enhances osteogenic and vasculogenic differentiation of human mesenchymal stem cells and endothelial colony-forming cells co-encapsulated in a patterned hydrogel, J. Control. Release. 223 (2016) 126–136. doi:10.1016/j.jconrel.2015.12.031.

114. T.E. Brown, K.S. Anseth, Spatiotemporal hydrogel biomaterials for regenerative medicine, Chem. Soc. Rev. 46 (2017) 6532–6552. doi:10.1039/c7cs00445a.

115. F.M. Chen, M. Zhang, Z.F. Wu, Toward delivery of multiple growth factors in tissue engineering, Biomaterials. 31 (2010) 6279–6308. doi:10.1016/j.biomaterials.2010.04.053.

116. T.N. Vo, F.K. Kasper, A.G. Mikos, Strategies for controlled delivery of growth factors and cells for bone regeneration, Adv. Drug Deliv. Rev. 64 (2012) 1292–1309. doi:10.1016/j.addr.2012.01.016.

117. S. Sant, M.J. Hancock, J.P. Donnelly, D. Iyer, A. Khademhosseini, Biomimetic gradient hydrogels for tissue engineering, Can. J. Chem. Eng. 88 (2010) 899–911. doi:10.1002/cjce.20411.

118. A.D. Van Der Meer, A. Van Den Berg, Organs-on-chips: Breaking the in vitro impasse, Integr. Biol. 4 (2012) 461–470. doi:10.1039/c2ib00176d.

119. K. Sakaguchi, T. Shimizu, S. Horaguchi, H. Sekine, M. Yamato, M. Umezu, T. Okano, In vitro engineering of vascularized tissue surrogates, Sci. Rep. 3 (2013). doi:10.1038/srep01316.

120. S. Cosson, M.P. Lutolf, Hydrogel microfluidics for the patterning of pluripotent stem cells, Sci. Rep. 4 (2014) 1–6. doi:10.1038/srep04462.

121. M.H. Wu, S. Bin Huang, G. Bin Lee, Microfluidic cell culture systems for drug research, Lab Chip. 10 (2010) 939–956. doi:10.1039/b921695b.

122. T.J. Cunningham, G. Duester, Mechanisms of retinoic acid signalling and its roles in organ and limb development, Nat. Rev. Mol. Cell Biol. (2015). doi:10.1038/nrm3932.

123. M. Uzkudun, L. Marcon, J. Sharpe, Data-driven modelling of a gene regulatory network for cell fate decisions in the growing limb bud, Mol. Syst. Biol. 11 (2015) 815–815. doi:10.15252/msb.20145882.

124. S.A. Rankin, L. Han, K.W. McCracken, A.P. Kenny, C.T. Anglin, E.A. Grigg, C.M. Crawford, J.M. Wells, J.M. Shannon, A.M. Zorn, A Retinoic Acid-Hedgehog Cascade

Coordinates Mesoderm-Inducing Signals and Endoderm Competence during Lung Specification, Cell Rep. 16 (2016) 66–78. doi:10.1016/j.celrep.2016.05.060.

125. S.A. Rankin, K.W. McCracken, D.M. Luedeke, L. Han, J.M. Wells, J.M. Shannon, A.M. Zorn, Timing is everything: Reiterative Wnt, BMP and RA signaling regulate developmental competence during endoderm organogenesis, Dev. Biol. 434 (2018) 121–132. doi:10.1016/j.ydbio.2017.11.018.

126. B. O'Grady, J. Wang, S. Faley, D. Balikov, E. Lippmann, L.M. Bellan, A Customizable, Low-Cost Perfusion System for Sustaining Tissue Constructs, SLAS Technol. (2018) 247263031877505. doi:10.1177/2472630318775059.

127. J. Crank, 1. The Diffusion Equations, in: Math. Diffus., 1975: pp. 2–5.

128. S. Kwak, M. Lafleur, Raman spectroscopy as a tool for measuring mutual-diffusion coefficients in hydrogels, Appl. Spectrosc. 57 (2003) 768–773. doi:10.1366/000370203322102843.

129. N. Jaiswal, S.E. Haynesworth, A.I. Caplan, S.P. Bruder, Osteogenic differentiation of purified, culture-expanded human mesenchymal stem cells in vitro, J. Cell. Biochem. 64 (1997) 295–312. doi:10.1002/(SICI)1097-4644(199702)64:2<295::AID-JCB12>3.0.CO;2-I.

130. F. Barry, R.E. Boynton, B. Liu, J.M. Murphy, Chondrogenic differentiation of mesenchymal stem cells from bone marrow: Differentiation-dependent gene expression of matrix components, Exp. Cell Res. 268 (2001) 189–200. doi:10.1006/excr.2001.5278.

131. C.W. Freudiger, W. Min, B.G. Saar, S. Lu, G.R. Holtom, C. He, J.C. Tsai, J.X. Kang, X.S. Xie, Label-free biomedical imaging with high sensitivity by stimulated raman scattering microscopy, Science (80-.). 322 (2008) 1857–1861. doi:10.1126/science.1165758.

132. C.W. Freudiger, W. Min, B.G. Saar, X.S. Xie, Stimulated Raman Scattering Microscopy for Label-Free Chemical Imaging, Opt. Photonics News. 20 (2009) 30. doi:10.1364/OPN.20.12.000030.

133. J.W. Westwater, H.G. Drickamer, The Mathematics of Diffusion, J. Am. Chem. Soc. 79 (1957) 1267–1268. doi:10.1021/ja01562a072.

134. M.C. Sala Alvarez, SIDA y enfermer??a. Abordaje desde atenci??n primaria., Rev. Enferm. 17 (1994) 23–28. doi:10.1016/S0168-3659(01)00467-9.

135. C.S. Dodson, A. V. Peresypkin, K. Rengarajan, S. Wu, J.M. Nickerson, Diffusion coefficients of retinoids, Curr. Eye Res. 24 (2002) 66–74. doi:10.1076/ceyr.24.1.66.5428.

136. A.M. Al-Baradi, M. Mears, R.A.L. Jones, M. Geoghegan, Diffusion of dextran within poly(methacrylic acid) hydrogels, J. Polym. Sci. Part B Polym. Phys. 50 (2012) 1286–1292. doi:10.1002/polb.23120.

137. T. Kihara, J. Ito, J. Miyake, Measurement of biomolecular diffusion in extracellular matrix condensed by fibroblasts using fluorescence correlation spectroscopy, PLoS One. 8

(2013). doi:10.1371/journal.pone.0082382.

138. M.F. Pittenger, A.M. Mackay, S.C. Beck, R.K. Jaiswal, R. Douglas, J.D. Mosca, M.A. Moorman, D.W. Simonetti, S. Craig, D.R. Marshak, Multilineage potential of adult human mesenchymal stem cells, Science (80-.). 284 (1999) 143–147. doi:10.1126/science.284.5411.143.

139. A.M. Mackay, S.C. Beck, J.M. Murphy, F.P. Barry, C.O. Chichester, M.F. Pittenger, Chondrogenic Differentiation of Cultured Human Mesenchymal Stem Cells from Marrow, Tissue Eng. 4 (1998) 415–428. doi:10.1089/ten.1998.4.415.

140. E.W. Esch, A. Bahinski, D. Huh, Organs-on-chips at the frontiers of drug discovery, Nat. Rev. Drug Discov. 14 (2015) 248–260. doi:10.1038/nrd4539.

141. I. Kelava, M.A. Lancaster, Dishing out mini-brains: Current progress and future prospects in brain organoid research, Dev. Biol. 420 (2016) 199–209. doi:10.1016/j.ydbio.2016.06.037.

142. R. Morizane, J. V. Bonventre, Kidney Organoids: A Translational Journey, Trends Mol. Med. 23 (2017) 246–263. doi:10.1016/j.molmed.2017.01.001.

143. M. Huch, H. Gehart, R. Van Boxtel, K. Hamer, F. Blokzijl, M.M.A. Verstegen, E. Ellis, M. Van Wenum, S.A. Fuchs, J. De Ligt, M. Van De Wetering, N. Sasaki, S.J. Boers, H. Kemperman, J. De Jonge, J.N.M. Ijzermans, E.E.S. Nieuwenhuis, R. Hoekstra, S. Strom, R.R.G. Vries, L.J.W. Van Der Laan, E. Cuppen, H. Clevers, Long-term culture of genome-stable bipotent stem cells from adult human liver, Cell. 160 (2015) 299–312. doi:10.1016/j.cell.2014.11.050.

144. P. Hoang, J. Wang, B.R. Conklin, K.E. Healy, Z. Ma, Generation of spatial-patterned early-developing cardiac organoids using human pluripotent stem cells, Nat. Protoc. 13 (2018) 723–737. doi:10.1038/nprot.2018.006.

145. L.M. Murrow, R.J. Weber, Z.J. Gartner, Dissecting the stem cell niche with organoid models: an engineering-based approach, Development. 144 (2017) 998–1007. doi:10.1242/dev.140905.

146. J.A. Bagley, D. Reumann, S. Bian, J. Lévi-Strauss, J.A. Knoblich, Fused cerebral organoids model interactions between brain regions, Nat. Methods. 14 (2017) 743–751. doi:10.1038/nmeth.4304.

147. T. Denayer, T. Stöhrn, M. Van Roy, Animal models in translational medicine: Validation and prediction, New Horizons Transl. Med. (2014). doi:10.1016/j.nhtm.2014.08.001.

148. J.A. Bolker, Animal Models in Translational Research: Rosetta Stone or Stumbling Block?, BioEssays. (2017). doi:10.1002/bies.201700089.

149. X.F. Tian, B.C. Heng, Z. Ge, K. Lu, A.J. Rufaihah, V.T.W. Fan, J.F. Yeo, T. Cao, Comparison of osteogenesis of human embryonic stem cells within 2D and 3D culture systems, Scand. J. Clin. Lab. Invest. (2008). doi:10.1080/00365510701466416.

150. Y. Imamura, T. Mukohara, Y. Shimono, Y. Funakoshi, N. Chayahara, M. Toyoda, N. Kiyota, S. Takao, S. Kono, T. Nakatsura, H. Minami, Comparison of 2D- and 3D-culture models as drug-testing platforms in breast cancer, Oncol. Rep. (2015). doi:10.3892/or.2015.3767.

151. M. Frega, M. Tedesco, P. Massobrio, M. Pesce, S. Martinoia, Network dynamics of 3D engineered neuronal cultures: A new experimental model for in-vitro electrophysiology, Sci. Rep. (2014). doi:10.1038/srep05489.

152. M. Georgiou, S.C.J. Bunting, H.A. Davies, A.J. Loughlin, J.P. Golding, J.B. Phillips, Engineered neural tissue for peripheral nerve repair, Biomaterials. (2013). doi:10.1016/j.biomaterials.2013.06.025.

153. D.D. McKinnon, T.E. Brown, K.A. Kyburz, E. Kiyotake, K.S. Anseth, Design and characterization of a synthetically accessible, photodegradable hydrogel for user-directed formation of neural networks, Biomacromolecules. (2014). doi:10.1021/bm500731b.

154. A. Fatehullah, S.H. Tan, N. Barker, Organoids as an in vitro model of human development and disease, Nat. Cell Biol. (2016). doi:10.1038/ncb3312.

155. C.R. Kothapalli, R.D. Kamm, 3D matrix microenvironment for targeted differentiation of embryonic stem cells into neural and glial lineages, Biomaterials. (2013). doi:10.1016/j.biomaterials.2013.04.042.

156. L. Ghasemi-Mobarakeh, Structural properties of scaffolds: Crucial parameters towards stem cells differentiation, World J. Stem Cells. (2015). doi:10.4252/wjsc.v7.i4.728.

157. K. Pietrucha, M. Zychowicz, M. Podobinska, L. Buzanska, Functional properties of different collagen scaffolds to create a biomimetic niche for neurally committed human induced pluripotent stem cells (iPSC), Folia Neuropathol. (2017). doi:10.5114/fn.2017.68578.

158. Z.-N. Zhang, B.C. Freitas, H. Qian, J. Lux, A. Acab, C.A. Trujillo, R.H. Herai, V.A. Nguyen Huu, J.H. Wen, S. Joshi-Barr, J. V. Karpiak, A.J. Engler, X.-D. Fu, A.R. Muotri, A. Almutairi, Layered hydrogels accelerate iPSC-derived neuronal maturation and reveal migration defects caused by MeCP2 dysfunction, Proc. Natl. Acad. Sci. (2016). doi:10.1073/pnas.1521255113.

159. C. Barry, M.T. Schmitz, N.E. Propson, Z. Hou, J. Zhang, B.K. Nguyen, J.M. Bolin, P. Jiang, B.E. McIntosh, M.D. Probasco, S. Swanson, R. Stewart, J.A. Thomson, M.P. Schwartz, W.L. Murphy, Uniform neural tissue models produced on synthetic hydrogels using standard culture techniques, Exp. Biol. Med. (2017). doi:10.1177/1535370217715028.

160. K.K. Kumar, E.W. Lowe, A.A. Aboud, M.D. Neely, R. Redha, J.A. Bauer, M. Odak, C.D. Weaver, J. Meiler, M. Aschner, A.B. Bowman, Cellular manganese content is developmentally regulated in human dopaminergic neurons, Sci. Rep. (2014). doi:10.1038/srep06801.

161. E.K. Hollmann, A.K. Bailey, A. V. Potharazu, M.D. Neely, A.B. Bowman, E.S. Lippmann, Accelerated differentiation of human induced pluripotent stem cells to blood-brain barrier endothelial cells, Fluids Barriers CNS. (2017). doi:10.1186/s12987-017-0059-0.

162. Y. Shi, P. Kirwan, F.J. Livesey, Directed differentiation of human pluripotent stem cells to cerebral cortex neurons and neural networks, Nat. Protoc. (2012). doi:10.1038/nprot.2012.116.

163. D. Loessner, C. Meinert, E. Kaemmerer, L.C. Martine, K. Yue, P.A. Levett, T.J. Klein, F.P.W. Melchels, A. Khademhosseini, D.W. Hutmacher, Functionalization, preparation and use of cell-laden gelatin methacryloyl-based hydrogels as modular tissue culture platforms, Nat. Protoc. (2016). doi:10.1038/nprot.2016.037.

164. L. Bian, M. Guvendiren, R.L. Mauck, J.A. Burdick, Hydrogels that mimic developmentally relevant matrix and N-cadherin interactions enhance MSC chondrogenesis, Proc. Natl. Acad. Sci. (2013). doi:10.1073/pnas.1214100110.

165. P.M. McClatchey, A.C. Keller, R. Bouchard, L.A. Knaub, J.E.B. Reusch, Fully automated software for quantitative measurements of mitochondrial morphology, Mitochondrion. (2016). doi:10.1016/j.mito.2015.12.003.

166. M. Shikanai, K. Nakajima, T. Kawauchi, N-Cadherin regulates radial glial fiber-dependent migration of cortical locomoting neurons, Commun. Integr. Biol. (2011). doi:10.4161/cib.4.3.14886.

167. H. Togashi, K. Abe, A. Mizoguchi, K. Takaoka, O. Chisaka, M. Takeichi, Cadherin regulates dendritic spine morphogenesis, Neuron. (2002). doi:10.1016/S0896-6273(02)00748-1.

168. I.B. Wanner, P.M. Wood, N-Cadherin Mediates Axon-Aligned Process Growth and Cell–Cell Interaction in Rat Schwann Cells, J. Neurosci. (2018). doi:10.1523/jneurosci.22-10-04066.2002.

169. H. Peluffo, P. González, A. Arís, L. Acarin, J. Saura, A. Villaverde, B. Castellano, B. González, RGD domains neuroprotect the immature brain by a glial-dependent mechanism, Ann. Neurol. (2007). doi:10.1002/ana.21170.

170. M. Zhu, S. Lin, Y. Sun, Q. Feng, G. Li, L. Bian, Hydrogels functionalized with N-cadherin mimetic peptide enhance osteogenesis of hMSCs by emulating the osteogenic niche, Biomaterials. (2016). doi:10.1016/j.biomaterials.2015.10.072.

171. E. Kaemmerer, F.P.W. Melchels, B.M. Holzapfel, T. Meckel, D.W. Hutmacher, D. Loessner, Gelatine methacrylamide-based hydrogels: An alternative three-dimensional cancer cell culture system, Acta Biomater. (2014). doi:10.1016/j.actbio.2014.02.035.

172. R. Gentile, G. Stevenson, T. Dooley, D. Franklin, I. Kawabori, A. Pearlman, Pulsed Doppler echocardiographic determination of time of ductal closure in normal newborn infants, J. Pediatr. (1981). doi:10.1016/S0022-3476(81)80719-6.

173. J.I. Hagadorn, D. Kendrick, J.C. Madan, I.D. Frantz, Patent Ductus Arteriosus Therapy: Impact on Neonatal and 18-Month Outcome, Pediatrics. (2009). doi:10.1542/peds.2007-2781.

174. A. Chiruvolu, P. Punjwani, C. Ramaciotti, Clinical and echocardiographic diagnosis of patent ductus arteriosus in premature neonates, Early Hum. Dev. (2009). doi:10.1016/j.earlhumdev.2008.12.008.

175. J. Gien, Controversies in the Management of Patent Ductus Arteriosus, Neoreviews. (2008). doi:10.1542/neo.9-10-e477.

176. K. Echtler, K. Stark, M. Lorenz, S. Kerstan, A. Walch, L. Jennen, M. Rudelius, S. Seidl, E. Kremmer, N.R. Emambokus, M.L. Von Bruehl, J. Frampton, B. Isermann, O. Genzel-Boroviczény, C. Schreiber, J. Mehilli, A. Kastrati, M. Schwaiger, R.A. Shivdasani, S. Massberg, Platelets contribute to postnatal occlusion of the ductus arteriosus, Nat. Med. (2010). doi:10.1038/nm.2060.

177. J. Le, M.A. Gales, B.J. Gales, Acetaminophen for Patent Ductus Arteriosus, Ann. Pharmacother. (2015). doi:10.1177/1060028014557564.

178. A.H. Tobias, C.D. Stauthammer, Minimally invasive per-catheter occlusion and dilation procedures for congenital cardiovascular abnormalities in dogs, Vet. Clin. North Am. - Small Anim. Pract. (2010). doi:10.1016/j.cvsm.2010.03.009.

179. J.E. Blossom, J.M. Bright, L.G. Griffiths, Transvenous occlusion of patent ductus arteriosus in 56 consecutive dogs, J. Vet. Cardiol. (2010). doi:10.1016/j.jvc.2010.04.002.

180. P. Giliberti, C. De Leonibus, L. Giordano, P. Giliberti, The physiopathology of the patent ductus arteriosus, J. Matern. Neonatal Med. (2009). doi:10.1080/14767050903198215.

181. P. Bajaj, R.M. Schweller, A. Khademhosseini, J.L. West, R. Bashir, 3D Biofabrication Strategies for Tissue Engineering and Regenerative Medicine, Annu. Rev. Biomed. Eng. (2014). doi:10.1146/annurev-bioeng-071813-105155.

182. W.T. Gerthoffer, Mechanisms of vascular smooth muscle cell migration, Circ. Res. (2007). doi:10.1161/01.RES.0000258492.96097.47.

183. G.J.C. Ye, A.P. Nesmith, K.K. Parker, The role of mechanotransduction on vascular smooth muscle myocytes cytoskeleton and contractile function, Anat. Rec. (2014). doi:10.1002/ar.22983.

184. M.J. Davis, X. Wu, T.R. Nurkiewicz, J. Kawasaki, G.E. Davis, M.A. Hill, G.A. Meininger, Integrins and mechanotransduction of the vascular myogenic response., Am. J. Physiol. Heart Circ. Physiol. (2001). doi:10.1074/jbc.R300038200.

185. P.W. Alford, A.P. Nesmith, J.N. Seywerd, A. Grosberg, K.K. Parker, Vascular smooth muscle contractility depends on cell shape, Integr. Biol. (2011). doi:10.1039/c1ib00061f.

186. R. Yamin, K.G. Morgan, Deciphering actin cytoskeletal function in the contractile vascular smooth muscle cell, J. Physiol. (2012). doi:10.1113/jphysiol.2012.232306.

187. V. Mironov, R.P. Visconti, V. Kasyanov, G. Forgacs, C.J. Drake, R.R. Markwald, Organ printing: Tissue spheroids as building blocks, Biomaterials. (2009). doi:10.1016/j.biomaterials.2008.12.084.

188. D.D. Swartz, J.A. Russell, S.T. Andreadis, Engineering of fibrin-based functional and implantable small-diameter blood vessels, Am. J. Physiol. Circ. Physiol. (2004). doi:10.1152/ajpheart.00479.2004.

189. J. Qiu, Y. Zheng, J. Hu, D. Liao, H. Gregersen, X. Deng, Y. Fan, G. Wang, Biomechanical regulation of vascular smooth muscle cell functions: From in vitro to in vivo understanding, J. R. Soc. Interface. (2014). doi:10.1098/rsif.2013.0852.